

3.4.11 IC RF Subsystems: Complete UHF Front-end

The schematic of the complete front-end, made of the building blocks described in the previous sections, is shown in Fig. 38.

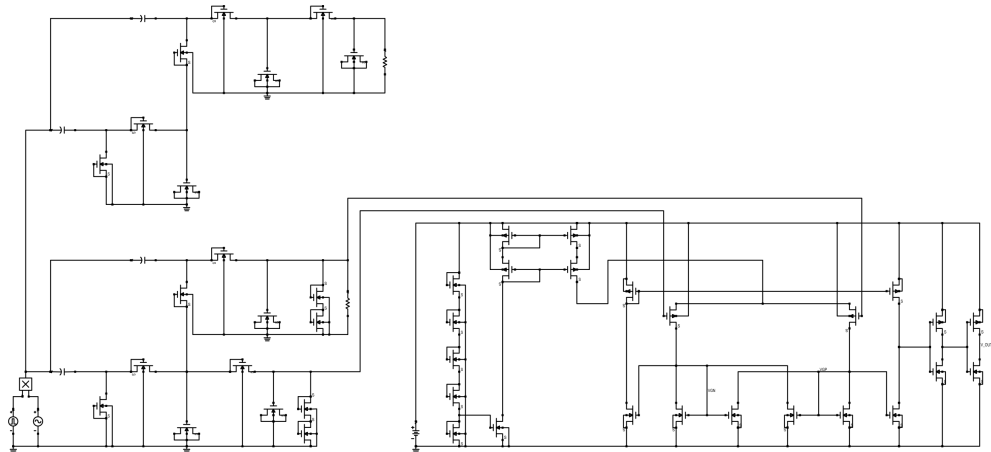


Figure 38: Schematic of the compete UHF front-end.

The performance have been evaluated with a harmonic balance simulation and by using an input voltage source. Moreover a transient simulation has been performed to test the demodulator behavior with a time varying modulated input signal. The DC output voltage of the power rectifier as a function of the RF input power is plotted in Fig. 39. The signal provided to the signal rectifier to the comparator and its output are plotted in Fig. 40. The comparator works correctly, with a constant bias voltage of 1 V, for input power greater or equal to -27 dBm that corresponds to an RF input voltage at the signal rectifier of about 150 mV and a difference of its output signals of about 25 mV. The RF input voltage is the voltage at the system input.

The input impedance and the reflection coefficient of the complete system before the matching are shown in Fig. 41. It varies as a function of the input power being a non-linear system and it is about $50 - j325 \Omega$ for an input power of -20 dBm. An external inductor of 57 nH in series with the input is required to match the circuit to a 50Ω input antenna. The performance have been evaluated with a harmonic balance simulation with a power source and they are very close to those ones reported in this section.

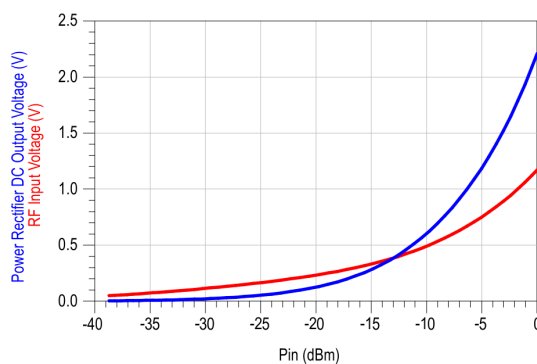


Figure 39: Simulation of the complete system: magnitude of the RF input voltage and DC output voltage of the power rectifier vs. the RF input power.

The layout of the complete front-end is shown in Fig. 42.

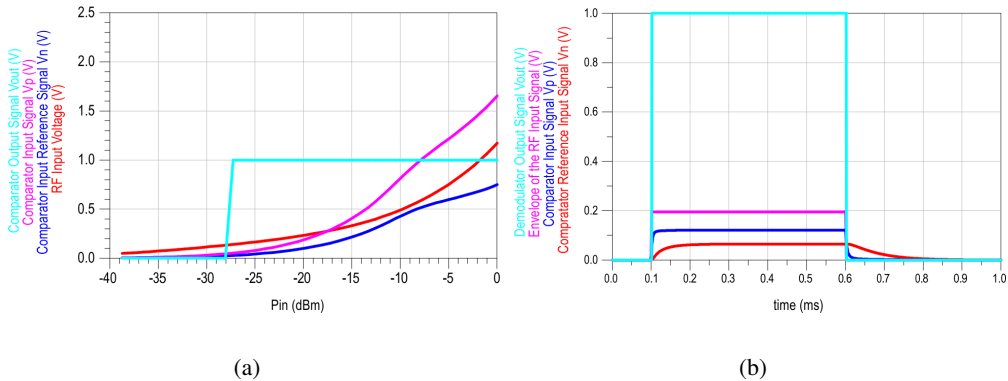


Figure 40: Simulation of the complete system: (a) magnitude of the RF input voltage, comparator input reference signal V_n , comparator input signal V_p , and Comparator output signal V_{out} vs. the RF input power; (b) demodulator output, comparator input signal V_p and reference input signal V_n for a modulated input pulse with magnitude 0.2 V vs. time.

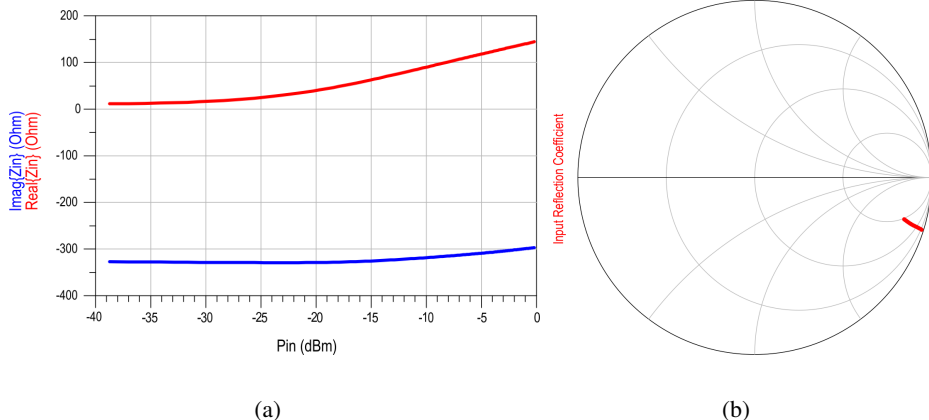


Figure 41: Simulation of the complete system: (a) input impedance and (b) reflection coefficient vs. RF input power.

3.5 Tag Subsystems Test

3.5.1 IC Subsystems: Prototyping and Test

The designed application specific integrated circuit (ASIC) prototype has been fabricated exploiting the mini-ASIC program and the UMC 180nm technology. The occupied area of the entire prototype is 1.5 mm x 3 mm. The prototype is shown in figure 43

A Printed Circuit Board (PCB) has been designed in order to perform the tests at RF. The chip packaged and assembled on the PCB is shown in figure 44. The package is a QFN48, useful for RF applications.

3.5.2 IC RF Subsystems: UWB Backscatter Modulator

The UWB backscatter modulator performance have been analyzed by measuring the reflection coefficients by means of a vector network analyzer (VNA). A test fixture (WILTRON 3680K) has been used as support for the Device Under Test (DUT). A preliminary measurement of the PCB 50 Ω transmission line in open circuit condition has been performed in order to remove its contribution by means of a de-embedding. Moreover the parasitic inductance related to the wire bond has been compensated. The

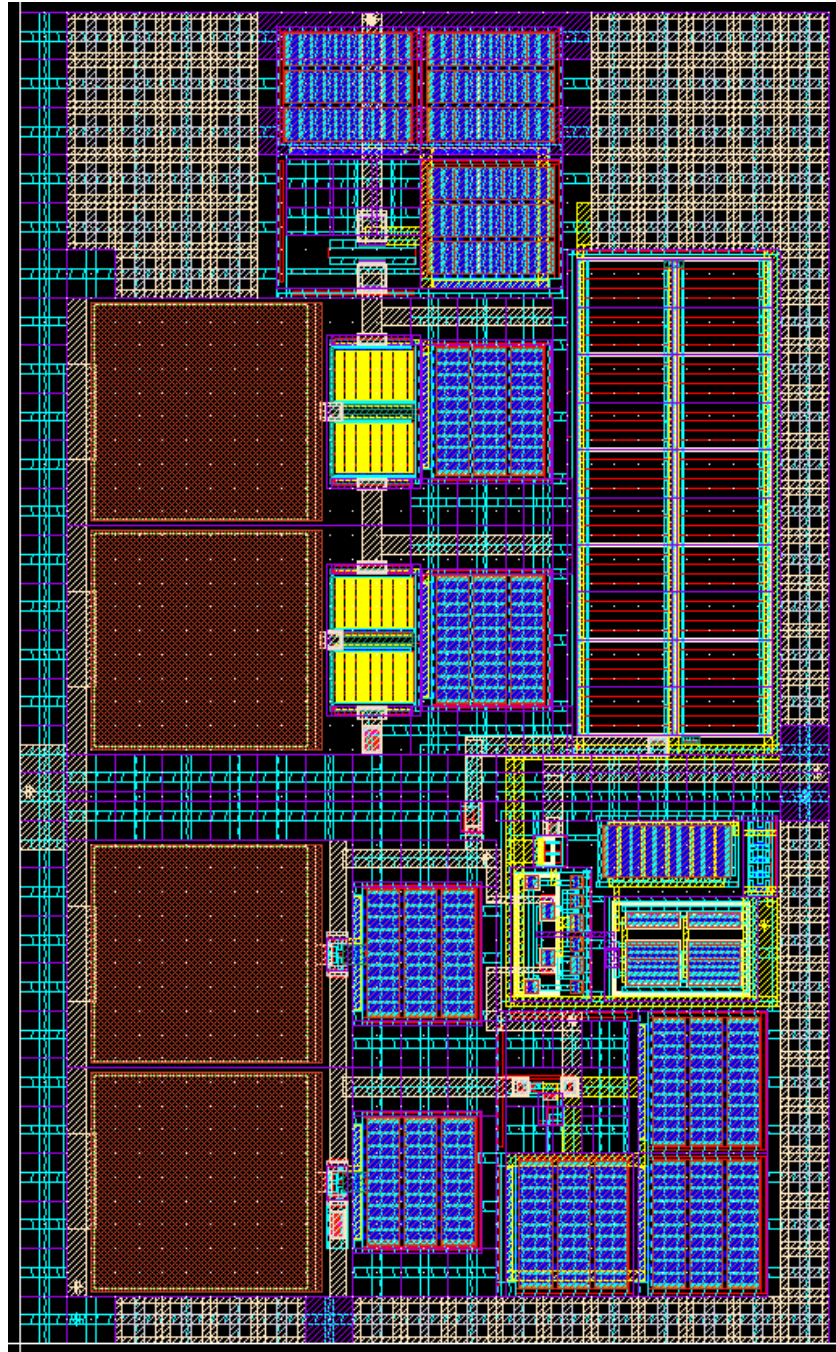


Figure 42: Layout of the complete UHF front-end.

measured reflection coefficients are plotted in figure 45 showing a good agreement with the simulations.

3.5.3 IC RF Subsystems: UHF Power Rectifier for EH

The power rectifier performance have been analyzed by measuring its output power as a function of the RF input power at 900 MHz. A signal generator (HP 8657A) and a multimeter (Agilent 34401A) have been used to perform this kind of measurements and a test fixture (WILTRON 3680K) as a support for the DUT. The measurements have been performed in several conditions. In particular, the load impedance and the input matching network have been modified and the results have been compared with the simulated ones.

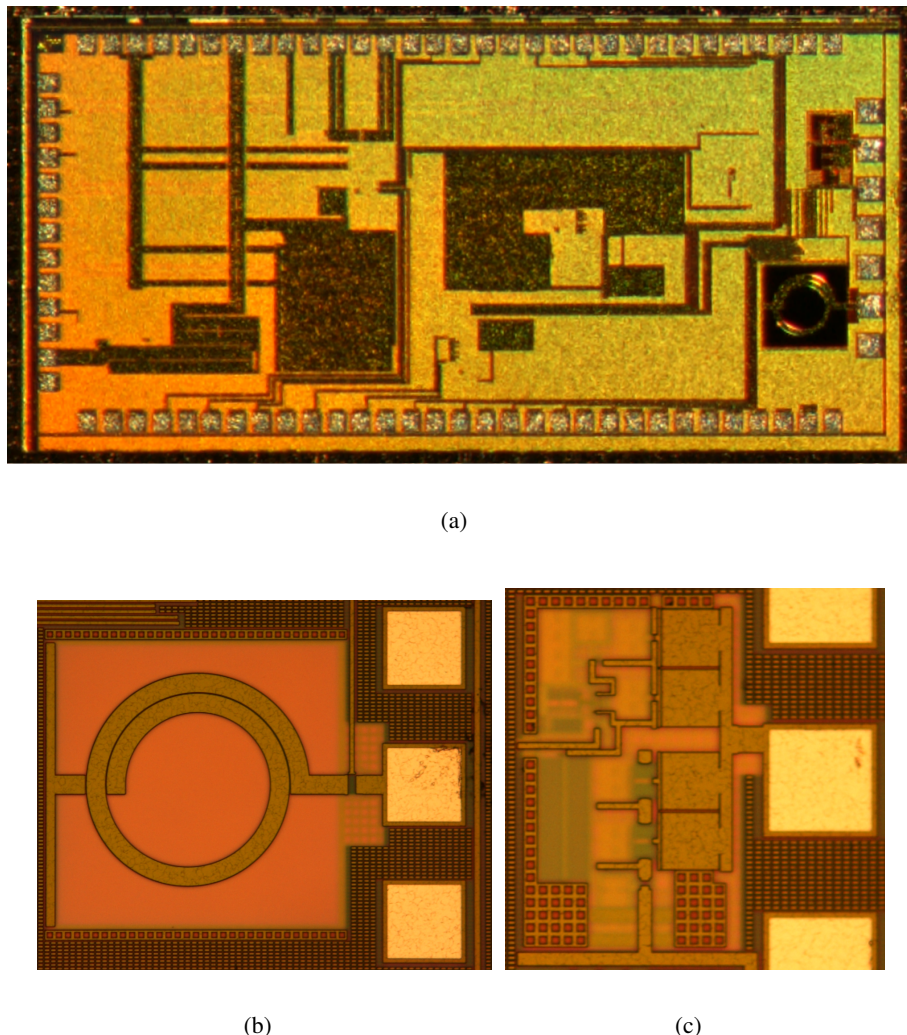


Figure 43: Picture of the fabricated IC. a) complete system; b) UWB backscatter modulator; c) UHF front-end.

The results obtained without the Input Matching Network (IMN) in OC conditions and with a load of $10\text{ k}\Omega$ (the design input impedance of the charge pump in cascade to the rectifier) are plotted in figure 46.

In order to improve the rectifier performance, an IMN has been designed and implemented. The IMN has been designed after the measurement of the rectifier input impedance, plotted in figure 47, by means of a VNA. Simulated and measured values differs because of the presence of the package connections with inductive behavior.

The results, in terms of output voltage, power and conversion efficiency, obtained with the IMN, consisting of an LC ladder network (lumped components values 33 nH and 3 pF), are compared with the simulations in figure 48. As expected, the system is able to provide a voltage greater than 500 mV for RF input power from -10 dBm . The results obtained for a simpler IMN (a lumped inductor of 27 nH in series) are plotted in figure 49. In the latter case, a better matching is obtained for higher input power but the performance for low and mid input powers, such as -10 dBm are lower than those ones in the previous case.

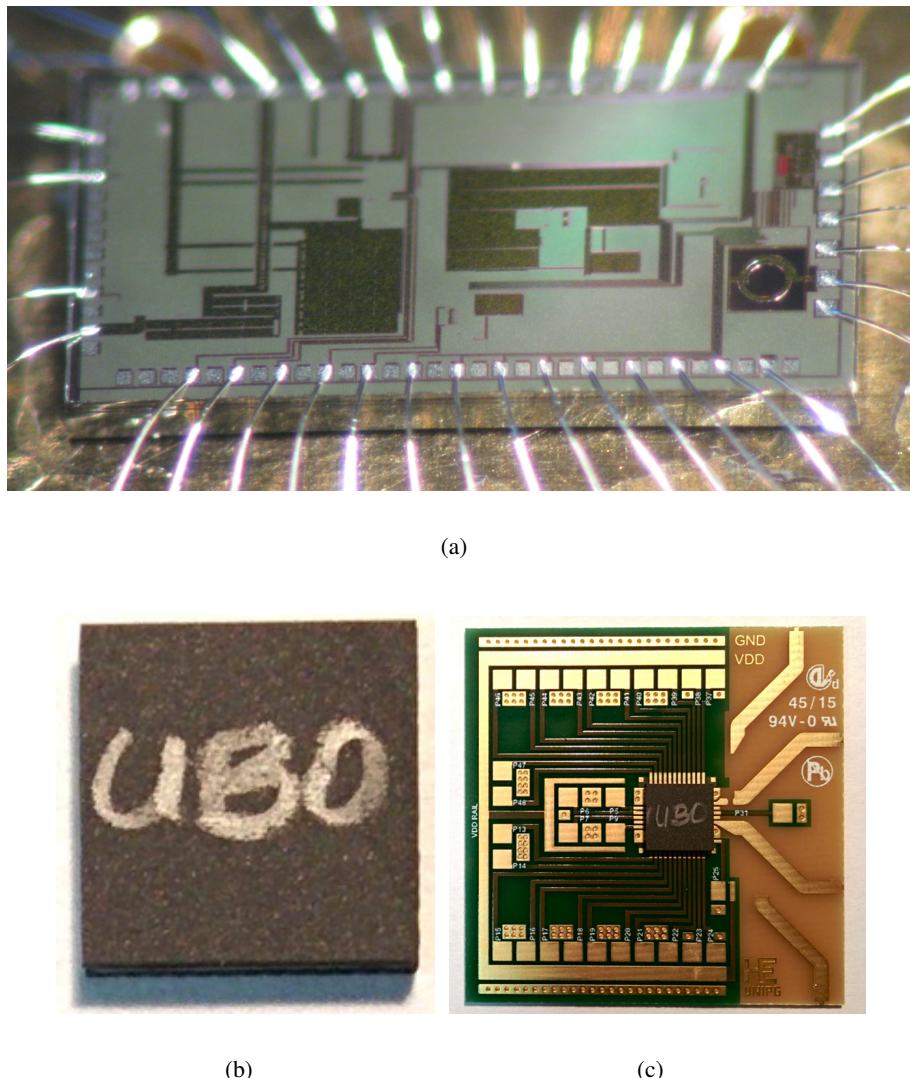


Figure 44: IC under test. a) IC with bonding wire; b) packaged IC; c) IC assembled on the PCB.

3.5.4 IC RF Subsystems: UHF Demodulator

The demodulator has been tested by measuring the comparator output as a function of the RF input power at 900 MHz. A signal generator (HP 8657A) and an oscilloscope (Agilent 54621A) have been used to perform this kind of measurements and a test fixture (WILTRON 3680K) as a support for the DUT. Tests about the subcomponents of the demodulator (current generator, comparator and signal rectifier) cannot be evaluated individually because of the IC layout. The results are plotted in figure 50(a) and the measurements show a good agreement with the simulations. The absence of the IMN reduce the operating range: a input signal is classified as high logic level from the comparator for input power greater than -15 dBm unlike the simulated matched case for which the minimum input power that can be distinguished by the comparator is -27 dBm. In terms of voltage, the simulations highlighted that minimum input signal voltage at the rectifier able to be processed by the demodulator correctly is about 120 mV with and without the IMN. A second test has been performed to analyze the response of the demodulator with a time varying input signal. In particular, the RF carrier at 900 MHz with power -10 dBm has been modulated (AM with 1 kHz signal and a modulation coefficient equal to 90 %) and the output signal has been measured. The instruments used to perform this measurement are the same used in the previous case. The measured results are compared with the simulations in figure 50(b) showing, also in this case,

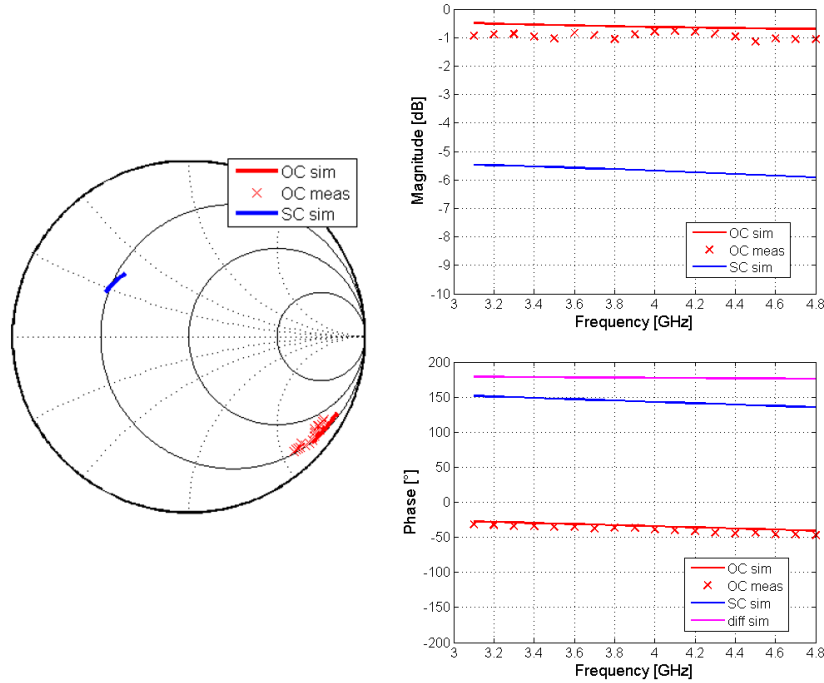


Figure 45: Measured and simulated reflection coefficients of the backscatter modulator controlled by using a voltage equal to 0 V for the OC and 1 V for the SC (a).

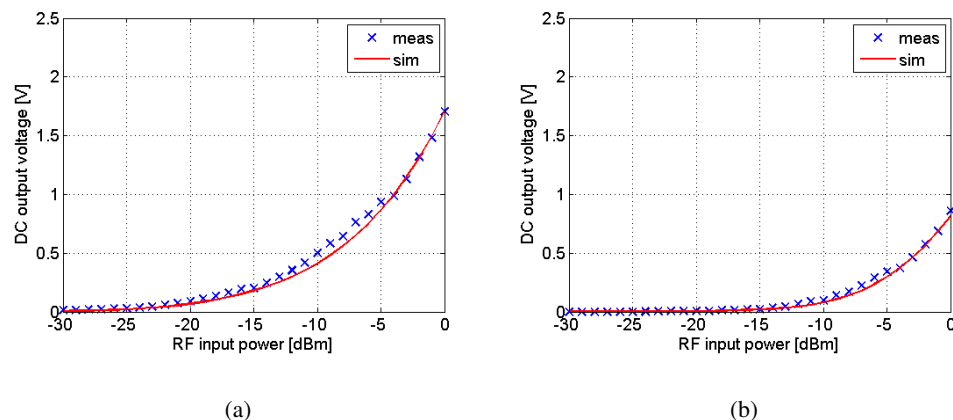


Figure 46: Measurements and simulations of the power rectifier for EH without IMN: output voltage in OC conditions (a), output voltage with a load of $10\text{ k}\Omega$ (b).

a good agreement.

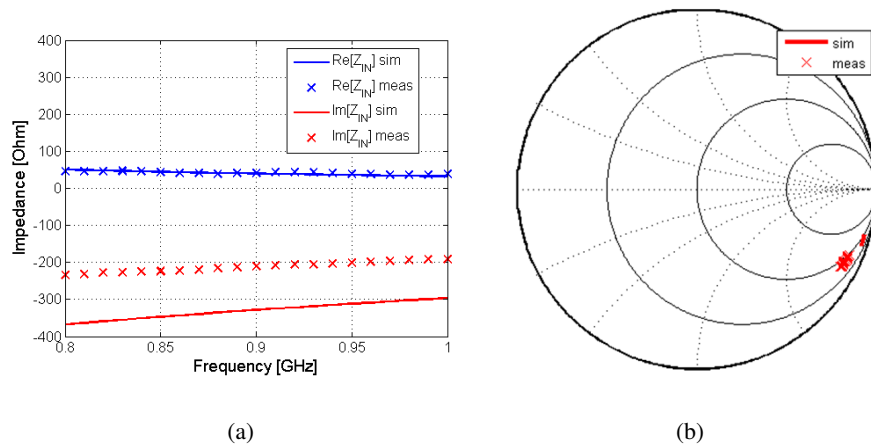


Figure 47: Measured and simulated input impedance (a) and reflection coefficient (b) of the power rectifier for EH vs. frequency for a RF input power of -10 dBm.

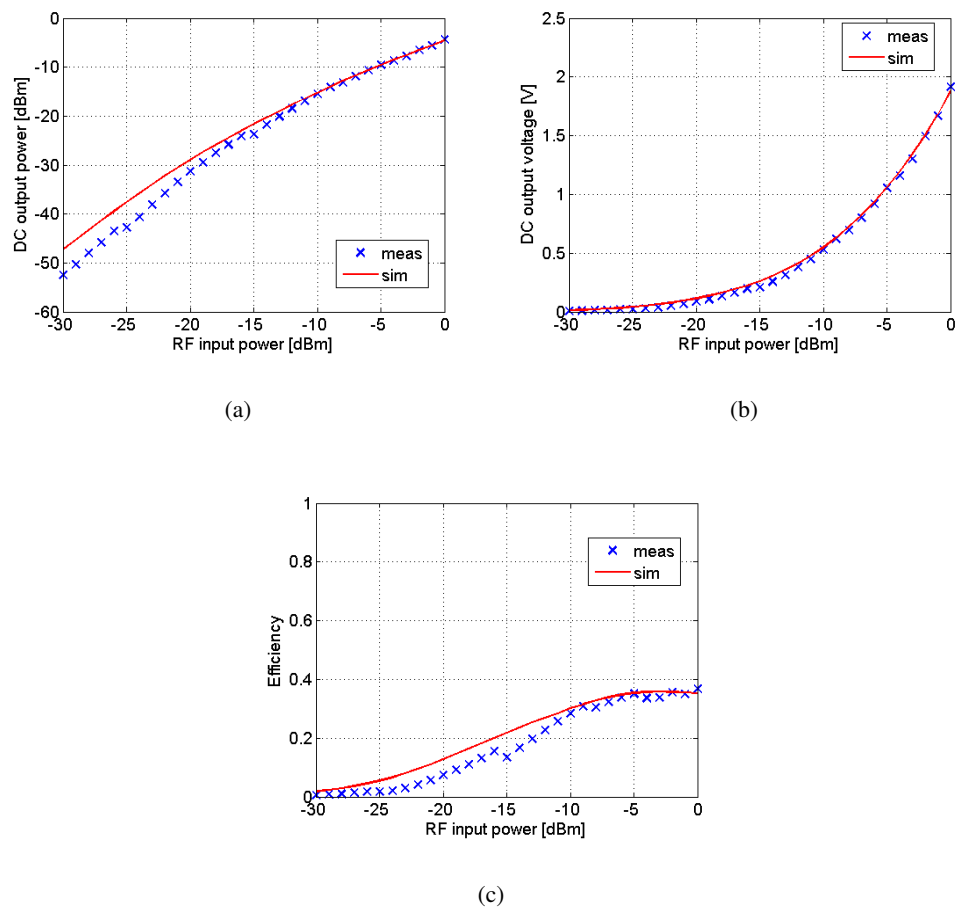


Figure 48: Measurements and simulations of the power rectifier for EH with IMN ($L=33$ nH, $C=3$ pF): output power (a), output voltage (b), and conversion efficiency (c) vs. RF input power.

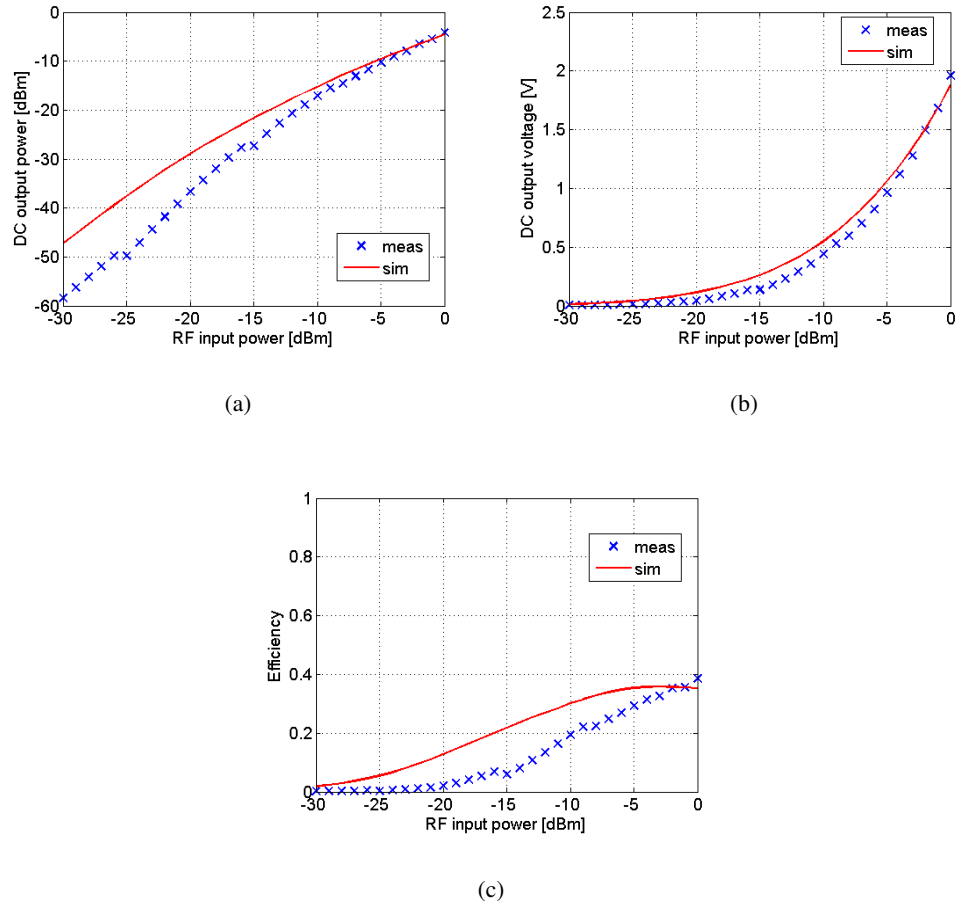


Figure 49: Measurements vs. simulations of the power rectifier for EH with IMN ($L=27$ nH): output power (a), output voltage (b), and conversion efficiency (c) and RF input power.

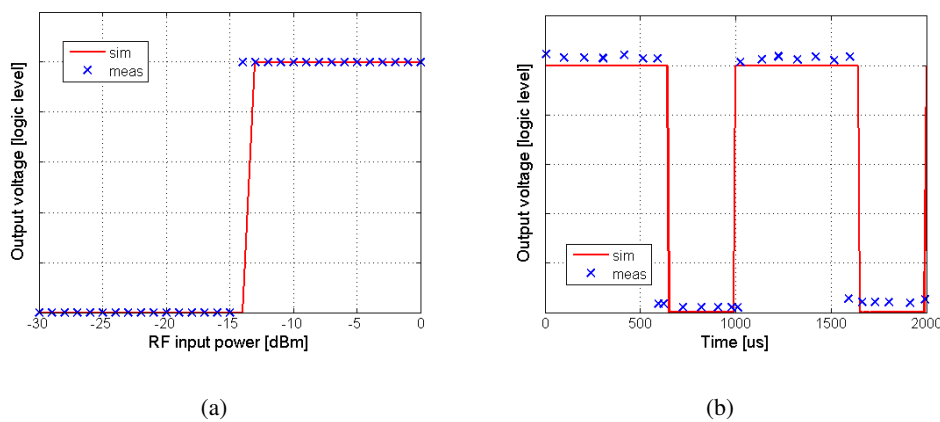


Figure 50: Measurements and simulations of the demodulator without IMN: output vs. RF input power (a), output for an RF input carrier at 900 MHz with power -10 dBm modulated (AM with 1 kHz signal and coefficient of 90 %) (b).

4 IMPLEMENTATION AND TEST OF FINAL DEMONSTRATOR

In this Section, the GRETA test-bed developed at University of Bologna for assessing the performance of UWB tags based on backscatter modulation is presented. The preliminary measurement setup was shown in [5]. Here, an extensive characterization of the adopted instrumentation, configurations, processing schemes and setup is presented, followed by measurement results.

4.1 Measurements Set-Up

The idea for measuring the backscattering characteristic of UWB antennas in the time domain is to generate signals similar to that adopted by RFID readers and collect the environmental response from which the antenna mode component can be extracted. Then, together with the signal processing described in Sec. 4.2.4, the measurement system emulates a sort of RFID receiver.

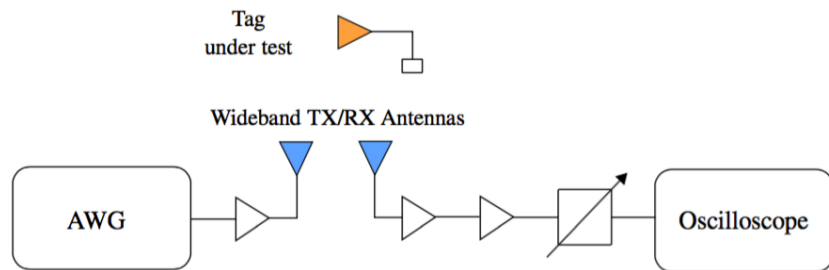


Figure 51: Measurement setup.

The measurement setup is shown in Fig. 51. The probe transmitted signal is generated by an arbitrary waveform generator (AWG), amplified with a wideband amplifier and then fed to a wideband transmitting antenna. The radiated signal propagates in the environment and reaches the tag antenna under test. According to [3], it is necessary to implement a strategy to isolate the antenna mode component from the structural mode component and from the clutter. This is possible by changing the load connected to tag antenna according to the code $\{c_n\}$. This is accomplished by the connection of the tag antenna with a wideband switch, which is loaded with a short circuit load and an open circuit load at its two ports (see Fig. 52). The signal backscattered by the tag and by the surrounding environment is then collected by a receiving antenna. Such a signal is amplified and acquired by an oscilloscope. A programmable attenuator is inserted between the wideband amplifiers chain and the oscilloscope front-end in order to adapt the instrument dynamic to the amplitude of the incoming signal, preventing the damage of its front-end.

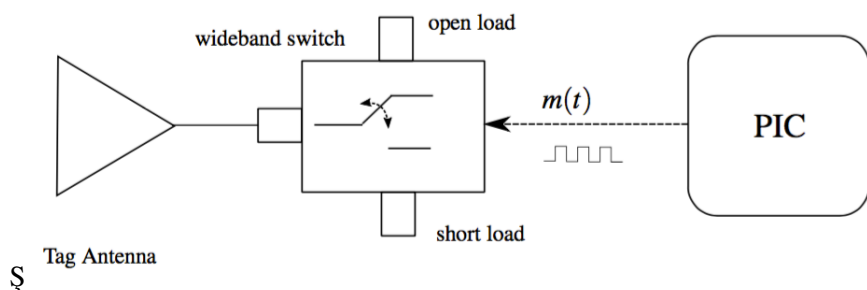


Figure 52: Tag block schematic.

The measurement setup is shown in Fig. 53. In the presented setup the receiving antenna and the transmitting antenna are close and forms a quasi-monostatic measurement configuration [27]. However, the presented measurement scheme can be applied to different transmitter/receiver antennas configurations,

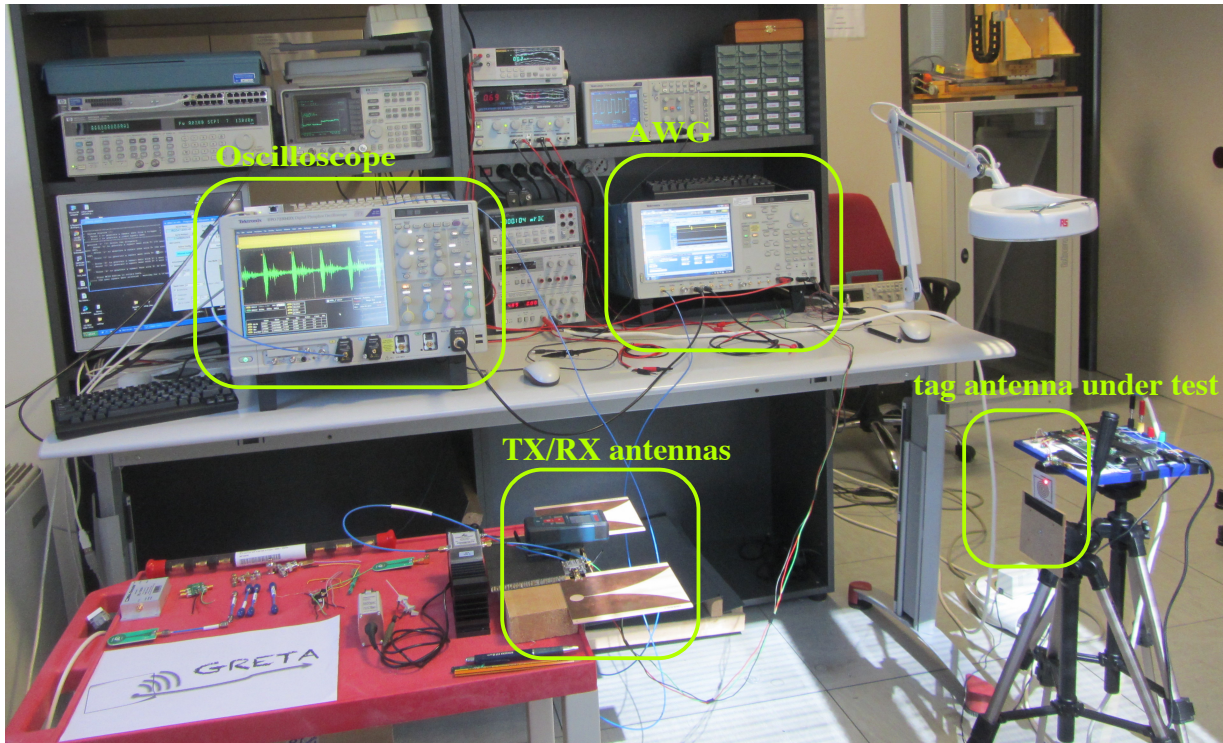


Figure 53: Measurement setup.

Table 3: Adopted instrumentation.

	Component	Producer	Model
Transmitter	AWG	Tektronix	AWG7122C
Receiver (1)	Oscilloscope	Tektronix	TDS6604
Receiver (2)	Oscilloscope	Tektronix	DPO72304DX
Transmitter	Amplifier	Mini Circuits	ZVA-183X-S
Receiver	Amplifier (1)	Mini Circuits	ZVA-183X-S
Receiver	Amplifier (2)	Mini Circuits	ZVE-8G+
Receiver	Attenuator	Mini Circuits	RCDAT-6000-60
TX/RX	Antennas	Imego	Vivaldi 004
Tag	Switch	Hittite	104122-5
Tag	Control Logic	Microchip	PIC24FJ256DA210
Tag	Open load	Aeroflex	7006
Tag	Short load	Aeroflex	7008

also separating them in space in order to test the backscattering characteristics of tags in bistatic configurations, which are very interesting for RFID applications [4, 28]. The instruments, antennas, amplifiers and tools adopted for the presented measurement setup is reported in Tab. 3.

4.2 Signal Processing

4.2.1 Transmitter and Receiver Chain

4.2.1.1 Transmitter

The pulse train (22) adopted as probe interrogation signal was built in Matlab according to the IEEE 802.15.4a specifications in terms of central frequency and bandwidth [29]. A root raised cosine (RRC) pulse centered at frequency $f_c = 4\text{ GHz}$, with pulse width parameter $T_w = 1\text{ ns}$ and roll-off factor $\beta = 0.6$, sampled at frequency $f_s = 12\text{ Gs/s}$ was then imported by the AWG.¹ The PRP has been imposed equal to 50ns; this translates in a maximum reader-tag distance $d_{\max} = 2cT_p \approx 7\text{ m}$ due to radio wave traveling time. The amplitude of the transmitted pulse has been set equal to the maximum AWG analog-to-digital converter (ADC) range.

The transmitted pulse train presents a power of -20 dBm . In order to have a suitable amplitude of the transmitted signal, the AWG output was connected to wideband amplifier with 26dB gain, resulting in a power around 20dB above the federal communications commission (FCC) limit.²

4.2.1.2 Receiver Front-End

At receiver side, a Vivaldi antenna collects the signal reflected by the environment and the tag. Such a signal is then amplified with a copule of wideband amplifier (26dB and 30dB gain) and fed to an oscilloscope which operates as a front-end sampling the incoming signal at frequency f_s . Two different oscilloscopes are considered: the first, with 6GHz bandwidth, operating at $f_s = 20\text{ Gs/s}$ and collecting 200ksamples (i.e., collecting $10\mu\text{s}$ of the received signal, corresponding to acquire the response to 200 transmitted pulses with 50ns PRP); the second, with 23GHz bandwidth, operating at $f_s = 25\text{ Gs/s}$ and collecting 12,5Msamples (i.e., collecting $500\mu\text{s}$ of the received signal, corresponding to acquire the response to 10000 transmitted pulses with 50ns PRP). A comparison of the oscilloscope capabilities is presented in Fig. 54 and Fig. 55.

Acq. window duration	Acq. window length	# of pulses	Sample rate	Sample time
10 μs	200 ksamp	200 (100)	20 Gs/s	50 ps

Figure 54: Receiver front-end: oscilloscope 1.

Acq. window duration	Acq. window length	# of pulses	Sample rate	Sample time
500 μs	12,5 Msamp	10000 (5000)	25 Gs/s	40 ps

Figure 55: Receiver front-end: oscilloscope 2.

Fig. 56 presents a comparison between the reference pulse generated by the AWG, and the two pulses obtained at the output of the two power amplifiers considered, properly scaled and time-aligned. As it is possible to notice, the distortion introduced by the amplifiers is almost negligible;³ this is confirmed by the cross-correlation coefficients between the reference pulse and the two amplified pulse, whose values are 0.96 for the ZVA-183X-S and -0.91 for the ZVE-8G+.

¹The instrument has been equipped with an optional board in order to generate UWB signals.

²Actually, the FCC limit is imposed on the effective isotropic radiated power (EIRP) so the antenna gain in the maximum direction of the transmitting antenna was considered.

³Notice that the 30dB amplifier ZVE-8G+ introduces a sign inversion of the signal.

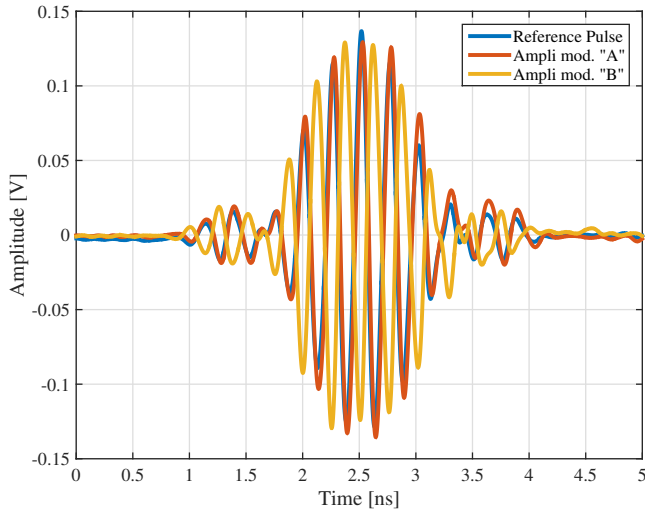


Figure 56: Amplified UWB pulses.

The described complete transmitter and front-end receiver chain is reported in Fig. 51.

4.2.2 UWB Tag

The UWB tag has been emulated with discrete components. The antenna under test has been connected to a UWB switch board. Such a switch, with 6GHz bandwidth, links the antenna port with two SMA ports, depending on the control signal; these two ports are connected to an open and a short circuit load, respectively, as depicted in Fig. 52. The switch board is driven by a Microchip DM240312 development board for the PIC24FJ256DA210 micro controller. The micro controller is programmed for generating a control signal consisting on a sequence of alternating +1 and -1 chips at different rates, that is, with a variable number of pulses per chip N_{pc} . Then, the resulting codes are, for example:

$$\tilde{c}^{(1)} = \left\{ \underbrace{+1, -1}_{\text{alternation of 1 chip}}, +1, -1, +1, -1, +1, -1, +1, -1, \dots \right\}$$

$$\tilde{c}^{(2)} = \left\{ \underbrace{+1, +1, +1, +1, -1, -1, -1, -1}_{\text{alternation of 4 chips}}, +1, +1, +1, +1, \dots \right\}.$$

The programmed chip times are 250ns, 500ns, 1μs, 2μs and 5μs. A switch loss of 4dB was measured at the central frequency $f_c = 4\text{GHz}$.⁴

The tag code driving the backscatter modulator at tag side has been considered as free-running and continuously switching the tag status between open and short circuit. The impact of this choice in the processing necessary to extract the antenna mode component will be described in Sec. 4.2.4.

4.2.3 Signal Acquisition Description

These sample measurements were conducted by acquiring the 200ksamples available from the oscilloscope TDS6604. Fig. 57 shows an example of an acquisition where the channel responses to several transmitted pulses are plotted jointly with the tag's switch command signal collected with a probe.⁵ Fig. 58 shows the channel response to a pulse transmitted by the Vivaldi antenna and collected with an other antenna in the quasi-monostatic configuration. The overall acquired signal is composed of a series of 200 of

⁴Then, due to the backscattering mechanism, the switch loss on the tag signal is about 8dB.

⁵It is possible to notice the 250ns chip time.

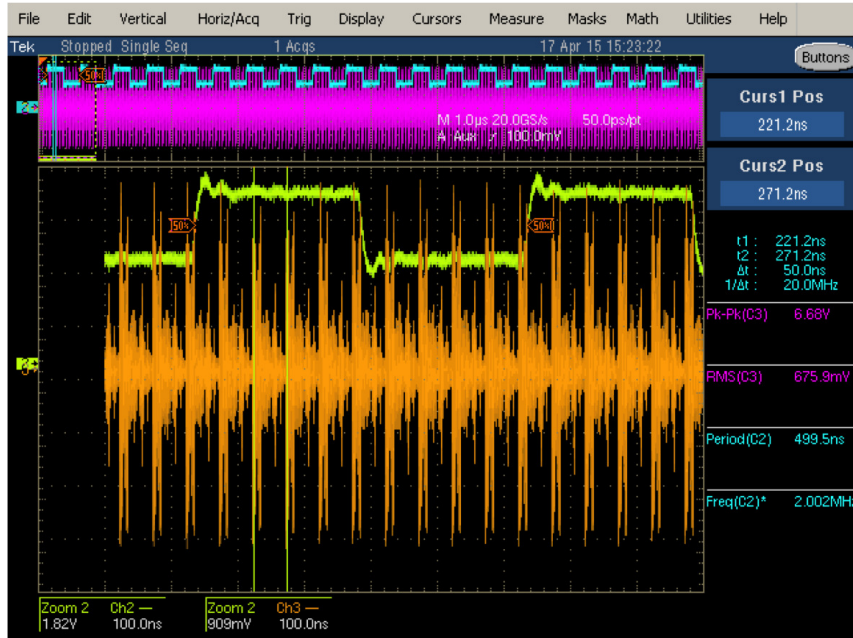


Figure 57: Example of oscilloscope capture.

these waveforms. The presented waveform encompasses the clutter $r^S(t)$ (i.e., the environment response to the transmitted pulse given by the reflection of the walls, furniture and objects in the room) and the tag response $r^T(t)$ (i.e., the antenna structural mode and antenna mode). Then, the signal at the receiver, can be written as

$$r(t) = r^T(t) + r^S(t) + n(t) \quad (4)$$

where $r^T(t)$ denotes the tag's contribution, that is, the tag's antenna mode component (comprehensive of multipath in a real scenario), while $r^S(t)$ accounts for the static contribution (comprehensive of multipath) between transmitter and receiver. Finally, $n(t)$ models the additive white Gaussian noise (AWGN) with one-sided power spectral density N_0 . Moreover, the tag response can be represented in the form

$$r^T(t) = \sum_{i=0}^{N_s-1} \tilde{c}_i w^T(t - iT_p - \tau) \quad (5)$$

being $w^T(t)$ the antenna-mode response to the transmitted pulse.

In general the clutter can be considered almost constant between subsequent PRP, while the antenna mode component changes according to the spreading code $\{c_n\}$ driving the switch in the wideband tag. In Fig. 58 it is possible to notice the first large component of the response, that is the coupling between the transmitting and receiving antennas; then, a series of multipath components with different time-of-arrival (TOA) are characteristic of the environment where measures are taken and of the antennas' positions and orientations. In the presented measurements configurations the response amplitude is about 6 V_{pp} .

4.2.4 Signal Processing

The goal of the signal processing is to extract from the raw collected data the tag antenna mode component $w^T(t)$, which is modulated by the switch and then constitutes the useful part. The block diagram of such processing chain is depicted in Fig. 59.

First of all the signal acquired by the oscilloscope is filtered to eliminate the out of band noise. Filtering is realized in the frequency domain, operating a fast Fourier transform (FFT) on the data samples and considering an ideal band-pass mask with center frequency 4GHz and 2GHz bandwidth. The filtering

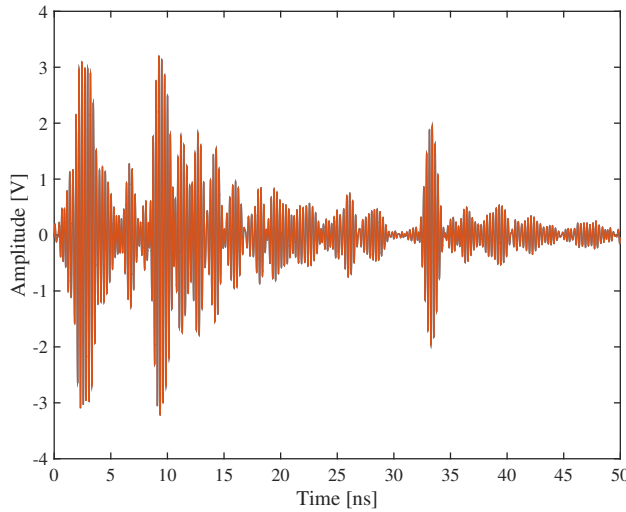


Figure 58: Channel response to a transmitted pulse.

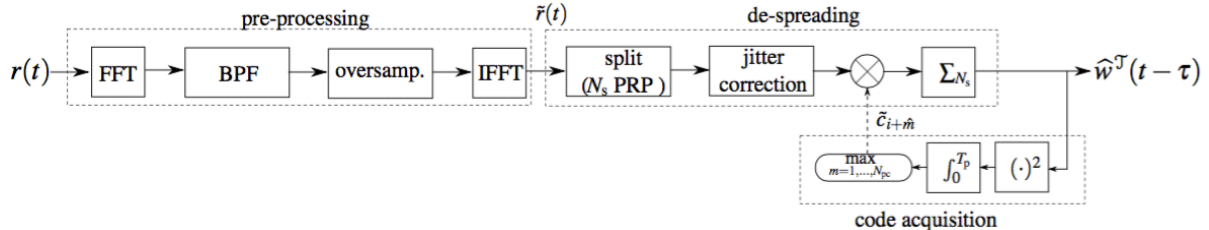


Figure 59: Signal processing scheme.

process is followed by an oversampling stage. This is fundamental to counteract drift effects due to the independent local oscillators of the transmitting AWG and receiving oscilloscope. In fact, although the sampling frequency of the oscilloscope is greater than the Nyquist rate, the presence of two different oscillators driving the transmission of the pulses and the acquisition makes a clock skew between the two instruments not negligible, and the effects are particularly pronounced due to the long duration of the transmitted and acquired signal. Moreover, the jitter itself of the oscillator driving the oscilloscope can strongly degrade the clutter removal performance of the successive processing blocks, making impossible the measurement of the backscattered antenna mode signal component. Such effects are then mitigated by operating an oversampling on the receiving signal. In order to reduce the elaboration time, oversampling has been realized in the frequency domain, by inserting a zero-padding sequence in the middle of the vector resulting from the filtered signal. Specifically, considering the vector of samples acquired by the oscilloscope $\mathbf{r} = r(m\delta t)$, with $m = 1, \dots, N = T_s/\delta t$ and $\delta t = 1/f_s$, define $\mathbf{s} = \text{FFT}[\mathbf{r}]$. Then, considering an oversampling factor OF, the time-domain oversampled signal $\tilde{\mathbf{r}} = \tilde{r}(m\tilde{\delta}t)$, $\tilde{\delta}t = \delta t/OF$, of length $N \cdot OF$ is obtained as

$$\tilde{\mathbf{r}} = \text{OF} \cdot \text{IFFT} \left[\tilde{\mathbf{s}} \left(1 : \frac{N}{2} \right) \underbrace{0, \dots, 0}_{N \cdot (\text{OF}-1)} \tilde{\mathbf{s}} \left(\frac{N}{2} : N \right) \right] \quad (6)$$

where $\tilde{\mathbf{s}}$ denotes the filtered version of \mathbf{s} .

4.2.5 De-Spreading

The core processing enabling the cancellation of the clutter component $r^S(t)$ is the de-spreading. The waveform is split in frames of length equal to the PRP T_p (see Fig. 60), which are multiplied for a code

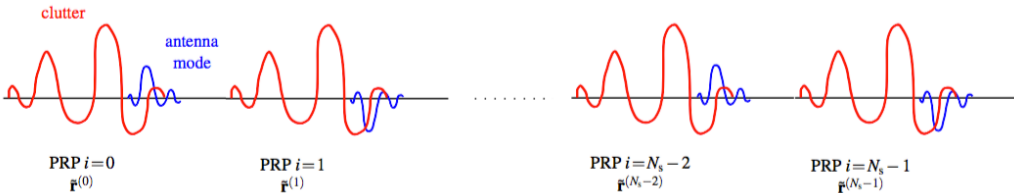


Figure 60: Signal splitting in N_s portions of length T_p .

equivalent to that adopted at tag side (and synchronous with it). This is possible since the spreading code generated by the PIC board is known. Then, these signal portions are coherently summed up together. Formalizing, we define the signal portions $\tilde{\mathbf{r}}^{(i)}$ as

$$\tilde{\mathbf{r}}^{(i)} \triangleq \tilde{\mathbf{r}}\left((i \cdot N_p + 1) : (i \cdot N_p + N_p)\right) \in \mathbb{R}^{N_p} \quad (7)$$

where $N_p = T_p / \tilde{\delta}t$. Then, the de-spreading result is given by

$$\hat{\mathbf{w}}^T = \frac{1}{N_s} \sum_{i=0}^{N_s-1} \tilde{c}_i \tilde{\mathbf{r}}^{(i)} \quad (8)$$

where \tilde{c}_i is the same ± 1 code adopted at tag side. Such $\hat{\mathbf{w}}^T$ is an estimate of $\mathbf{w}^T = w^T(m \tilde{\delta}t - \tau)$ for $m = 1, \dots, N_p$. Since the tag code used at receiver is balanced (i.e., it is composed of the same number of $+1$ and -1) the result of such an operation is the cancellation of the clutter component $r^S(t)$ which is constant between subsequent frames. Differently, the tag antenna mode component, which is modulated by the same code at tag side, grows and presents a process gain N_s . Such a principle enabling the clutter cancellation is depicted in Fig. 61.

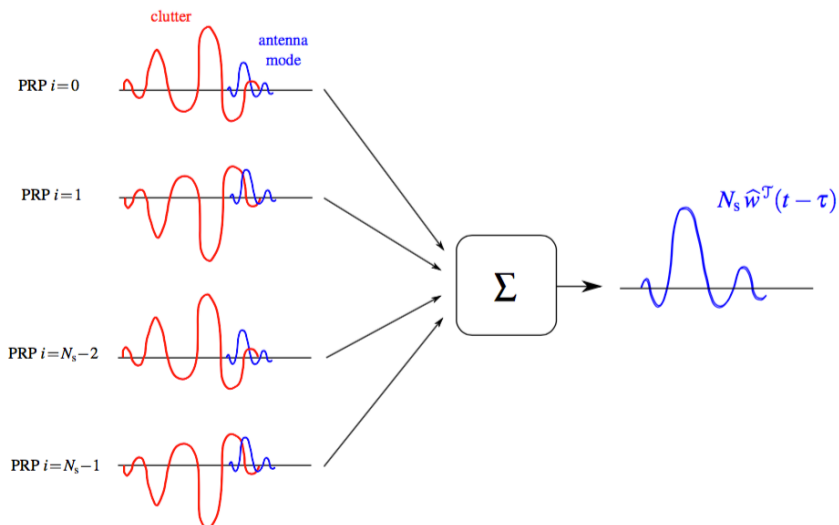


Figure 61: Pictorial representation of the clutter cancellation principle. Note that the depicted signal portions (of length T_p) are already multiplied for the tag code.

The described de-spreading principle has been then improved thanks to the operated oversampling procedure. In fact, we considered for each period of duration T_p the cross-correlation between the first pulse, that is $r(t)$ for $t \in [0, T_p]$ (i.e., the channel response to the transmitted pulse for $i = 0$) and the generic i th channel response, that is, $r(t)$ for $t \in [iT_p, (i+1)T_p]$; since we have $r(t) \approx r^S(t)$, the time instant corresponding to the cross-correlation peak can be adopted instead of the generic iT_p to perform

the de-spreading. Specifically, N_s time-aligned vectors, denoted with $\mathbf{p}^{(i)}$, with $i = 0, \dots, N_s - 1$, are constructed from $\tilde{\mathbf{r}}$ according to

$$\mathbf{p}^{(i)} = \tilde{\mathbf{r}} \left(((i + \Delta^{(i)}) \cdot N_p + 1) : ((i + \Delta^{(i)}) \cdot N_p + N_p) \right) \quad (9)$$

where $\Delta^{(i)} = N_p - \tilde{m} + 1$ and \tilde{m} is the index corresponding to

$$\max_{m=1, \dots, N_p} \text{IFFT} \left[\text{FFT} \left[\tilde{\mathbf{r}}^{(0)} \right] \odot \text{FFT} \left[\tilde{\mathbf{r}}^{(i)} \right]^* \right] \quad i = 1, \dots, N_s - 1 \quad (10)$$

having indicated with \odot the pointwise product and with $(\cdot)^*$ the conjugate. These time-aligned signal portions $\mathbf{p}^{(i)}$ are then adopted in the de-spreading (8) instead of $\tilde{\mathbf{r}}^{(i)}$, considering $\mathbf{p}^{(0)} \triangleq \tilde{\mathbf{r}}^{(0)}$. This allows compensating the small difference between the oscillator of the AWG, driving the transmission instants of the pulses, and that of the oscilloscope side, driving the ADC, and correcting the sampling instant drift. Again, as showed in (10), in order to maximize the performance, the $N_s - 1$ cross-correlations are operated in the frequency domain by considering the multiplication of the FFT of the two involved signal portions.

4.2.6 Code Synchronization

Unfortunately the offset (phase) of the tag code is not known since the tag is not synchronized with the trigger driving the oscilloscope acquisition. Then, a code acquisition stage has been implemented in order to search for the best code offset of the de-spreading block. Specifically, N_{pc} code shifts of the code adopted for the de-spreading are considered. For each code shift a de-spreading procedure is operated and the overall energy of the obtained waveform of length T_p is measured (see Fig. 59). Finally, a decision in favor of the code shift resulting in the maximum output energy is taken, and the corresponding code is adopted for de-spreading. Formalizing, we have

$$\hat{m} = \underset{m=1, \dots, N_{pc}}{\operatorname{argmax}} \left\| \sum_{i=0}^{N_s-1} \tilde{c}_{i+m} \tilde{\mathbf{p}}^{(i)} \right\|^2 \quad (11)$$

and in (8) the code $\tilde{c}_{i+\hat{m}}$ is adopted of \tilde{c}_i .

The result of such a de-spreading operation is shown in Fig. 62. As it is possible to notice, the tag signal TOA is different from the clutter signal TOA (which starts at the beginning of the windows with the antenna coupling since $\tau' \approx 0$ in the considered quasi-monostatic configuration) due to the distance between the transmitting/receiving antennas and the tag antenna. The estimation of such a TOA is usually adopted for guaranteeing the reader-tag ranging and them enabling localization [30]. Moreover, the channel profile of the tag response is different from the overall response of Fig. 58 due to particular tag position in the environment. Finally, as expected, the signal amplitude is significantly lower of that visible in Fig. 58 due to the two-hop propagation mechanism characteristic of backscattering. In the following section experimental results with different tag antennas will be presented and the effect of the processing parameters discussed.

4.2.7 Range Estimation

4.2.8 Order of Arrival Estimation

As a possible final application, we consider the sorting of a stream of objects moving on a conveyor belt, i.e., OOA estimation. Given a stream of N_o objects, the OOA of the objects is represented by the vector \mathbf{o} , whose j th element $\mathbf{o}[j] = l$ indicates that the object l (i.e. l is the identification index with $l = 1, 2, \dots, N_o$) is the j th to cross the monitored area. To simplify the notation, we consider a single tag per object, with the tag for the i th object in position $\mathbf{p}_i \in \mathbb{R}^D$ in a D -dimensional space. At any time, the vector \mathbf{o} is defined as

$$\mathbf{o}[h] = \underset{i \notin \{\mathbf{o}[1], \dots, \mathbf{o}[h-1]\}}{\operatorname{argmax}} \{x_i : i \in \mathcal{O}\} \quad (12)$$

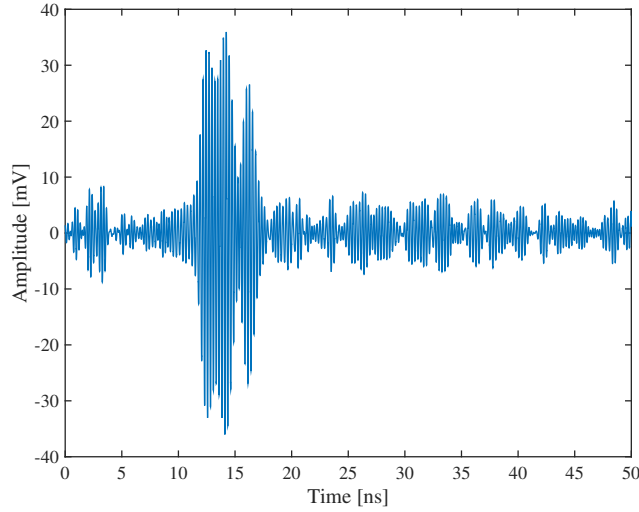


Figure 62: Processing result (estimated tag antenna component).

where x_o is the coordinate of the object i th along the conveyor belt direction. Note that (12) holds for any time since \mathbf{o} is fixed in time and depends on the tags' initial position. In general, the OOA estimation is based on a set \mathbf{z} of measurements taken by a network of readers. For example, \mathbf{z} can represent the set of energy vectors measured from all the reader-tag pairs or the corresponding range estimates.

Consider N_r readers, with index set \mathcal{R} . The r th reader is at $\mathbf{r}_r \in \mathbb{R}^3$ and transmits signals to detect, identify, and localize the tags in the monitored area. Therefore, $\mathbf{z} = \{\mathbf{z}_r^{(k)}\}$ where $\mathbf{z}_r^{(k)}$ is the measurement taken by the r th reader at time index k by processing the signals communicated between the interrogated tags and the reader. The time index $k = 1, 2, \dots, N_m$ varies within a time interval $T_{\text{obs}} = N_m T$, where N_m is the number of measurements and T is the time interval between two subsequent measurements.

Given a set \mathcal{D} of detected objects, the estimated order vector $\hat{\mathbf{o}}$ can take $|\mathcal{D}|!$ possible values, i.e., $\hat{\mathbf{o}} \in \Omega_{|\mathcal{D}|!} = \{\boldsymbol{\omega}_1, \boldsymbol{\omega}_2, \dots, \boldsymbol{\omega}_{|\mathcal{D}|!}\}$, with $\boldsymbol{\omega}_i = [\omega_{i1}, \omega_{i2}, \dots, \omega_{i|\mathcal{D}|}]$. Therefore, the OOA problem corresponds to an M -ary hypothesis test with $M = |\mathcal{D}|!$ where the i th hypothesis is

$$\mathcal{H}_i : \mathbf{o} = \boldsymbol{\omega}_i \forall i \in \Omega_{|\mathcal{D}|!}. \quad (13)$$

Based on the dataset \mathbf{z} of observations, the index \hat{i} of the estimated order vector is given by

$$\hat{i} = \operatorname{argmax}_i \mathbb{P}(\mathcal{H}_i | \mathbf{z}) = \Lambda(\boldsymbol{\omega}_i | \mathbf{z}) \quad (14)$$

where $\Lambda(\boldsymbol{\omega}_i | \mathbf{z})$ is the likelihood function of the vector \mathbf{z} for the i th hypothesis.

We consider both a hard-decision and a soft-decision method, depending on whether the raw energy samples $\mathbf{z} = \mathbf{e} = \{\mathbf{e}_{ri}\}_{r \in \mathcal{R}, i \in \mathcal{O}}$ or a TOA estimation taken from each energy vector $\mathbf{z} = \hat{\mathbf{t}} = \{\hat{t}_{ri}\}_{r \in \mathcal{R}, i \in \mathcal{O}}$ are employed. The choice of \mathbf{z} is driven by the knowledge of its probability distribution and the computational complexity, since it depends on the size of the dataset to be communicated in the network (e.g., in a centralized signal processing).

In case of soft-decision, based on the likelihood function $\Lambda(\mathbf{o} = \boldsymbol{\omega}_i | \mathbf{z})$ with $\mathbf{z} = \mathbf{e}$, the OOA is chosen as

$$\hat{i} = \operatorname{argmax}_i \mathbb{P}(\mathcal{H}_i | \mathbf{z}) = \operatorname{argmax}_i \Lambda(\mathbf{o} = \boldsymbol{\omega}_i | \mathbf{z}) \quad (15)$$

In case of hard-decision, a least square approach is employed based on the $\mathbf{z}^{(k)} = \boldsymbol{\tau}^{(k)}$

$$\hat{i} = \operatorname{argmin}_i \operatorname{argmin}_{\mathbf{p} \in \mathcal{P}_i} \sum_r \sum_j (\|\mathbf{p}_j - \mathbf{r}_r\|/c - \hat{t}_{rj})^2 \quad (16)$$

For what concerns the soft-decision case, the likelihood function $\Lambda(\mathbf{o} = \boldsymbol{\omega}_i | \mathbf{z})$ can lead to very high computational complexity. However, it can be demonstrated that the maximum likelihood estimate in (15) can be approximated with

$$\hat{i} = \arg \max_i \log f_Z(\mathbf{z} | \hat{\mathbf{p}}^{(i)}, \mathcal{H}_i) \quad (17)$$

where

$$\hat{\mathbf{p}}^{(i)} = \arg \max_{\mathbf{p}} \mathbb{P}(\mathbf{p} | \mathbf{z}, \mathcal{H}_i). \quad (18)$$

Then, given $\mathcal{P} \in \mathbb{R}^{D \times N_o}$ as the space of possible tag positions $\mathbf{p} = [\mathbf{p}_1, \mathbf{p}_2, \dots, \mathbf{p}_{N_o}]$, we define $\mathcal{P}_i = \{\mathbf{p} \in \mathcal{P} \text{ s. t. } \mathbf{o} = \boldsymbol{\omega}_i\}$ as the locus of points where the OOA is $\boldsymbol{\omega}_i$. Therefore, (18) becomes

$$\hat{\mathbf{p}}^{(i)} = \arg \max_{\mathbf{p} \in \mathcal{P}_i} f_P(\mathbf{p} | \mathbf{z}) \quad (19)$$

where $f_P(\mathbf{p} | \mathbf{z})$ is known and its empirical approximation can be extrapolated from measurements.

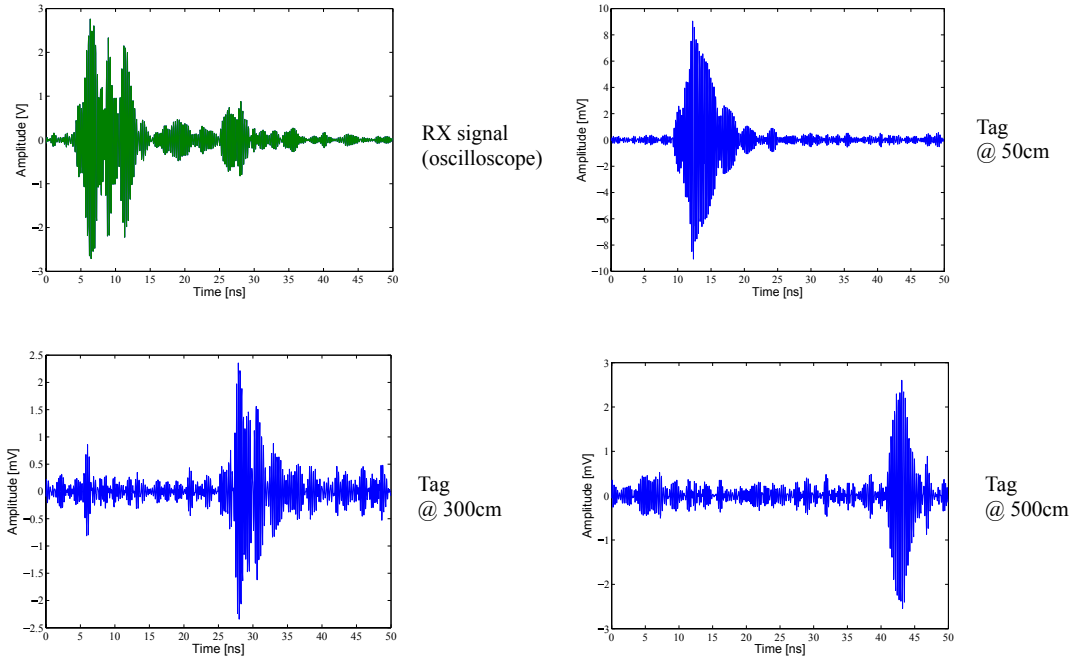


Figure 63: Example of measurements results.

4.3 Experimental Results

In this section experimental results are showed. Specifically, the capability of the proposed setup of extracting the antenna mode backscattered component of UWB antennas will be presented. Then, the effect of the choices in terms of tags' spreading codes and signal processing parameters will be characterized.

4.3.1 UWB Antennas Backscattering

Fig. 62 shows an example of received signal obtained according to the aforementioned measurement setup and signal processing scheme. As it is possible to see, the signal duration is 50 ns, that is, the duration of a PRP. In fact, thanks to the accumulation and de-spreading process, several portions of the received signal are summed up in order to obtain the raw response to a single pulse experiencing a proper processing

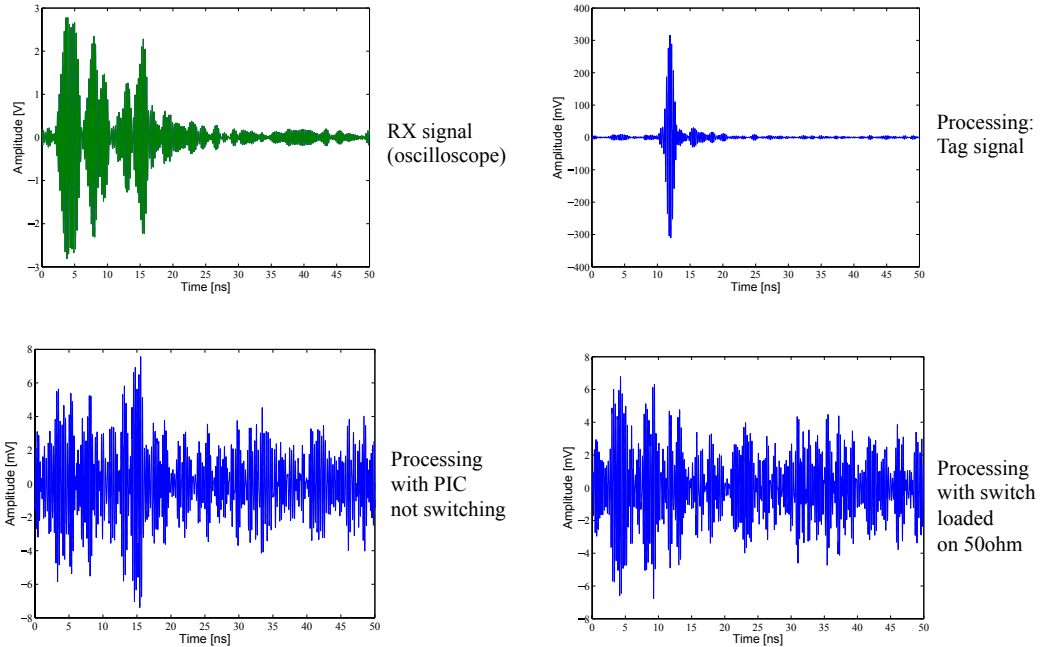


Figure 64: Example of measurements results.

gain. In Fig. 62 and in the subsequent results, the de-spreading result is always divided by the number of accumulated pulses N_s composing a symbol, in order to read in the vertical axis the amplitude in Volt of the backscattered pulse (including amplifiers gain at receiver side).

In order to verify the effect of the processing scheme, in Fig. 63 it is shown a PRP of the original signal collected by the oscilloscope (in green). At first glance, all the N_s PRP look the same due to the dominant amplitude of the clutter component. Specifically, the amplitude of the acquired signal is around 5 V peak-to-peak. Differently, the 3 following pictures in Fig. 63 show the effects of the de-spreading when a tag is present at 0.5 m, 3 m and 5 m of reader-tag distance. In these cases the amplitude of the signal, now composed of antenna mode component and noise only, is significantly lower (around 50 mV peak-to-peak and the starting point of the pulse is a function of the reader-tag distance due to the signal propagation in air, as expected).

The behavior of the adopted processing scheme is confirmed in Fig. 64. In this case, again, in the green picture a PRP of the signal acquired by the oscilloscope is reported. In the following blue pictures the de-spreading result when a tag is active (i.e., switching its backscatter modulator between open and short loads) is presented. As expected, a pulse can be found at a time instant corresponding to the given reader-tag distance. Differently, in the two bottom pictures, the de-spreading result in particular conditions is presented. At the left, the result with the PIC not switching is shown; in this case the antenna mode backscattering component is composed of always the same open or short response. Then, after the de-spreading and accumulation, only noise if present as signal processing output. The same behavior is obtained when the tag antenna is not loaded with open/short loads, but with a matched load (i.e., 50Ω). In this case the tag response is composed of the structural mode response only, and no antenna mode components depending on the unmatched load are backscattered. Then, the de-spreading result is again composed of noise only.

In Fig. 65 the signal responses related to the open-load and short-load antenna mode components are presented. These results have been obtained according to the following measurement setup. First, the two antenna switch ports were connected to a couple of delay-matched transmission lines. Then, one port of the transmission line was connected to a matched load (i.e., 50Ω), while the other to the short load. A measurement was taken according to this scheme. The result of the de-spreading is, in this case, a pulse given by the difference of the response between short load and matched load. Since the response in the

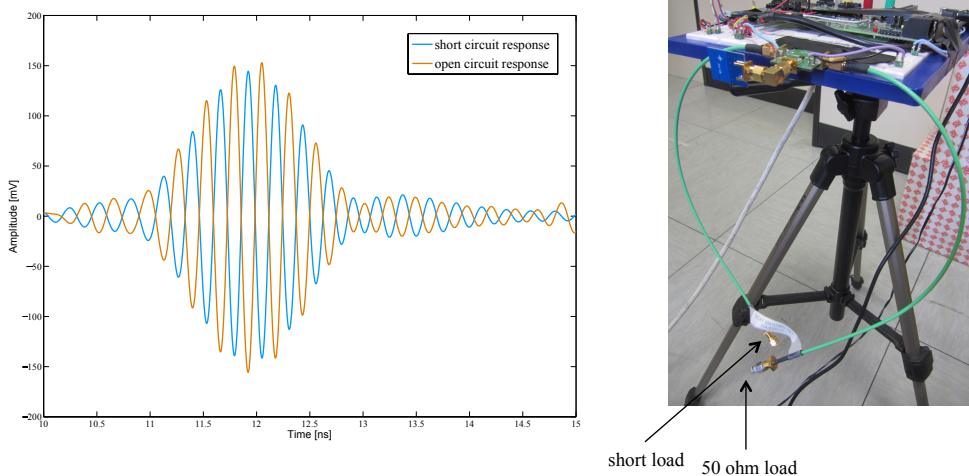


Figure 65: Measured tag open circuit and short circuit responses.

matched load case is composed of structural mode only, we obtained the signal response related to the short load case. By repeating the same procedure manually changing the load between short and open⁶, the response related to the open load case was obtained. As it is possible to see from Fig. 65, the two responses have a 180° phase difference, as expected, especially for the first path (depicted in the figure).

4.3.2 Backscattering Characteristics of Commercial Antennas

In this section, different commercial antennas are tested with the presented measurement setup as potential tag antennas. The considered antennas are presented in Fig. 66. Specifically they are:

- Broadspec antenna by Time Domain Corp.;
- Skycross antenna;
- Fractus antenna;
- WB002 antenna by Decawave.

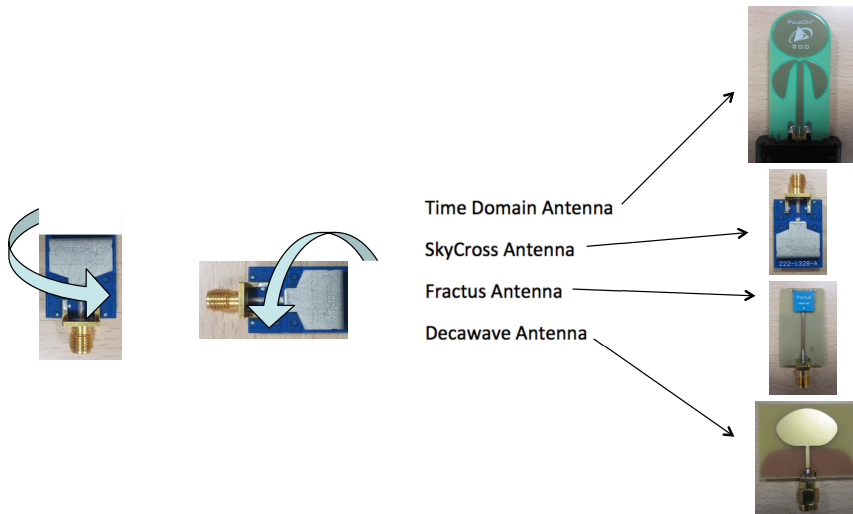


Figure 66: Commercial antennas considered for tag measurements.

All the considered antennas have a dipole-like radiation pattern and present linear polarization. For

⁶The delay-matched transmission line allows changing the load without moving the tag antenna which could result in an unpredictable different response.

this reason, they were tested considering 4 different rotations in the vertical plane and 4 different rotations in the horizontal plane. In all the cases, the reader transmitting and receiving antennas were kept horizontal then resulting in 4 measurements with the same polarization for reader and tag, and 4 measurements in cross-polarization.

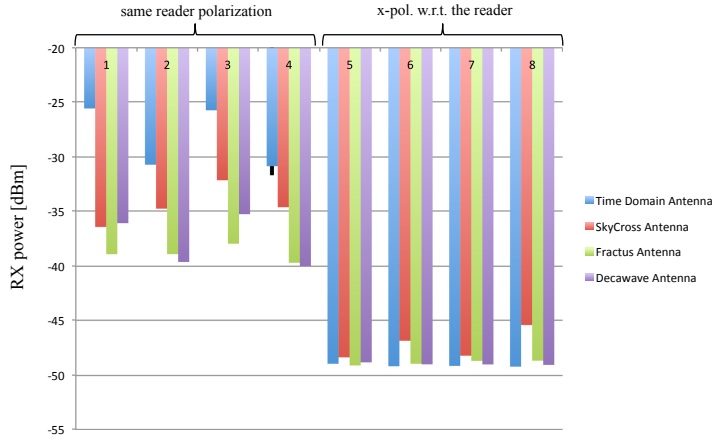


Figure 67: Characterization of commercial antennas in backscattering.

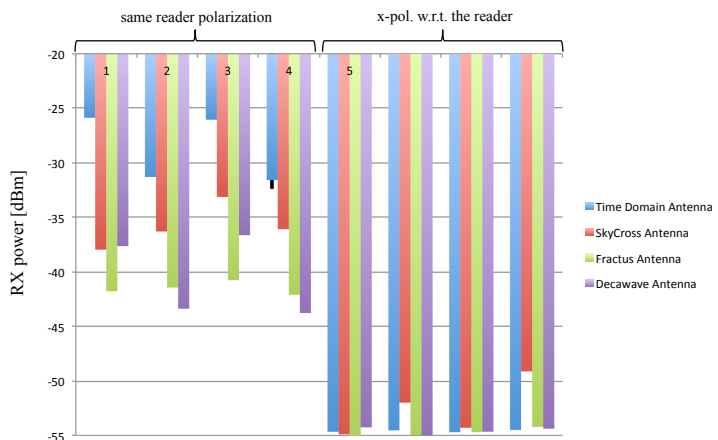


Figure 68: Characterization of commercial antennas in backscattering.

Fig. 67 shows the received power for the 4 antennas, considering the 4 cases of accorded polarization with respect to the reader (first 4 histograms) and the 4 cases of cross-polarization (following 4 histograms). The received power was computed as the ratio between the received energy in a PRP and the PRP duration⁷. As expected, the receiver power in the case of cross-polarization is around 10dB lower than the corresponding case with accorded polarization. In this case, in fact, the energy comes at most from noise and scattered multipath components. Differently, with the first 4 histograms, it is possible to appreciate the difference in terms of received power related to the response of the 4 antennas considering the different rotations.

In Fig. 68 the same results of Fig. 67 are offered but considering the first path only for the received power calculation. In fact, in this case, the received power was obtained as the ratio between the energy measured integrating the receiving signal around its peak (corresponding to the first path in line-of-sight (LOS)) for a duration equal to the pulse width, and the PRP duration. Due to this fact, the received power is lower since, now, it is less affected by the multipath components. The general behavior of the different antennas is anyway confirmed.

⁷Then, this result includes the effects of the receiver amplifiers.

4.3.3 Backscattering Characteristics of the GRETA Antenna

In this section some results obtained with the GRETA test-bed considering the ad-hoc developed UHF-UWB tag antenna are presented.

RX Energy [pJ]	RX Power [dBm]	RX Energy [pJ]	RX Power [dBm]
Overall received signal		First path only	
70 cm - Pol. 1 w/o UHF			
1,86E-03	-27,29	1,48E-03	-28,29
1,51E-03	-28,20	1,08E-03	-29,68
1,31E-03	-28,82	1,03E-03	-29,85
1,79E-03	-27,47	1,31E-03	-28,83
1,83E-03	-27,37	1,39E-03	-28,57
2,08E-03	-26,81	1,58E-03	-28,02
1,75E-03	-27,55	1,35E-03	-28,68
2,00E-03	-26,98	1,51E-03	-28,19
1,93E-03	-27,13	1,48E-03	-28,30
2,07E-03	-26,83	1,47E-03	-28,33
1,81E-03	-27,44	1,37E-03	-28,67
2,45E-04	0,63	1,83E-04	0,62

Figure 69: Received power from the GRETA antenna.

Fig. 69 presents the results of 10 consecutive measurements related to the UWB backscattering. For each measurement (each line) the received energy and power of the backscattered signal are presented, both considering the energy computed integrating all the multipath components and integrating the waveform around the first path only. In the last two lines the average values and standard deviations around the 10 measurements are reported. As expected, the received energy/power considering all the received waveform are larger with respect to the relative values considering the first path only, due to the presence of multipath components.

RX Energy [pJ]	RX Power [dBm]	RX Energy [pJ]	RX Power [dBm]	RX Energy [pJ]	RX Power [dBm]	RX Energy [pJ]	RX Power [dBm]
Overall received signal		First path only		Overall received signal		First path only	
70 cm - Pol. 1 w/o UHF				70 cm - Pol. 2 w/o UHF			
1,86E-03	-27,29	1,48E-03	-28,29	1,98E-03	-27,02	1,70E-03	-27,68
1,51E-03	-28,20	1,08E-03	-29,68	1,99E-03	-27,01	1,65E-03	-27,82
1,31E-03	-28,82	1,03E-03	-29,85	1,59E-03	-27,97	1,14E-03	-29,43
1,79E-03	-27,47	1,31E-03	-28,83	2,15E-03	-26,67	1,84E-03	-27,34
1,83E-03	-27,37	1,39E-03	-28,57	2,10E-03	-26,76	1,65E-03	-27,82
2,08E-03	-26,81	1,58E-03	-28,02	1,53E-03	-28,15	1,24E-03	-29,07
1,75E-03	-27,55	1,35E-03	-28,68	1,64E-03	-27,83	1,20E-03	-29,22
2,00E-03	-26,98	1,51E-03	-28,19	1,90E-03	-27,21	1,51E-03	-28,20
1,93E-03	-27,13	1,48E-03	-28,30	1,50E-03	-28,22	1,18E-03	-29,29
2,07E-03	-26,83	1,47E-03	-28,33	1,74E-03	-27,57	1,45E-03	-28,37
1,81E-03	-27,44	1,37E-03	-28,67	1,81E-03	-27,44	1,45E-03	-28,42
2,45E-04	0,63	1,83E-04	0,62	2,41E-04	0,58	2,53E-04	0,77

Figure 70: Received power from the GRETA antenna: polarization effect.

In Fig. 70 the GRETA antenna was characterized considering two different polarizations. In this case, the antenna is circularly polarized, then it was rotated of 45° around its axis by maintaining its face pointing towards the reader antenna. The received power, depicted in the figure, was -28.67 dBm in average for one polarization and -28.42 dBm in average for the antenna rotated of 45° . This fact

confirms the perfect circular polarization which ensures a good tag reading independently of the tag orientation when the antenna is pointed towards the reader.

RX Energy [pJ]	RX Power [dBm]	RX Energy [pJ]	RX Power [dBm]	RX Energy [pJ]	RX Power [dBm]	RX Energy [pJ]	RX Power [dBm]
Overall received signal	First path only	Overall received signal	First path only	Overall received signal	First path only	Overall received signal	First path only
70 cm - Pol. 2 w. UHF				70 cm - Pol. 2 w/o UHF			
1,24E-03	-29,06	1,00E-03	-29,97	1,98E-03	-27,02	1,70E-03	-27,68
1,84E-03	-27,34	1,50E-03	-28,23	1,99E-03	-27,01	1,65E-03	-27,82
1,44E-03	-28,40	1,21E-03	-29,15	1,59E-03	-27,97	1,14E-03	-29,43
1,20E-03	-29,20	9,18E-04	-30,36	2,15E-03	-26,67	1,84E-03	-27,34
1,75E-03	-27,55	1,44E-03	-28,39	2,10E-03	-26,76	1,65E-03	-27,82
1,07E-03	-29,68	8,60E-04	-30,65	1,53E-03	-28,15	1,24E-03	-29,07
1,10E-03	-29,58	8,91E-04	-30,49	1,64E-03	-27,83	1,20E-03	-29,22
1,69E-03	-27,71	1,29E-03	-28,88	1,90E-03	-27,21	1,51E-03	-28,20
1,35E-03	-28,69	1,08E-03	-29,66	1,50E-03	-28,22	1,18E-03	-29,29
1,37E-03	-28,64	1,10E-03	-29,58	1,74E-03	-27,57	1,45E-03	-28,37
1,41E-03	-28,58	1,13E-03	-29,54	1,81E-03	-27,44	1,45E-03	-28,42
2,73E-04	0,83	2,27E-04	0,86	2,41E-04	0,58	2,53E-04	0,77

Figure 71: Received power from the GRETA antenna: UHF/UWB decoupling.

Fig. 71 shows the performance of the GRETA antenna for what concerns the UWB/UHF decoupling capability. In fact, this single-port multi-band antenna incorporates a wideband diplexer capable of dividing the UHF and UWB signals. Then, the UWB response was measured in the presence of a continuous wave (CW) transmitted UHF signal of +30 dBm power at 868 MHz, with a panel antenna pointed towards the multi-band GRETA tag antenna positioned at 2 m distance. The results shown in Fig. 71, where the received power in the UWB band is presented in absence and in presence of the UHF signal, confirm the good decoupling between the two branches. In fact, the presence of the UHF signal does not degrade the UWB backscattered power which present a small decreasing of around 1 dB.

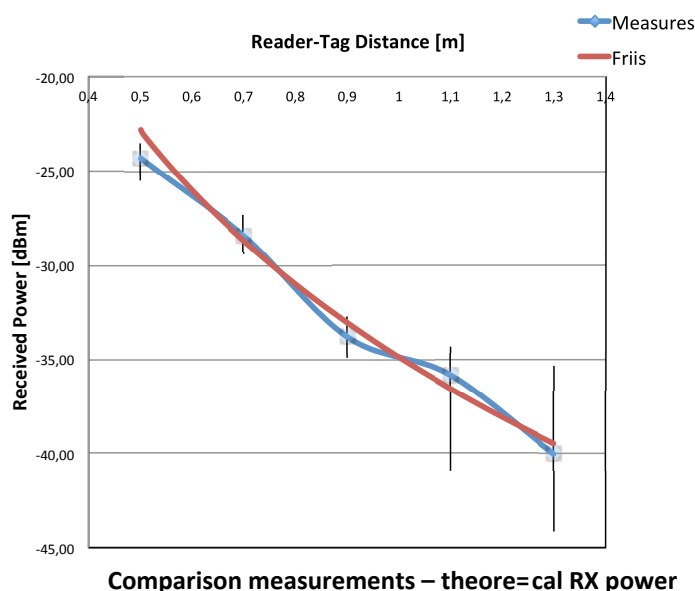


Figure 72: Received power from the GRETA antenna as a function of the reader-tag distance.

Finally, Fig. 72 presents the received power from the GRETA antenna as a function of the reader-tag

distance⁸. For comparison, the theoretical received power obtained from the Friis transmission equation was plotted, considering the gain/losses values of all the components composing the measurement chain and an additional loss of 3dB. As it is possible to notice, there is a very good agreement between the expected power and the measurement power, for what concerns both the absolute value and the behavior with respect to the distance.

4.3.4 Signal Processing Impact

In this section, the effects of the different choices in terms of signal processing parameters are investigated. In particular, the effects of the number of accumulated pulses N_s and of the oversampling factor OF are investigated. As figures of merit, the estimated received power from the tag backscattering, and the signal-to-clutter ratio (SCR) are considered. The received power should be, theoretically, independent of both N_s and OF since it is related to the tag backscattering capability only. However, since it is measured after the processing blocks discussed in the previous sections, it can be affected by some parameter choices. For further convenience, and in line with the processing usually done for signal TOA estimation to enable tag localization, the received signal of length T_p is divided in N_b energy bins, each related to energy of the waveform in a particular time interval. Specifically, since $T_p = 50\text{ ns}$ in the conducted measurements, $N_b = 50$ bins of 1 ns width were considered. Starting from the energy profile composed by the ordered set of all the bins, the SCR was defined as the ratio between the energy related to the largest bin (corresponding to the signal TOA, i.e., the first path of the tag backscattered signal) and the energy of the first 3 bins, usually containing noise and possible residual signals of the direct TX-RX reader antennas coupling.

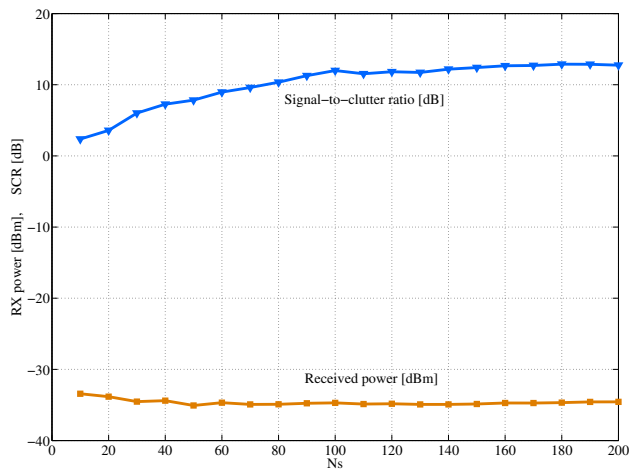


Figure 73: Impact of N_s on the estimated received power and on the SCR.

Fig. 73 shows how the estimated backscattered power and SCR behave as a function of N_s . It is possible to notice that, with small N_s (few accumulate pulses) the SCR is lower due to the presence of more noise in the signal. The estimated power is robust with respect to N_s . In general, considering $N_s > 100$ both the results are very stable and the processing output can be considered reliable.

Examples of the received signals and energy profiles for two different values of N_s are given in Fig. 74. It is possible to see that with $N_s = 20$ the signal is much more buried in noise but, from the energy profile on the right, it is clear the first path of the tag backscattered signal starting from bin 15 (i.e., TOA of 15 ns). Differently, adopting $N_s = 200$, the noise level is much lower than in the previous case and the energy profile results very clean, leading to a more reliable detection and correct TOA estimation.

⁸The power obtained integrating the received signal around the first path was considered.

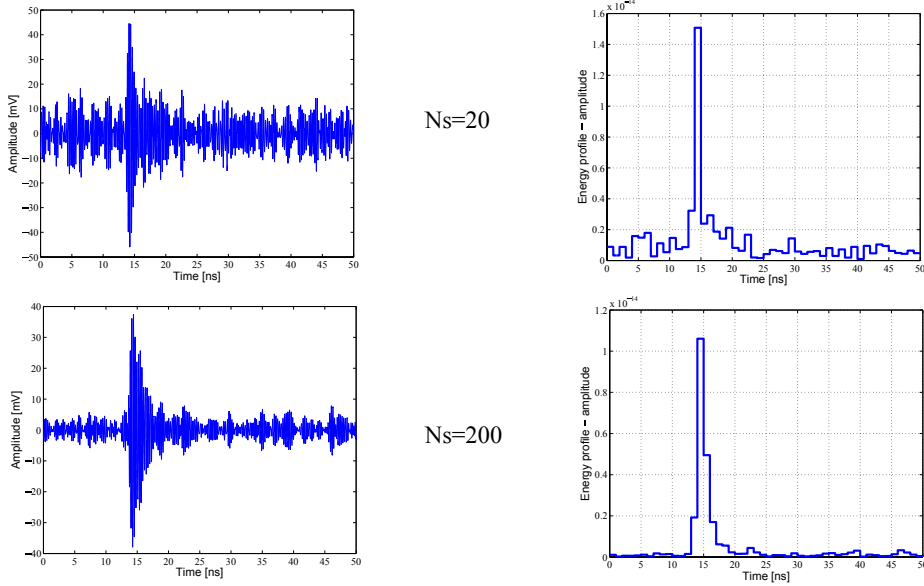


Figure 74: Example of impact of N_s on the received waveform.

In Fig. 75 the effect of the oversampling is shown. As before, the estimated power and the SCR are considered as figures of merit as a function of the oversampling factor OF. Results are given for three different values of N_s , that are, $N_s = 50$, $N_s = 100$ and $N_s = 200$. Looking at the figure, it is clear as an oversampling factor $OF > 25$ is necessary to obtain reliable measurement results. In fact, if OF is too low, we experience oscillations in the SCR and a potential wrong estimation of the received backscattered power from tag. These facts are due to the presence of clutter residuals on the received waveform, not properly canceled out by the processing scheme. Differently, when a proper value of OF is considered, the results are very stable and the processing output can be considered reliable.

Practical examples of these effects can be found in Fig. 76. In the upper part the received waveform (after the processing) and the related energy profile are shown without considering any form of oversampling. Differently, the same signals are reported in the bottom part of the figure considering $OF = 25$ in the processing chain. It is clear as, without oversampling, large clutter residuals are present. These clutter residuals impact the waveform in time instants before the signal TOA, then can confuse a detection or TOA estimation algorithm and must be avoided.

4.3.5 Code Effects

The following results consider the effect of the spreading code adopted at tag side on the measurement results. In particular it is shown how the rate of switching between open and short circuit impacts the performance. Histograms in Fig. 77 show the estimated received power and SCR for different switching rates, that is, different values of the pulses per chip N_{pc} . Specifically, $N_{pc} = 5$, $N_{pc} = 10$, $N_{pc} = 20$, $N_{pc} = 50$ and $N_{pc} = 100$ are considered, always with $N_s = 200$. The general behavior shows a decreasing of the SCR if N_{pc} increases. At the same manner, the estimated power slightly increases. The decreasing of the SCR can be explained with the progressive born and increase of clutter residuals not properly canceled out by the processing scheme. In fact, when the tag switches frequently between open and short loads, to consecutive responses are immediately summed up, after the multiplication for the expected code value, so that the clutter cancels out. Differently, when a low switching rate between open and short is considered, many responses are accumulated and are summed up. Then, if few differences are present between the responses due to time-distant pulses (e.g., the first pulse related to open circuit and the 101th pulse related to short circuit) the clutter cancelation could not be ideal, then increasing the SCR.

This fact is confirmed by Fig. 78 where the received signals and energy profile are shown considering

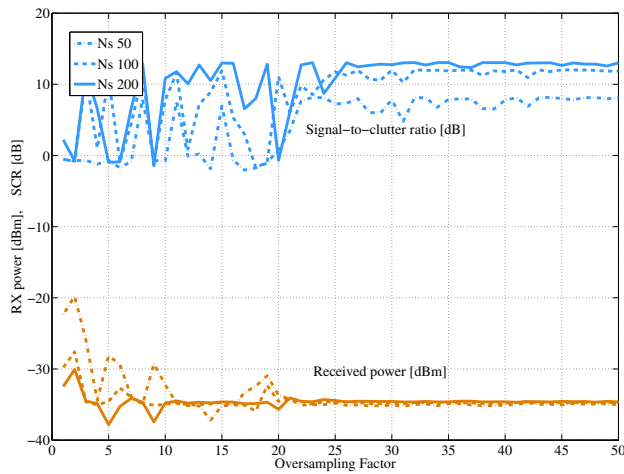


Figure 75: Impact of the oversampling on the estimated received power and on the SCR.

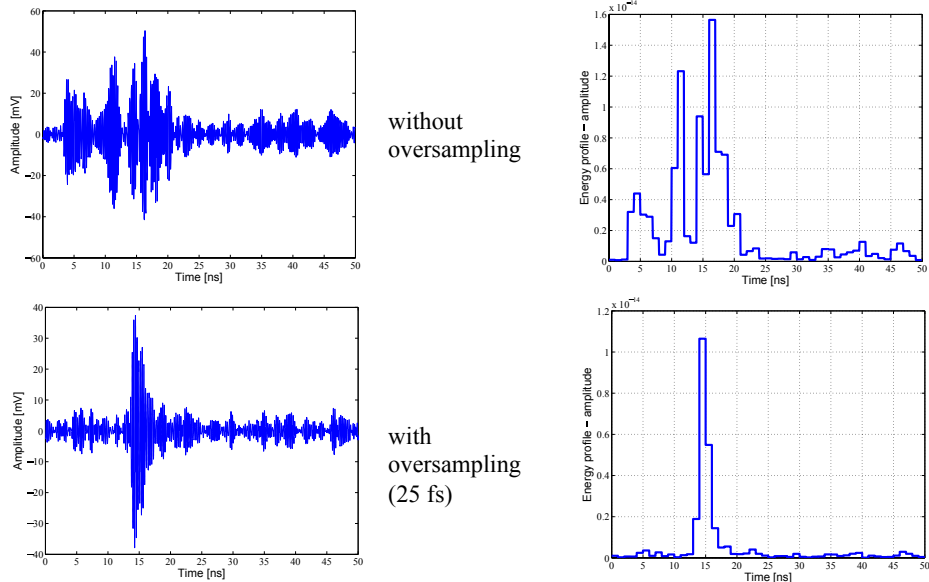


Figure 76: Example of impact of the oversampling on the received waveform.

$N_{pc} = 5$ (top) and $N_{pc} = 100$ (bottom). In the case of $N_{pc} = 5$ the tag signal and energy profile are very clean. Differently, when $N_{pc} = 100$, a clutter residual arises in the first 5 – 10 ns of the received waveform, mainly due to the strong TX-RX antenna coupling not properly canceled out by the processing algorithm. Notice that this effect translates in a small energy bins before the tag signal TOA then, if the detection/estimation is properly designed, it does not impact the performance, especially for small reader-tag distance (i.e., large tag signal SNR).

4.3.6 Order-of-arrival Results

To validate the approach presented in Sec. 4.2.8 through the test-bed, we collected a measurement dataset has been collected by varying the distance between the reader and the tag with a 0.30cm step from 0.30cm to 3m. For each position, the range measurement is taken in the absence and in the presence of an obstacle. Two kind of obstacles have been used: (1) a monitor inside a paper box and (2) a stack of books in a paper box. For each configuration and position, 10 different measurements of the energy bin \mathbf{e}

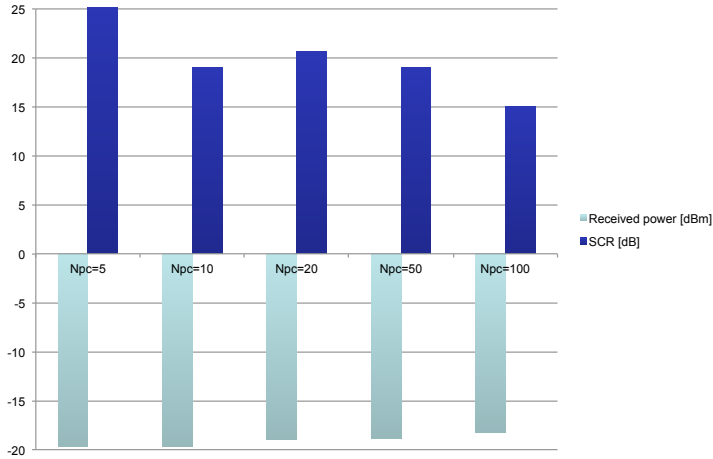


Figure 77: Impact of the code length on the estimated received power and on the SCR.

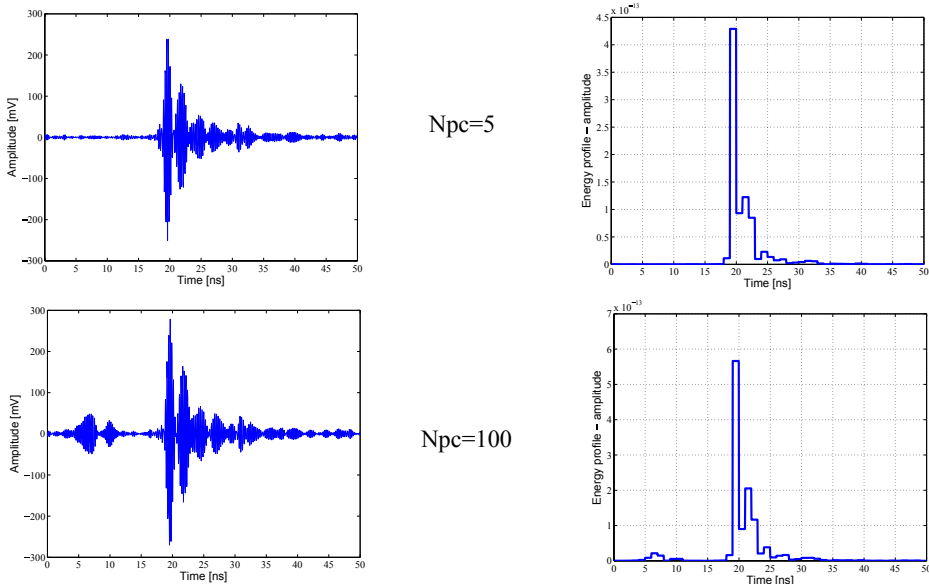


Figure 78: Example of impact of the code length on the received waveform.

have been taken. The collected bins have been processed to extrapolate an empirical distribution function $\hat{f}_Z(\mathbf{p}|\mathbf{z})$. Based on such empirical functions, the OOA estimation of a stream with $N_o = 3$ objects has been simulated using both soft-decision and hard-decision. Results have been obtained by varying also the distance Δ between two consecutive objects.

Results are obtained in terms of absolute rate, which is defined as

$$R_a = 1 - \frac{\delta(\mathbf{o}, \boldsymbol{\omega}_i)}{N_o} \frac{\#\{\hat{\mathbf{o}} = \boldsymbol{\omega}_i\}}{\# \text{trials}} \quad (20)$$

where $\delta(\mathbf{o}, \boldsymbol{\omega}_i)$ is the Hamming distance between \mathbf{o} and $\boldsymbol{\omega}_i$; and in terms of correct rate, which is defined as

$$R_c = \frac{\#\{\hat{\mathbf{o}} = \mathbf{o}\}}{\# \text{trials}}. \quad (21)$$

Fig. 4.3.6 and Fig. 4.3.6 show the absolute rate for $\Delta = 0.15, 0.30, 0.45$, and 0.60m in the presence and in a absence of the obstacle. Fig. 4.3.6 and Fig. 4.3.6 shows the correct rate for $\Delta = 0.15, 0.30, 0.45$, and

0.60 m in the presence and in a absence of the obstacle. Both R_a and R_c increase as the objects are more distant from each other, i.e., as Δ increases, and the performance win the soft-decision case are better or equal than the hard-decision case.

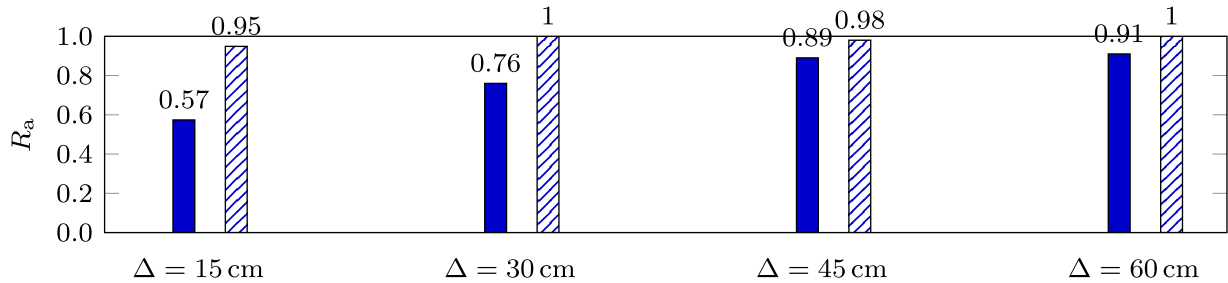


Figure 79: Absolute rate in NLOS conditions for different values of Δ with hard-decision (solid pattern) and soft-decision (dashed pattern).

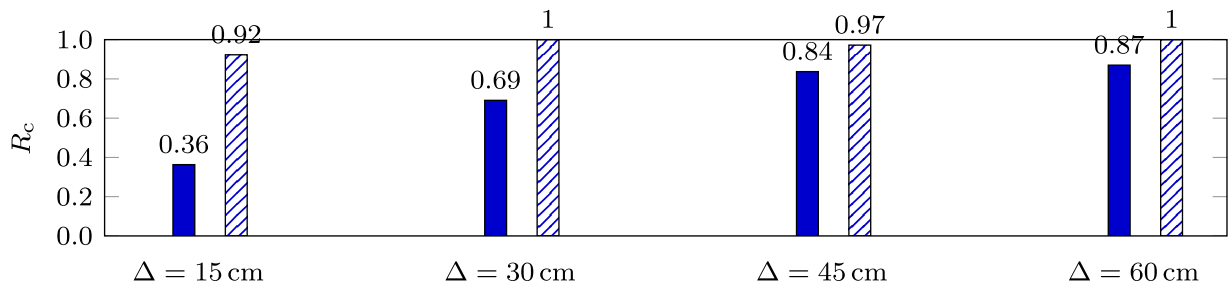


Figure 80: Correct rate in NLOS conditions for different values of Δ with hard-decision (solid pattern) and soft-decision (dashed pattern).

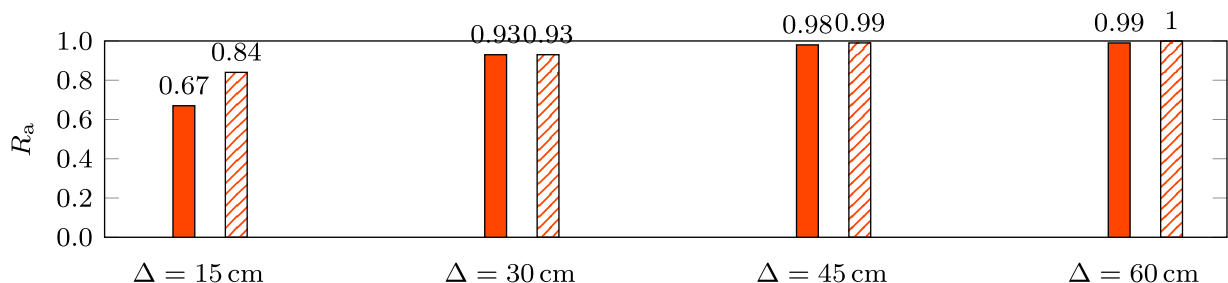


Figure 81: Absolute rate in LOS conditions for different values of Δ with hard-decision (solid pattern) and soft-decision (dashed pattern).

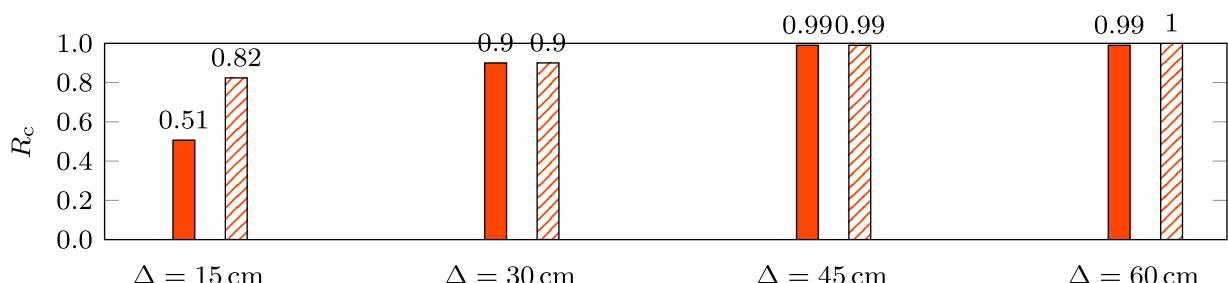


Figure 82: Correct rate in LOS conditions for different values of Δ with hard-decision (solid pattern) and soft-decision (dashed pattern).

5 MAIN ACHIEVEMENTS

5.1 Components on Recyclable Material Substrates

5.1.1 Green Technologies

This section presents the improvement in the manufacturing technique of green, eco-compatible and cost effective SIW microwave passive components. The proposed process for the implementation of SIW circuits on paper consists of two steps: the preliminary preparation of the metallized paper substrate and the manufacturing of the circuit, which requires both milling machining and subsequent metallization of the via holes.

Beside the fabrication process, the electromagnetic characterization of the involved materials is presented. Finally, the design and the measurement of several prototypes of SIW microwave devices are reported.

Substrate preparation

The preparation of the substrate requires, as a first step, the selection of a suitable type of paper with the proper thickness. The thickness of the substrate plays a role in the overall loss of SIW components: in fact, conductor loss in a SIW structure decreases when increasing the substrate thickness, whereas the dielectric loss is independent from the thickness. Consequently, the substrate thickness should be large enough, to guarantee that conductor loss is small compared to dielectric loss. If available, a single paper sheet is adopted; otherwise, a few paper sheets can be stacked and glued, in order to reach the required thickness. Of course, the latter approach leads to a more complex (and less reliable) technological process. In this work, a single paper layer with a thickness of 500 μm has been used.

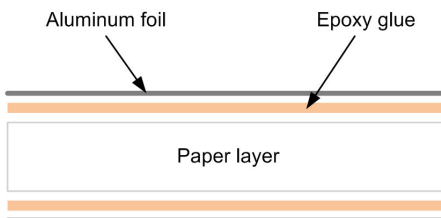


Figure 83: Side view of the metalized paper substrate, consisting of a stack of paper layer and aluminum foils, attached by epoxy glue.

Differently from traditional laminated substrates, which are commercially available with top and bottom metallization, the paper substrate requires metal sheets to be attached on both faces. To this aim, the paper sheet is embedded between two aluminum foils with a thickness of 20 μm (Fig. 83), which are attached by epoxy glue. The stack of paper sheet and aluminum foils is pressed and heated in a thermal oven for four hours at 65 Celsius degree. Since the stack is pressed while the glue is not yet completely solid, the thickness of the glue is only few microns and it results negligible with respect to the paper thickness. The main reason for using epoxy glue is the achieved stiffness of the glue layer, that permits an easy manufacturing process by milling machining, as detailed in the next Section.

Manufacturing of the SIW circuit

The manufacturing of the SIW circuit on paper is based on the use of a numerical controlled (CNC) milling machine, namely a ProtoMat E33 from LPKF Laser & Electronics AG. This machine is adopted both for the surface patterning and for the hole drilling, as in a standard PCB fabrication process. The milling machine can be equipped with two main types of tools: the spiral drills and the cutters. The first ones are employed to drill the via holes, with diameter spanning from 0.2 mm to 2 mm. The cutters are

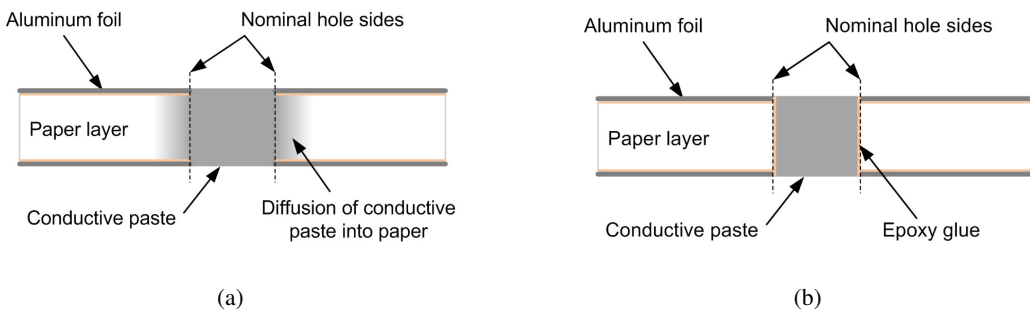


Figure 84: Effect of different techniques for the metallization of the via holes: (a) direct use of the conductive paste, with diffusion of the paste into paper; (b) preliminary coating of the hole walls by epoxy glue, which prevents conductive paste diffusion.

used both to etch thin gaps between strips and to remove wide areas of metal foil, and the available cutters diameter ranges from 0.15 mm to 3 mm.



Figure 85: Photographs of the steps of manufacturing of the metalized via holes.

Finally, the via holes of the SIW structure need to be metallized. A conductive paste is adopted to fill the drilled holes, to guarantee ohmic contact between top and bottom conductive layer. Several experiments showed that the direct use of conductive paste is critical, as the conductive paste diffuses in the substrate because of the porosity of the paper, thus jeopardizing the metallization process (Fig. 84a). To overcome this problem, a two-steps metallization process was adopted. A preliminary coating thin film of epoxy glue is distributed on the inner wall of via holes, to avoid the aforementioned diffusion effect (Fig. 84b). A fast heating process is required to cure the coating. The second step is the metallization process with the conductive paste. A final heating process in a thermal oven is required to increase the conductivity of the conductive paste. The implementation process of the metal via holes is shown in Fig. 85, with a four-hole pattern test bench.

By using this new fabrication method the costs of material and manufacturing are extremely low. Moreover, the proposed technique is suitable for SIW components and can be applied to other non-standard substrates.

Material characterization

The use of paper-based substrates for the implementation of microwave components requires a preliminary characterization of the electric parameters of the adopted materials. In particular, it is necessary to measure the dielectric permittivity and the loss tangent of paper and the conductivity of the aluminum foils.

This section presents, at first, the experimental determination of the conductivity of the aluminum foils, which is independent from the selected paper material. Subsequently, test circuits are realized on paper substrates, to determine the electric properties of paper.

Measurement of aluminum foil conductivity

The technique adopted to characterize the conductivity σ of the aluminum foils is based on a cylindrical cavity resonator, operating at 2.45 GHz on the fundamental TM₀₁₀ mode. In fact, the quality factor of the cavity mode depends on the wall conductivity. Two cavities have been considered: in the first case, the top and bottom walls of the cylindrical cavity consist of bulky copper, while in the second case they are replaced by the aluminum foils.

The experimental setup consists of the cavity, connected through two ports to a vector network analyzer (VNA). Weak coupling is achieved by properly adjusting input/output feeding loops, in such a way that the loaded quality factor well approximates the unloaded one.

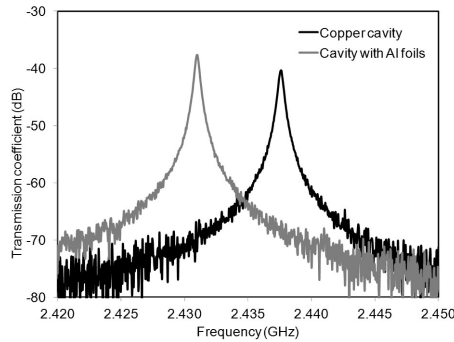


Figure 86: Measured $|S_{21}|$ of the resonant cavity adopted for the characterization of the aluminum foil conductivity: cavity with copper top and bottom (black line) and with aluminum foil (gray line).

Fig. 86 shows the measured transmission coefficient of the cavity in the two cases. The unloaded quality factor can be derived from the scattering parameters and it results approximately 6000 for both cases. Because the difference between the quality factor in the two cases is negligible, the conductivity of the aluminum foil is comparable to the copper conductivity. For this reason, the conductivity value $\sigma=3.5 \times 10^7$ S/m was adopted in the simulations. In addition, Fig. 86 shows a small frequency shift of 6.6 MHz between the two resonances: this phenomenon is attributed to the small bending of the thin aluminum foils, which was confirmed by numerical simulations.

Electrical characterization of paper

There is wide availability of different types of paper, which vary in density, thickness, and texture. However, since paper is not developed specifically for microwave applications, accurate information about its electric properties are not readily available. Therefore, it is essential to adopt a systematic process for determining the dielectric permittivity ϵ_r and the loss tangent $\tan\delta$. Several methods are currently used to characterize microwave substrates, including resonators and transmission lines. The method adopted in this work is based on the study of the frequency response of a microstrip ring resonator. This technique permits to determine the dielectric permittivity of the substrate from the analysis of the resonance frequencies of the ring, and the loss tangent from the evaluation of the quality factor of the resonant modes.

Several different types of papers have been characterized by adopting this technique. In all cases, a proper ring resonator has been designed and tested. The structure of the circuit consists of a microstrip ring, as shown in Fig. 87a, coupled to the input and output 50 Ohm microstrip lines through two gaps. The value of the gap was selected, taking into account the constraints of the manufacturing process. In the design, the terminal sections of the microstrip lines near the ring were increased to increase the capacitance, and consequently to achieve a larger coupling.

The frequency response of the ring resonator presents a set of resonances at the frequencies where the length of the ring corresponds to an integer number of effective wavelengths (Fig. 87b). As the effective wavelength is related to the dielectric permittivity of the substrate, the value of ϵ_r is derived from the

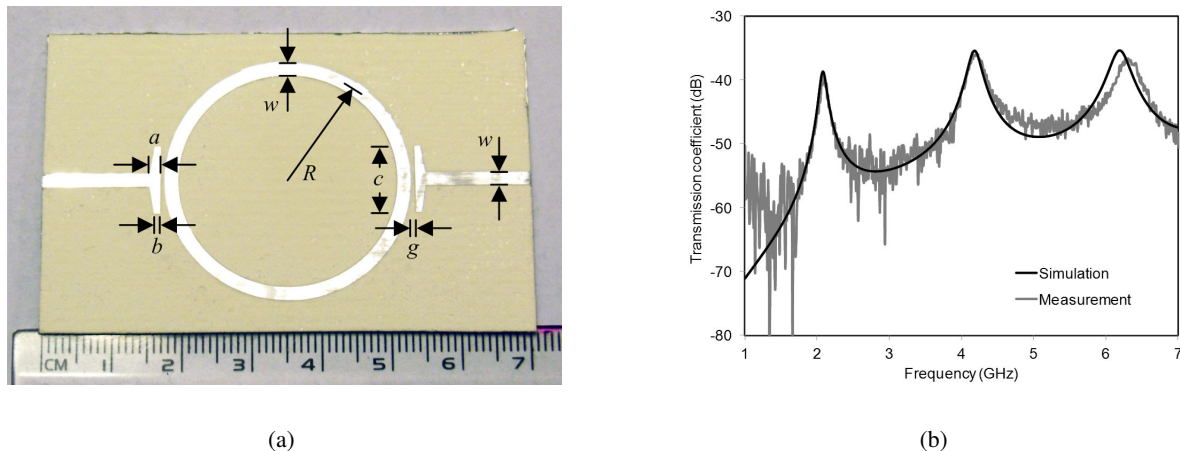


Figure 87: Example of a microstrip ring resonator on paper adopted for the material characterization (dimensions in mm: $w=1.9$, $g=0.65$, $R=16.8$, $a=1.5$, $b=0.8$, $c=9.9$): (a) photograph of the prototype; (b) simulated and measured $|S_{21}|$.

resonance frequencies of the ring resonator. Concerning the loss tangent of the paper substrate, it is mainly related to dielectric loss, as radiation loss is negligible and it was demonstrated in the previous subsection that the aluminum foils exhibit a high conductivity. Therefore, the value of $\tan\delta$ is derived from the measured unloaded quality factor, obtained from the insertion loss and the -3 dB bandwidth.

All ring resonators have been designed in order to have the first resonant frequency at 2 GHz, assuming the tentative value of dielectric permittivity $\epsilon_r=2.85$, taken from the literature.

Table 4: Electrical parameters of different types of paper substrates, derived from the measurement of ring resonators.

Paper type	Number of layers	Thickness μm	Dielectric constant	Loss tangent
Photographic paper	3	690	2.35	0.044
Fabriano Copy 2	6	480	2.13	0.060
Watercolor paper	1	300	2.09	0.045
Corrugated paper	1	1500	1.46	0.036
Raw paper	1	350	2.11	0.037
PM1	1	500	1.90	0.045
Momo 07	1	665	2.02	0.041
Fabriano 5	1	500	2.25	0.045
Burgo	1	500	2.20	0.040

The values of the relative permittivity and of the loss tangent of several different paper substrates, measured with the ring resonator technique, were determined, and the results are reported in Table 4. The values of ϵ_r and $\tan\delta$ were preliminarily determined by using the formulas in, and subsequently refined by using full-wave simulations to fit measurement data. The results show that the dielectric permittivity of the paper is in the range of 1.9-2.35 in the frequency band from 2 to 4 GHz for most types of paper, with the only exception of corrugated paper, which has a lower permittivity of 1.46 due to the large presence of air. The values of loss tangent range from 0.037 to 0.06.

Paper based components

Once the fabrication process achieved an acceptable level of reliability and the electromagnetic characteristics of the involved materials are known, the design, manufacturing and measurements of different

passive microwave components can be done. In particular, this Section presents several SIW components based on paper substrate.

These new designs are based on Burgo paper substrate which is a thick raw paper without any final glossy treatment. The dielectric permittivity is $\epsilon_r = 2.2$ and the loss tangent is $\tan \delta = 0.04$. The most important improvement with respect of the previous designs is that the thickness of a single sheet of paper is $500 \mu\text{m}$, that allows to use a single layer as dielectric substrate for the implementation of the SIW structures.

The proposed prototypes comprise an SIW cavity, two SIW interconnections, a two-pole SIW filter based on quarter-mode cavities and a cavity-backed SIW slot antenna. All these components have been designed with the commercial electromagnetic simulator Ansys HFSS, and the measurement setup is based on the vector network analyzer (VNA) Anritsu 37347C and the universal test fixture (UTF) Anritsu 3680.

SIW square cavity

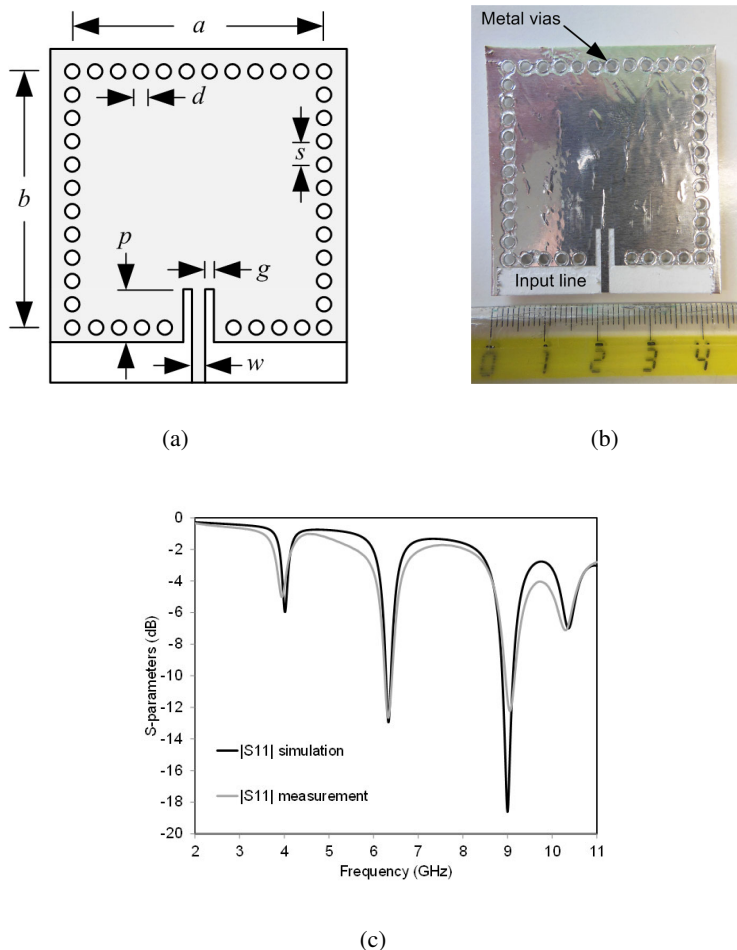


Figure 88: SIW cavity resonator on paper: (a) drawing of the SIW cavity (dimensions in mm: $a=b=36.5$, $d=2$, $s=4$, $w=1.6$, $g=1$, $p=7$); (b) photograph of the prototype; (c) simulated and measured $|S_{11}|$ of the cavity resonator.

A square SIW cavity on paper is designed to resonate at 4 GHz, which is the middle of the lower part of the standard UWB frequency band. The excited fundamental mode is the TM_{110} . The layout of the square SIW cavity is illustrated in Fig. 88a. The side dimension of the optimized cavity is $a=b=36.5$

mm in order to center the desired resonant frequency, the via holes have a diameter of $d=2$ mm, and their spacing is $s=4$ mm (that is the double of the diameter), to practically avoid radiation leakage. The cavity is fed by a 50 Ohm microstrip line, with two symmetric insets to control the coupling. The relevant dimensions of the structure are provided in the caption of Fig. 88a.

Table 5: Simulated and measured resonance frequency and quality factor of the first cavity modes.

Resonant mode	Simulated f_r (GHz)	Measured f_r (GHz)	Simulated Q_U	Measured Q_U
Mode TM ₁₁₀	4.02	3.95	20.9	10.9
Mode TM ₂₁₀	6.33	6.33	19.3	11.8
Mode TM ₃₁₀	9.00	9.05	15.3	11.8

Fig. 88b shows a photograph of the prototype. The comparison of simulated and measured reflection coefficient of the circuit is shown in Fig. 88c. In the considered frequency band from 2 GHz to 11 GHz, the frequency response of the SIW cavity exhibits four poles, corresponding to four resonant modes of the cavity. The good agreement between simulation and measurement demonstrates that the values of ϵ_r and $\tan \delta$, determined at the frequency of 2 GHz in the previous section, do not change significantly over the entire frequency band. More specifically, Tab. 5 shows the simulated and measured resonance frequency f_r and unloaded quality factor Q_U of the first three cavity modes. The maximum discrepancy between simulated and measured resonance frequencies is in the order of 2%, and a reasonable agreement was found also in the values of the quality factors.

Moreover, the resonant cavity represents the basic element for the implementation of SIW filters, as the quality factor of the cavity is related to the achievable filter selectivity. The Q_U factor of the first mode of the SIW square cavity is approximately 11. To make a comparison, the quality factor of the ring resonator fabricated on the same paper is 17. This result is not surprising, as in the case of the SIW cavity the field is completely confined inside the (quite lossy) dielectric material, whereas in the case of the microstrip ring resonator the field is partially in the dielectric material and partially in air, thus reducing the overall dielectric losses. Beside this issues, SIW cavity resonators, as well as SIW components, are completely shielded and consequently the radiation losses are negligible. This leads to the possibility of stacked more layers of SIW components without changing their frequency behaviors and also to prevent spurious perturbations from the external environment.

SIW and HMSIW interconnections

As presented before, another classical component is the straight interconnection, that is essential for the implementation of microwave circuits. As discussed the main difference between the previous prototypes is related to the substrate adopted. In this case the single sheet of Burgo paper is employed in order to keep as simple as possible the manufacturing of the substrate and therefore to achieve a more reliable manufacturing process. Two different topologies of SIW interconnections are proposed: the standard SIW and a half-mode SIW (HMSIW). Both interconnections exhibit tapered transitions to input and output 50 Ohm microstrip lines, in order to measure the scattering parameters of the circuits by using a vector network analyzer. The measurement setup is still the same of the previous case.

The basic SIW interconnection is designed to cover the lower part of the ultra-wideband (UWB) frequency range, from 3.1 GHz to 4.8 GHz. Consequently, the cut-off frequency of the SIW is set to $f_C = 2.5$ GHz, so that the useful band starts at $1.25 f_C = 3.1$ GHz, according to the usual definition. To this aim, the unit cell of the SIW structure has been designed with the diameter of via holes $d=2$ mm, the longitudinal spacing $s=4$ mm, and the width of the SIW $w=40.7$ mm (Fig. 89a). The overall length of the circuit is set to $L=48$ mm, corresponding to 12 unit cells.

The photograph of the top view of the prototype is shown in Fig. 89b. The frequency response of the SIW structure is shown in Fig. 89c, where the simulated and measured scattering parameters of the paper-based SIW interconnect are reported. An overall agreement between simulation and measurement results is observed. The measured insertion loss of the SIW structure, including input/output microstrip

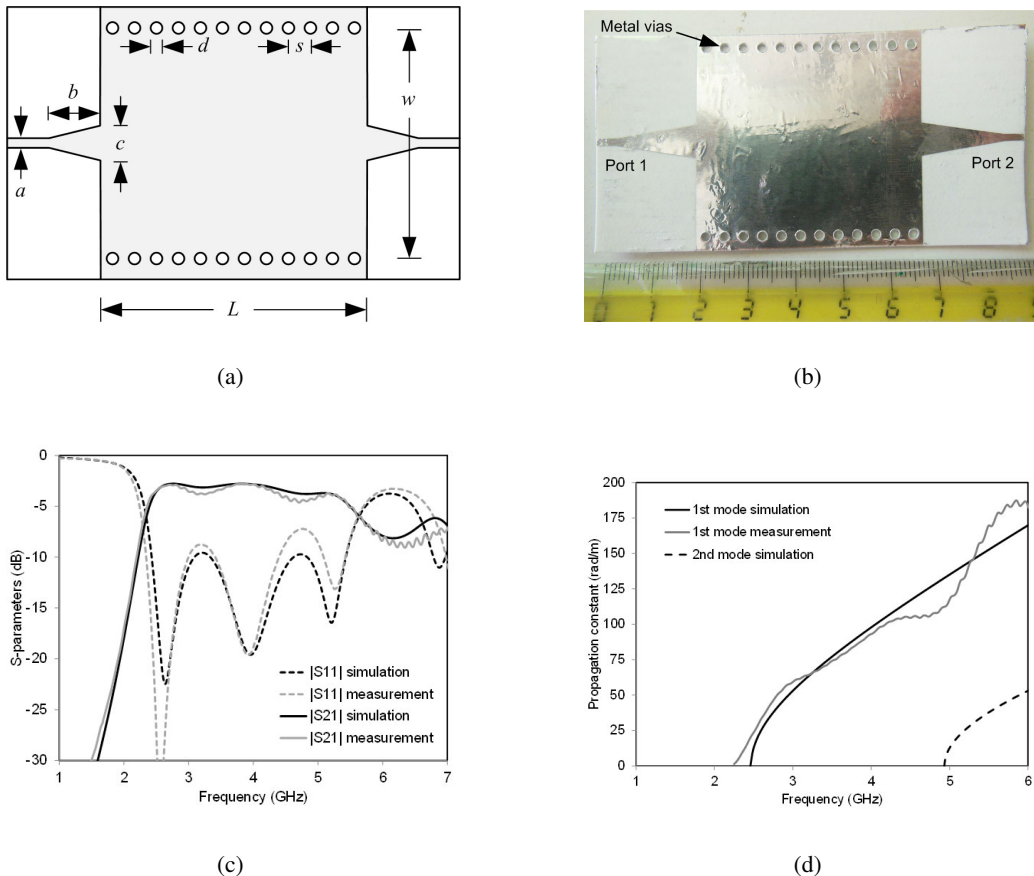


Figure 89: SIW interconnect on paper: (a) drawing of the SIW interconnect (dimensions in mm: $a=1.6$, $b=17$, $c=7.2$, $d=2$, $s=4$, $w=40.7$, $L=48$); (b) photograph of the prototype; (c) simulated and measured scattering parameters of the SIW interconnect; (d) simulated and measured dispersion diagram of the fundamental mode of the SIW interconnect.

lines and tapered transitions, is 2.83 dB at the frequency of 4 GHz. The dispersion diagram of the SIW structure is obtained by comparing two lines with different length (more specifically, a long structure with 12 unit cells and a short structure with 9 cells). The propagation constant versus frequency is shown in Fig. 89d. The attenuation constant of the SIW interconnection is estimated 0.3 dB/cm at 4 GHz.

The second interconnection based on paper substrate is the half-mode SIW. The structure is obtained by removing half of the top wall of the SIW interconnection, as well as a row of metal vias (Fig. 90a). The operation principle of this structure is based on the presence of a magnetic wall boundary condition along the cutting plane, which satisfies the boundary condition of the fundamental SIW mode. In addition, the radiation leakage through the open side remains negligible because of the low thickness of the substrate and therefore the high aspect ratio. The HMSIW exhibits two basic advantages: the size is reduced of almost 50% with respect to the standard SIW, and the single-mode bandwidth is significantly enhanced. The quasi- TE_{20} mode is not supported because of the magnetic wall condition, and the first upper mode is the quasi- TE_{30} that has the cut-off frequency three times higher with respect of the fundamental mode one.

The HMSIW was designed with the same $f_C = 2.5$ GHz of the SIW described above, thus resulting in the same longitudinal dimensions (as reported in Fig. 90a).

A prototype of the half-mode SIW was fabricated with the described technology and its picture is reported in Fig. 90b. The simulated and measured scattering parameters are shown in Fig. 90c and exhibit a good agreement over the entire frequency band. Moreover, the propagation constant of the HMSIW is

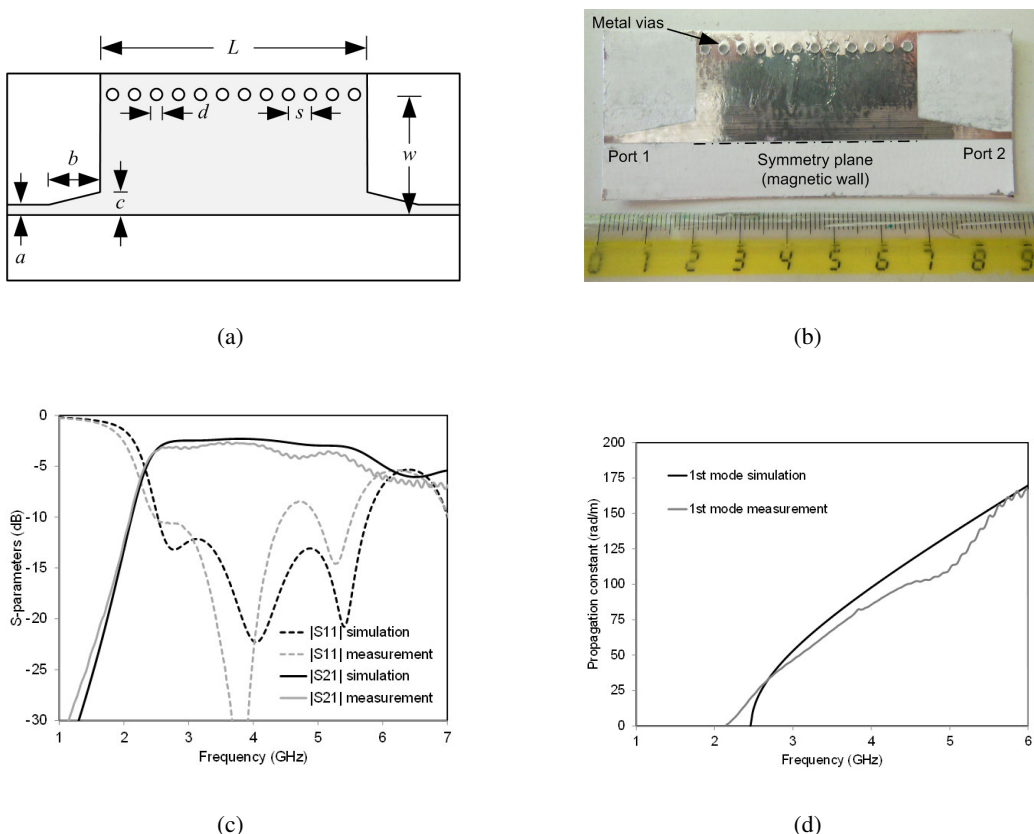


Figure 90: Half-mode SIW interconnect on paper: (a) drawing of the half-mode SIW interconnect (dimensions in mm: $a=1.6$, $b=16.8$, $c=4.8$, $d=2$, $s=4$, $w=20.4$, $L=48$); (b) photograph of the prototype; (c) simulated and measured scattering parameters of the half-mode SIW interconnect; (d) simulated and measured dispersion diagram of the fundamental mode of the half-mode SIW interconnect.

reported in Fig. 90d. The values of the propagation and attenuation constant of the HMSIW are similar to the ones of the standard SIW, being the only difference the much broader single-mode bandwidth. The propagation constant of the second mode starts at approximately 7.5 GHz that is out of scale in Fig. 90d.

Quarter-mode SIW filter

Another significant example presents a two-pole filter based on quarter-mode SIW cavities (Fig. 91a). The selected topology permits to minimize the filter size, as the cavity dimension is reduced of a factor four. The quarter SIW cavity exploits the same concept of the half-mode SIW structure: due to the particular aspect ratio, the two open sides of the quarter cavity practically exhibit magnetic-wall boundary conditions, thus supporting the fundamental $\text{TM}_{0.5,0.5,0}$ cavity mode.

The proposed filter consists of two quarter-mode SIW cavities, connected at one side, where the metal posts are removed. The input/output 50 Ohm microstrip lines are connected to the cavities, in the corner where the electric field assumes the maximum value.

The pass-band filter has been designed with central frequency at 4 GHz. The resulting cavity side is $w = 17.2$ mm, whereas the via diameter and spacing are $d = 2$ mm and $s = 4$ mm. The input/output microstrip lines are slightly tapered to optimize the input matching. The overall length of the device is approximately 50 mm. The dimensions of the circuit are given in detail in the caption of Fig. 91a.

Fig. 91b shows the top view of the prototype. The simulated and measured frequency responses of the filter are reported in Fig. 91c. The measured insertion loss is 2.9 dB at the frequency of 4 GHz.

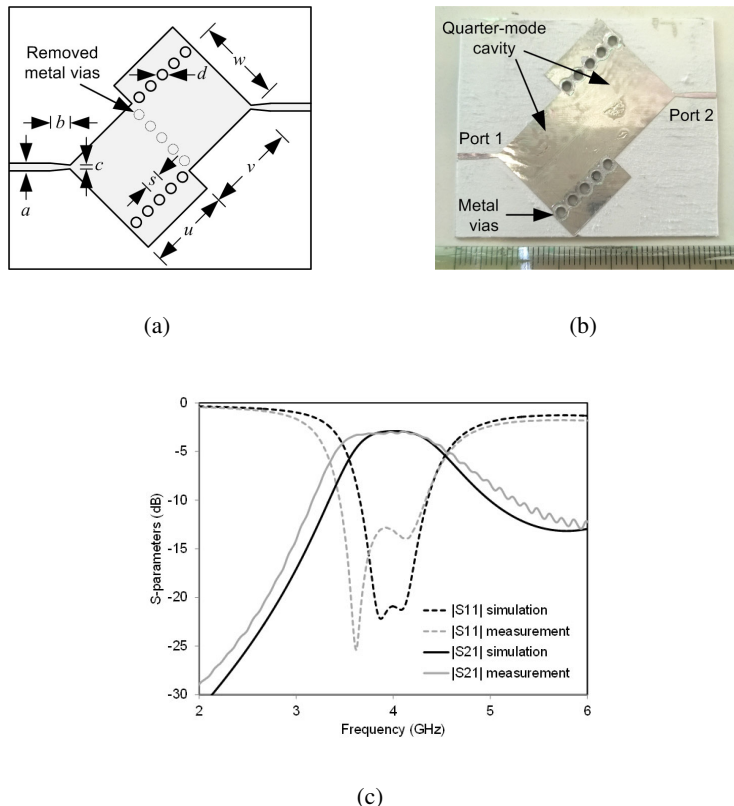


Figure 91: Quarter-mode SIW cavity filter on paper: (a) drawing of the SIW filter (dimensions in mm: $a=1.6$, $b=4.3$, $c=0.65$, $d=2$, $s=3.32$, $u=16.3$, $v=18.1$, $w=17.2$); (b) photograph of the prototype; (c) simulated and measured scattering parameters of the SIW filter.

Half-mode SIW filter

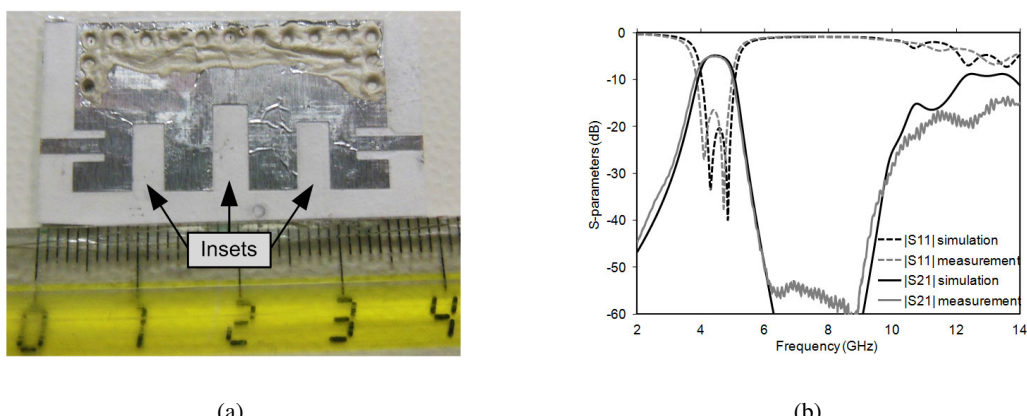


Figure 92: Low pass filter on paper substrate.

One more example in band-pass filter design based on this technology is a compact half-mode SIW filter. The design is based on the excitation and control of the resonance modes of a half-mode SIW cavity.

By properly selecting the dimension and position of three insets (Fig. 92a), the resonance frequency of the cavity modes can be adjusted, in such a way that two modes determine the pass band at 4.5 GHz

and the higher modes are shifted up to approximately 10 GHz (return band), thus guaranteeing a wide out-of-band region. The input matching is optimized by playing with the coupling with the input/output microstrip lines, which does not practically affect the mode resonance frequencies.

The prototype of the filter is shown in Fig. 92a the overall size is quite small, being its length less than 40 mm, including the input/output microstrip lines. The frequency response is reported in Fig. 92b and exhibits a very good agreement between simulation and measurement over the entire frequency band. The measured insertion loss is 5.0 dB at the frequency of 4.5 GHz.

Cavity-backed SIW slot antenna

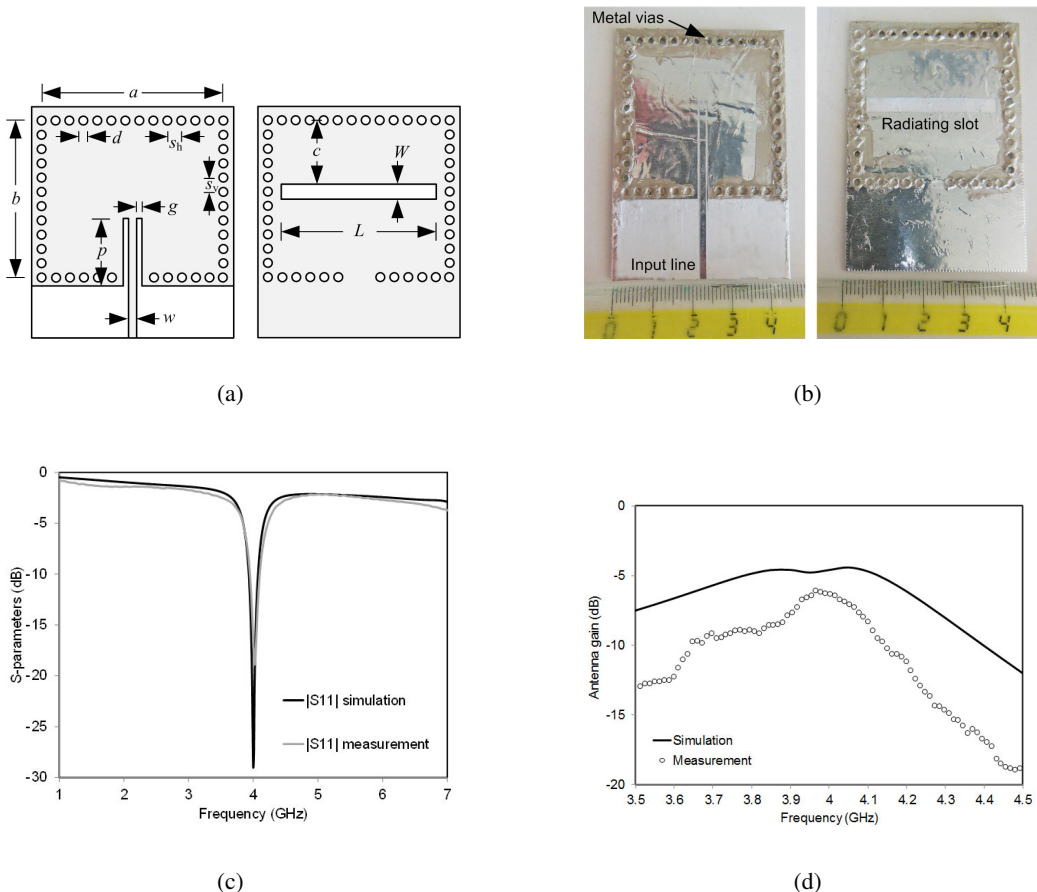


Figure 93: Cavity-backed SIW antenna on paper: (a) drawing of the SIW antenna (dimensions in mm: $a = b = 39.3$, $c = 17.18$, $d = 2$, $sh = 3.02$, $sv = 3.57$, $w = 1.6$, $g = 0.5$, $p = 25.25$, $L = 34$, $W = 4$); (b) photographs of the bottom and top side of the prototype; (c) simulated and measured input matching of the SIW antenna; (d) simulated and measured gain vs. frequency of the SIW antenna.

One more example is a cavity-backed SIW slot antenna, operating at the frequency of 4 GHz and with linear polarization (Fig. 93a). This antenna topology exhibits some important features: because it is completely shielded at the sides it does not suffer from side leakage, it is less sensitive to the environment. For these reasons, this type of antenna finds useful applications in wearable systems.

The antenna consists of a square SIW cavity with a rectangular slot on a side and a feeding line on the opposite side, as depicted in Fig. 93a. The size of the SIW cavity is selected to exhibit the TM_{120} resonant mode at the frequency of 4 GHz. Similarly, the length of the rectangular slot is optimized to radiate at the same frequency. The antenna is fed by a microstrip line with two insets, designed to optimize the input matching. All dimensions of the antenna are provided in the caption of Fig. 93a.

This circuit requires a double-face manufacturing process that implies an uncertainty in the alignment between top and bottom when the substrate is flipped. The photographs of the top and bottom sides of the prototype are shown in Fig. 93b.

The measured and simulated input matching of the antenna are reported in Fig. 93c, and they show a negligible variations in terms of resonant frequency of the antenna, thus fully validating the double-face manufacturing process. Finally, the simulated and measured gain of the antenna are shown in Fig. 93d. The measured gain of the antenna at the frequency of 4 GHz is -6.3 dB, corresponding to a radiation efficiency of 6.4%.

5.2 Autonomous RFID Tags

5.2.1 Antenna and external front-end

In order to prove the performance of the paper tag, several measurements of the prototype parts (i.d. antenna, diplexer, and tag) were conducted. At first, the antenna stand-alone was measured in terms of return loss. The comparison between modelled and measured data is reported in Fig. 94. Besides some slight frequency shift, especially for the higher frequencies, a very good agreement is observed.

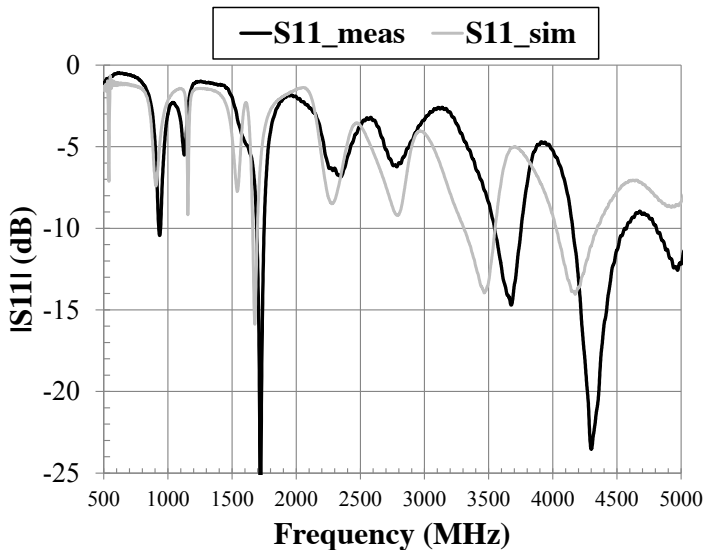


Figure 94: Simulated and measured magnitude of S11 of the paper antenna.

As a second investigation the diplexer UWB performance was measured in terms of scattering parameters. Both ports (port 1 and port 3) where loaded by the measurement instruments 50Ω terminations. Results are reported in Fig. 95: a good agreement can be observed also in this case.

As a further prove of the correct behavior of both the antenna and the UWB filter, their performance where tested again for the tag prototype. In this case the term of comparison is the reflection coefficient at the UWB port (port 3), when the microstrip filter is terminated by the antenna at port 1. The results are shown in Fig. 96.

Finally, the UHF network performance was evaluated. A separate measurement of the UHF lumped components filter and of the rectifier is not possible, therefore the UHF network behavior was measured for the tag as a whole in terms of RF-to-DC conversion efficiency. The measurements where performed in a real office environment. The tag was radiated by a transmitting antenna in the UHF band at 1 meter distance, emulating the reader operations, for different RF power levels. Since a direct evaluation of the incident power level at the diplexer UHF input is not possible, a reference antenna, identical to the one of the tag, is first used to estimate the RF power level incident on the antenna. Then, in the same condition, the reference antenna is substituted by the tag and the rectified voltage on the optimum load is measured.

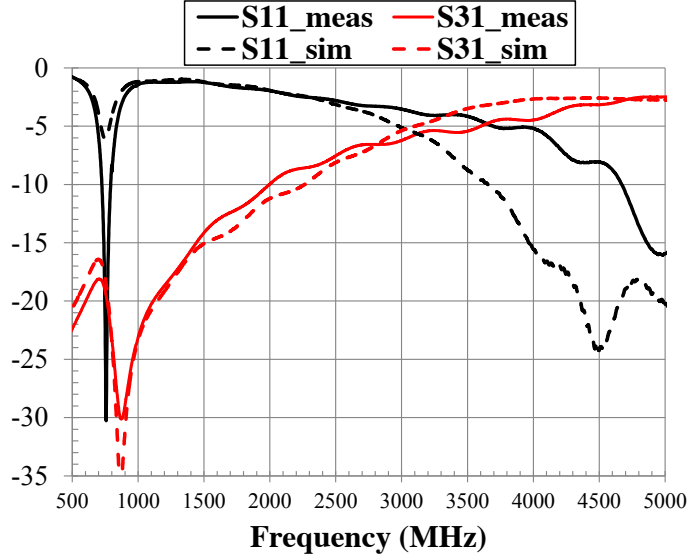


Figure 95: Comparison between the simulated and measured UWB filter performance.

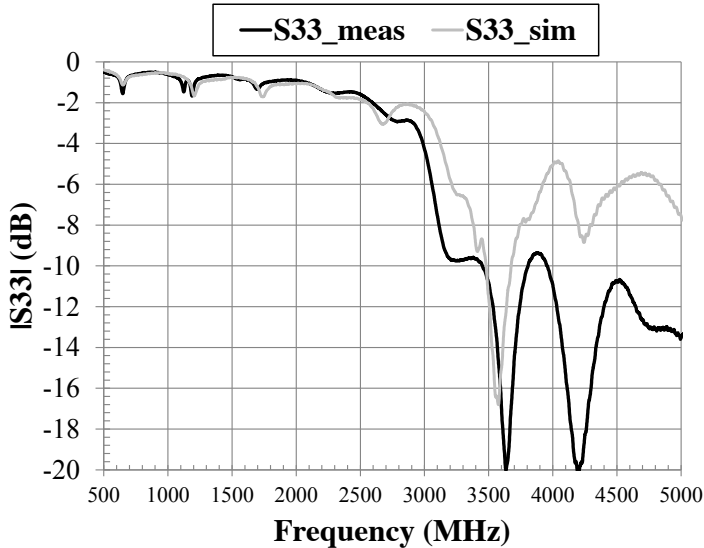


Figure 96: Measured and simulated reflection coefficient at port 3 of the paper tag; port 1 is loaded by the antenna.

The RF-to-DC conversion efficiency is finally calculated as the ratio between the output DC power and the input available RF power: the comparison between simulated and measured efficiency is provided in Fig. 97, for the input power range obtained with the available laboratory equipments. Besides a slight degradation of the measured behavior, possibly due to the prototype inaccuracies, a fairly good agreement can be noticed in this case as well.

5.2.2 IC Prototyping

The designed ASIC prototype has been fabricated exploiting the mini-ASIC program and the UMC 180nm technology. The occupied area of the entire prototype is 1.5 mm x 3 mm. The complete prototype is shown in figure 98.

The RF subsystem, implemented to perform the EH, the UHF demodulation and UWB backscatter modulation, and which are described and characterized in Section 3, are shown in figure 99.

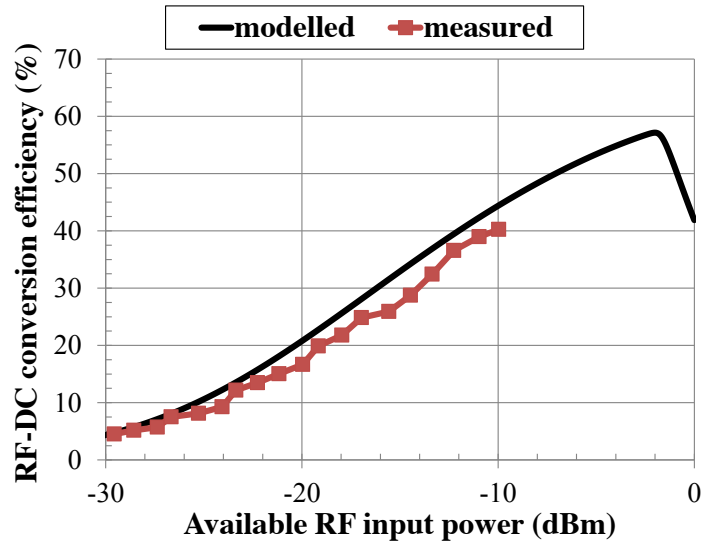


Figure 97: Comparison between the measured and simulated RF-to-DC conversion efficiencies.

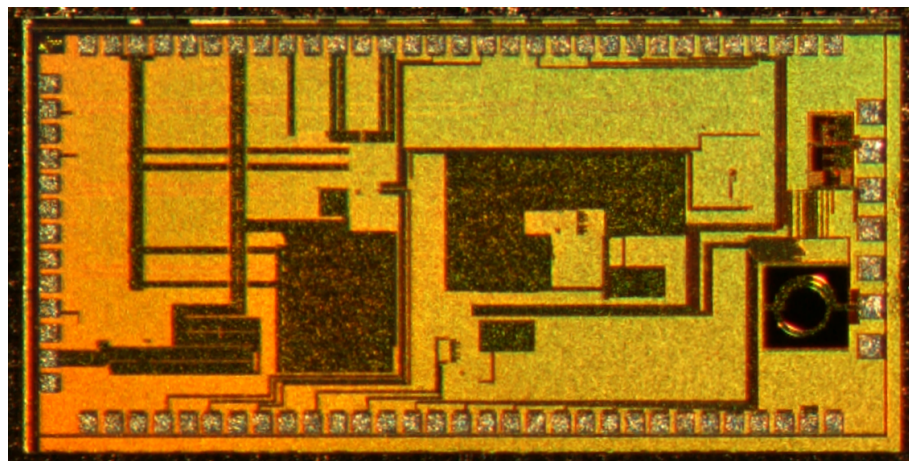


Figure 98: Picture of the tag fabricated with the UMC technology.

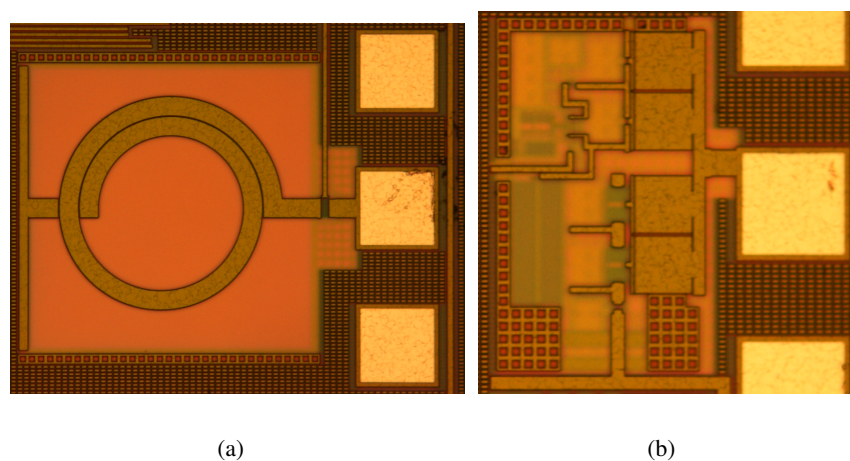


Figure 99: Picture of the fabricated IC. a) UWB backscatter modulator; b) UHF front-end.

5.3 UWB Backscattering Models

5.3.1 Signaling Scheme

Several signal processing tasks have to be accomplished by the readers in order to provide information about the tags to the network. The first task consists of tag detection, that is the process to determine the presence of a tag in a monitored area. Secondly, the reader has to perform tag TOA estimation, thus enabling localization capabilities by fusing at the central unit at least three tag observations. Due to the low complexity of the tag and to the fact that tags cannot directly communicate, no cooperative techniques can be exploited for performance improvement and coverage extension, so every point of the monitored area must be directly covered by a sufficient number of readers. Finally, if the tag itself contains data to be transmitted to the reader (e.g., because it has an embedded sensor, or data related to the object to which it is attached), the receiver has to perform signal demodulation. In the following, Fig. 100 will be considered the reference scenario, composed of a square cell with 4 readers with co-located transmitters and receivers placed at the corners.

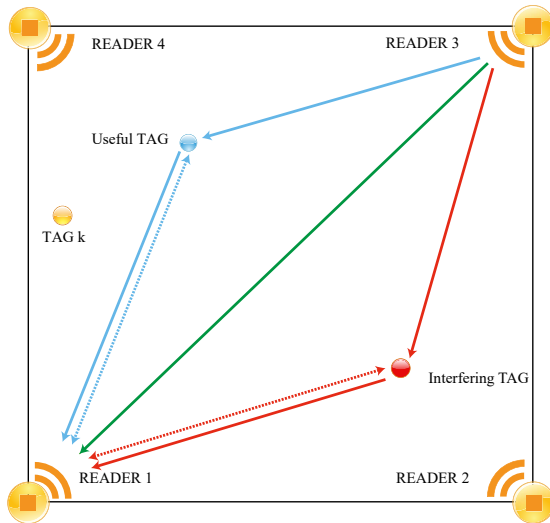


Figure 100: Reference scenario composed of a square cell monitored by four readers placed at the corners.

To meet the processing requirements previously listed, consider the scenario of Fig. 100, where each reader interrogates N_{tag} tags located in the same area. In Fig. 101 the architectures for tag and reader, as separated transmitter and receiver, are shown. During the interrogation phase, the j th transmitter sends

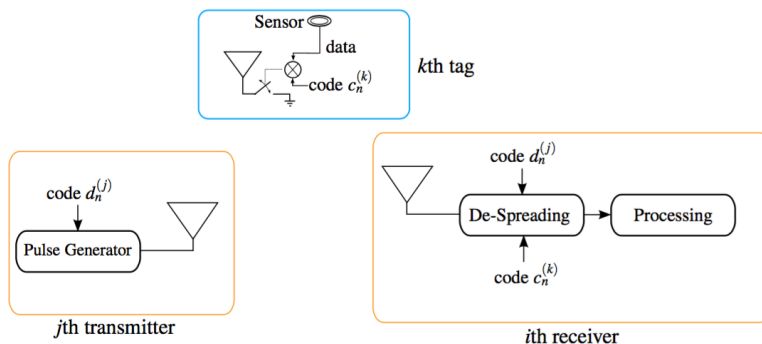


Figure 101: The considered scheme of the tag, transmitter and receiver.

an UWB interrogation signal composed of repeated symbols of duration T_s , each given by

$$\begin{aligned} s_{Tj}(t) &= \sum_{m=0}^{N_p-1} \sum_{n=0}^{N_c-1} d_n^{(j)} g(t - nT_c - mT_s) \\ &= \sum_{m=0}^{N_p-1} \sum_{n=0}^{N_c-1} d_n^{(j)} \sum_{i=0}^{N_{pc}-1} p(t - nT_c - iT_p - mT_s) \end{aligned} \quad (22)$$

where $\{d_n^{(j)}\}$ is the j th transmitter's code, N_c , N_p , N_{pc} are the number of chips (code length), transmitted symbols, and pulses per chip, respectively, T_c and T_s are the chip and symbol time, respectively, and $p(t)$ is the transmitted UWB pulse, repeated with PRP T_p .

Each tag switches its backscatter modulator status at each chip time T_c , according to an antipodal binary code $\{c_n^{(k)}\}$, for $n = 0, 1, \dots, N_c - 1$, allowing the creation of a unique backscattered channel for each tag. An example of UWB backscattered signal corresponding to two different antenna load configurations (open/short) is shown in Fig. 102, when a single UWB pulse is emitted by the reader. As can be noticed, there is a polarity change in the reflected antenna mode component, which is the only part depending on the antenna load, and that can be exploited for tag identification and localization with the signal processing herein described.⁹ Considering N_p transmitted symbols, the backscatter modulator signal commanding the switch of the k th tag is

$$m^{(k)}(t) = \sum_{m=0}^{N_p-1} b_m \sum_{n=0}^{N_c-1} c_n^{(k)} \cdot \Pi\left(\frac{1}{T_c}[t - mT_s - nT_c]\right) \quad (23)$$

with $\Pi(t)$ denoting the rectangular function of unitary duration for $t \in [0, 1]$. In this way, the polarity of the backscattered signal changes at each chip time T_c according to the k th tag's code value $c_n^{(k)}$, with $k \in \mathcal{T}$, while the polarity of the whole symbol composed of N_s pulses is modulated according to the data bit $b_m \in \pm 1$ transmitted from the tag to the reader [27].

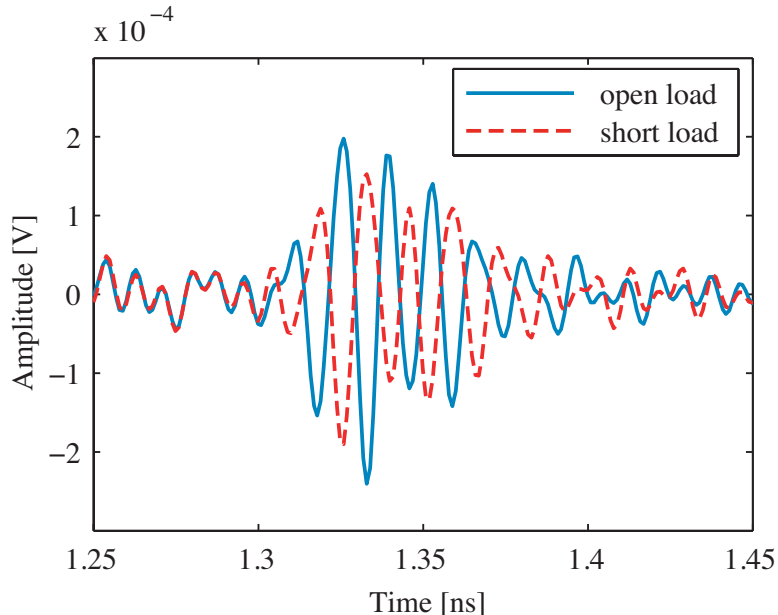


Figure 102: Example of the backscattered signal for tag open and short circuit load (only the antenna mode component is shown).

⁹We refer the reader to [31–33] for a detailed electromagnetic analysis of UWB backscattering and antennas.

Each interrogation signal is backscattered by the tags as well as by the surrounding scatterers of the environment. Specifically, the signal at the i th receiver due to the signal transmitted by the j th transmitter, can be written as

$$\check{r}_{i,j}(t) = r_{i,j}^T(t) + r_{i,j}^S(t) + n(t) \quad (24)$$

where $r_{i,j}^T(t)$ denotes the tags contribution¹⁰ while $r_{i,j}^S(t)$ accounts for the static contribution (comprehensive of multipath) between transmitter and receiver.¹¹ Finally, $n(t)$ models the AWGN with one-sided power spectral density N_0 .

The tags' contribution is given by¹²

$$r_{i,j}^T(t) = \sum_{k \in \mathcal{T}} \left[\left(s_{Tj}(t) \otimes h_{\text{down}}^{(j,k)}(t) \right) \cdot m^{(k)}(t) \right] \otimes h_{\text{up}}^{(k,i)}(t) \quad (25)$$

where $h_{\text{down}}^{(j,k)}(t)$ is the downlink channel impulse response (CIR), de-embedded of the propagation time, related to the link j th transmitter - k th tag, $h_{\text{up}}^{(k,i)}(t)$ is the uplink CIR related to the link k th tag - i th receiver.

It is possible to rearrange (25) as

$$r_{i,j}^T(t) = \sum_{k \in \mathcal{T}} \sum_{m=0}^{N_p-1} \sum_{n=0}^{N_c-1} d_n^{(j)} c_n^{(k)} b_m w_{i,j,k}^T(t - mT_s - nT_c - \tau_{i,j,k}) \quad (26)$$

where $\tau_{i,j,k}$ is the signal TOA, considered with respect to the transmitter's clock, and $w_{i,j,k}^T(t) = g(t) \otimes h_{\text{down}}^{(j,k)}(t) \otimes h_{\text{up}}^{(k,i)}(t)$ is the channel response to $g(t)$ for the k th tag. Specifically, it is $\tau_{i,j,k} = (d_{Tj} + d_{Ri})/c$, where d_{Tj} is the distance between the j th transmitter and the tag, d_{Ri} is the distance between the tag and the i th receiver,¹³ and c denotes the speed of light.

Note that the UWB round trip backscattering channel is strongly unfavorable from the energetic point of view, since the received backscattered signal experiences pathloss between the reader and the tag twice [36, 37]. In fact, the distance-dependence of the received signal power scales, in free space, with the fourth power of the reader-tag distance, resulting in a maximum reading distance much smaller than for an ordinary one-hop communication link [38]. It is important to underline that the tag backscattering behavior is strongly impacted by the presence of the object on which it is attached [39, 40].

Together with the tag response, the receivers collect the signal reflected by the surrounding environment, which composes the static contribution of the clutter component. Such a static contribution $r_{i,j}^S(t)$ in (24) is

$$r_{i,j}^S(t) = s_{Tj}(t) \otimes h_c^{(j,i)}(t) \quad (27)$$

having indicated with $h_c^{(j,i)}(t)$ the CIR of the link between the j th transmitter and the i th receiver, which is independent of tags' backscattering. As before, (27) can be reformulated as

$$r_{i,j}^S(t) = \sum_{m=0}^{N_p-1} \sum_{n=0}^{N_c-1} d_n^{(j)} w_{i,j}^S(t - mT_s - nT_c - \tau_{i,j}) \quad (28)$$

where $\tau_{i,j}$ is the signal TOA, considered with respect to the transmitter's clock, and $w_{i,j}^S(t) = g(t) \otimes h_c^{(j,i)}(t)$ is the channel response to $g(t)$ for the static contribution. Specifically it is $\tau_{i,j} = d_{i,j}/c$, where $d_{i,j}$ is the distance between the j th transmitter and the i th receiver.

¹⁰Here only the tag's antenna mode component is included [34].

¹¹We neglect the presence of fast moving objects and tags in the environment, as well as the effects of diffuse clutter [30, 35].

¹²Operator \otimes denotes the convolution.

¹³Both d_{Tj} and d_{Ri} are function of the tag index k , however this dependence has been omitted for notation convenience.

Table 6: Minimum number of pulses for a target reader-tag reading range and refresh rate with a 128 bit packet transmission.

Reader-Tag distance	1 m	2 m	3 m	4 m	5 m	6 m	7 m	8 m	9 m	10 m
N_s	5	71	358	1129	2757	5716	10589	18064	28934	44100
Refresh Rate	12207 Hz	860 Hz	170 Hz	54 Hz	22 Hz	11 Hz	6 Hz	3 Hz	2 Hz	1 Hz

Discrimination between the useful contribution backscattered from the k th tag and those reflected by other tags and the direct transmitter-to-receiver signal is ensured by a de-spreading procedure at the receiver (see Fig. 101). Specifically, the separation is possible by the adoption of different spreading codes, since the tags signals are modulated according to the composed code $\{d_n^{(j)} \cdot c_n^{(k)}\}$, while the static contribution independent of tags' backscattering results modulated according to the transmitter code $\{d_n^{(j)}\}$ only [30]. In the following, starting from the signaling scheme here described, the management of the tags in the scenario is described.

5.4 Signal Processing for Communication and Sensing

When multiple UWB tags based on backscatter modulation are deployed in the environment, several aspects have to be accounted. Here the solutions developed for tags management are reported in a unitary form, in order to drive the following discussion about the receiver design and the network deployment of the following sections.

5.4.1 Tags Synchronization

Tags' synchronization is a crucial operation in the UWB-RFID systems. In fact, if tags code generators are completely free running, the reader must perform an exhaustive code acquisition search in order to synchronize its code generator, used for the de-spreading, with that of the intended useful tag which has to be detected. In addition, the level of reader-tag synchronization imposes constraints on the tags' codes assignment to counteract multi-user interference, as detailed in Sec. 5.4.3. To accomplish this task, an additional narrowband link, for example in the UHF band or in the 2.4 GHz band, can be used to derive the synchronization signal necessary to wake-up tags, initially in an idle state, and to reset the tags' spreading code generators. The same wake-up signal can also be used to energize the tag by exploiting

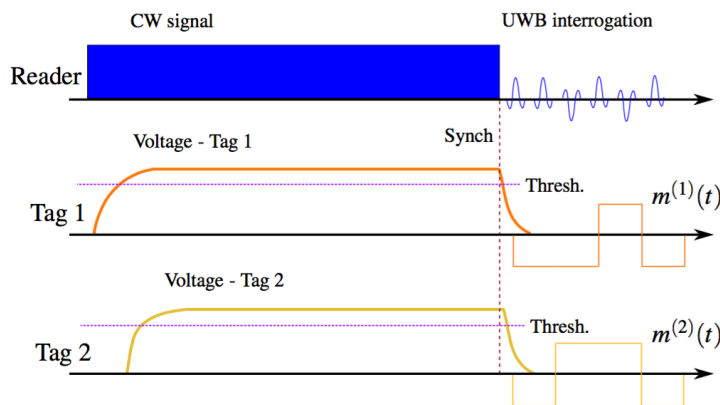


Figure 103: Wake-up synchronization scheme and signaling.

energy harvesting techniques, thus making the tag fully passive, that is, energy autonomous.

Among the various possibilities, an interesting solution is to perform the reset of the tag code generator on the falling edge of a wake-up CW carrier received by tags, as shown in Fig. 103. Note that the CW powers up tags, by charging a capacitor via the antenna and a rectifier circuit. Once the CW signal has ended, the falling of the resulting voltage is used for initiating the backscatter modulation of the UWB signals. In this way the propagation-dependent capacitor charge time¹⁴ does not play a significant role in the synchronization jitter, since the discharge starting event is not affected by the pathloss and depends only on the tags' circuitry. Such solutions have been proposed and experimented in [6,41]. The maximum offset after this procedure is expected to be in the order of a chip time. Moreover, if the narrowband link exploited for wake-up is modulated with a proper signal (e.g., exploiting ASK/OOK modulations), the demodulated signal at tag side can serve as reference to lock the local tag oscillator, and helps to prevent the clock drift effect [42]. Such a clock drift is present at tag side due to the poor characteristics of the low-cost oscillators driving the backscatter modulator. The clock drift determines then a variation on the modulation at tag side with respect to that expected at reader side. The longer is the duration of the UWB packet, that is, $N_p T_s$, the more the drift effect is detrimental. An example of ad-hoc oscillator for tags based on UWB backscattering has been presented in [43].

5.4.2 Tag Detection

Once tags are synchronized, the UWB reader-tag communication begins, since tags start modulating the transmitted pulses that are then received by the readers (see Fig. 103).

As described in Sec. 5.3.1, tags multiple access is realized thanks to the assignment of different spreading codes to tags. In this case, since we are in presence of a CDMA and each spreading code is uniquely assigned to a tag, a decision at the output of the de-spreading phase is sufficient to accomplish the identification purpose. De-spreading is operated, as described in [27], by accumulating the responses of the N_s pulses that compose a symbol. In particular, each response of the channel to a transmitted pulse is multiplied at receiver side for the code element $\tilde{d}_n^{(j)}$ of the intended transmitter and the code element $\tilde{c}_n^{(k)}$ of the intended tag, and then summed up to the others composing a symbol. Codes $\{\tilde{d}_n^{(j)}\}$ and $\{\tilde{c}_n^{(k)}\}$ denote the periodically repeated sequences of period $N_s = N_c N_{pc}$ as $\tilde{c}_n^{(k)} \triangleq c_{\lfloor n/N_{pc} \rfloor}^{(k)}$ and $\tilde{d}_n \triangleq d_{\lfloor n/N_{pc} \rfloor}^{(j)}$ for $n = 0, 1, \dots, N_s - 1$, with $\tilde{c}_{n+N_s}^{(k)} = \tilde{c}_n^{(k)}$, $\tilde{d}_{n+N_s}^{(j)} = \tilde{d}_n^{(j)}$, where $\lfloor \cdot \rfloor$ indicates the floor operation. Such an operation allows isolating the signals related to a specific transmitter-tag pair from clutter and interference, and produces a processing gain counteracting the receiver noise [27].

The optimal processing technique requires a matched filter [27] but its implementation is often too complex due to the large bandwidth so energy-based detection techniques are usually considered [2]. Generically, tag detection is realized at each reader by checking if the de-spreading output level related to a specific tag code is above a certain threshold. When more than one reader is tuned to the same tag, the decision on the tag presence can be taken by properly combining the different observations in the central unit. The detection and demodulation of multiple tags requires the replication of the same receiver structure multiple times, with multiple de-spreaders each tuned to a specific tag code. Alternatively, the same de-spreader can be re-used for different tags in different interrogation cycles, changing properly the tag code, at the expense of the system refresh rate, that is the capability of the system of offering a new reading of a specific tag.

It is important to underline that even if tag detection has been properly performed, the receiver has to continue tracking a certain tag code to follow the tag clock drift. Note that in UWB backscattering, the clock drift at tag side does not affect the TOA of the backscattered pulse (which is determined only by the transmitter, supposed to be equipped with a high-accuracy clock), but it affects the pulses' modulation operated by spreading codes. In addition to detection, demodulation of the bits $\{b_m\}$ allows data communication between tags and readers. In this manner the tag ID can be transferred to the network or, if the tag has embedded sensors, measurements can be transmitted. Data modulation can be accomplished via

¹⁴This is due to the narrowband CW signals that may experience selectively channels, and to different reader-tag distances.

Table 7: Simulation parameters.

Parameter	Symbol	Value
EIRP	P_T	-11 dBm
Bandwidth	W	1.5 GHz
Center frequency	f_c	4 GHz
Pulse interval	T_p	128 ns
Reader antenna gain	G_r	5 dBi
Tag antenna gain	G_t	1 dBi
Tag losses	L_t	2 dB
Pulses per symbol	N_s	32768
Receiver noise figure	F	4 dB
Signal-to-Noise Ratio	SNR	15 dB

binary phase shift keying (BPSK) modulation of the overall sequence of N_s pulses composing a symbol, as described in [27].

In order to have an idea of potential operating ranges, Table 6 shows the number of pulses N_s required to ensure a theoretical reader-tag distance, in monostatic configuration, when an energy detector receiver is considered, for a SNR which let to guarantee a probability of false alarm 10^{-3} and a probability of detection 0.9, under the European mask constraint [2]. In the same table the maximum refresh rate when a packet of 128 bits is transmitted from the tag to the reader is also shown.¹⁵ Here and in the following of the paper, results have been obtained considering the realistic system parameters reported in Table 7. It is important to underline that the larger is N_s (i.e., the symbol time), the longer will be the maximum allowed reader-tag distance, thanks to an increasing processing gain at receiver side. As reported in Sec. 5.3.1, the number of pulses per symbol N_s is determined by both the code length N_c and by the number of pulses per chip N_{pc} . In general, increasing the number of pulses per chip, with a fixed PRP, decreases the energy consumption since the tag average switching rate between open and short circuit is decremented. Furthermore, as described in [2], this helps on avoiding detrimental effects due to synchronization mismatches between tags and receivers.

5.4.3 Multi-Tag Interference

With the proposed CDMA scheme, all tags present in the monitored area simultaneously respond to the reader interrogation, without the need of any anti-collision protocol as required in the EPC Gen.2 RFID standard [44]. Such an access technique poses particular constraints in terms of code assignment to tags. The behavior of the adopted codes, and the degree of synchronization between readers and tags, determine the amount of interference at the receiver. Such interference may produce false alarms during the detection of a desired tag [42] and worsen the demodulation performance [27]. Moreover, due to the two-hop propagation link characteristic of backscatter propagation, near-far interference can drastically affect the performance; in fact, a tag close to a reader can produce an irreducible interference on the detector output of a farer tag, preventing the possibility of a correct detection. An extensive analysis of the code assignment strategies to tags and an overview of their design guidelines is reported in [2]. We want here to stress the importance of adopting balanced, or quasi-balanced, codes (i.e., codes with zero mean value) that allow the clutter cancellation at receiver side [27], as will be discussed in the next section.

A main limitation of the analyzed CDMA scheme is represented by the necessity of providing each tag with a unique spreading code. Table 8 reports the number of different available sequences for several

¹⁵The number of bits has been chosen larger than the standard 96 bits of the Electronic Product Code (EPC) provided by the Gen.2 UHF-RFID to account for possible sensor data and parity.

Table 8: Number of available codewords for different code families.

N_c	15/16	31/32	63/64	127/128	255/256	511/512	1024/1024	2047/2048	4095/4096	8191/8192
Orthogonal (balanced)	15	31	63	127	255	511	1023	2047	4095	8191
M-sequences	2	6	6	18	16	48	60	176	144	630
Gold (balanced)	-	17	33	65	-	257	513	1025	-	4097

code families of interest for the UWB-RFID system, considering typical codes lengths. As example, a code length allowing several trade-offs between interference mitigation, complexity and detection performance is $N_c = 128$, as shown in [2]. In this case, adopting balanced Gold codes, which represent good candidates, only 65 different tags can be managed. Note that, in case of good reader-tags synchronization, the same spreading code can be assigned to several tags with a different initial phase shift, providing that this is greater than the possible level of asynchronism of the system. In this manner the number of manageable tags is increased. New alternative solutions capable of overcoming the limitation on the number of different tags were introduced in GRETA (modes 2 and 3 presented in Sec. ??) and will be further detailed in Sec. 5.7.4.

5.4.4 Clutter Removal

The RFID-UWB system suffers from clutter, that is determined by the environmental response not depending on tag's backscattering [34]. In monostatic networks the clutter includes the transmitting-receiving antenna coupling, which can be avoided with time-gating operations on the received signal [45], resulting in *blind zones* around the reader where the tag cannot be detected. Another clutter contribution is given by the tag's signal structural mode, which is the backscattered component independent on the tag's antenna load. In this case, it has been proposed to separate in the time-domain the structural and the antenna mode by adopting a delay line at tag side between the antenna port and the backscattering modulator [32, 45]. The last clutter contribution is given by the response of the environment. The ensemble of all these signals determines the static contribution $r_{i,j}^S(t)$ at receiver side.

The clutter component must be properly canceled in order to provide robust tags signal detection. The proposed CDMA approach is intrinsically immune to clutter if balanced codes are adopted at tag side, regardless the reader's code [27, 30]. In fact, with the de-spreading, each static response to a transmitted pulse is multiplied for the tag code $c_n^{(k)}$ and accumulated; the balanced tag code makes then null the clutter output contribution after the accumulation of the N_s pulses. Alternative solutions for clutter suppression deal with classical radar signal processing, such as filtering techniques that remove the estimated background response when the tag is absent [45]. The main drawbacks are represented by the necessity of channel estimation and very high-speed signal processing, additionally with severe limitations in terms of tags movement.

From the implementation point of view, one of the main challenges is the digital removal of the clutter component, whose level is usually several orders of magnitude higher than that of tags, as will be studied in Sec. 5.5.1, thus determining the dynamic range at the receiver.

5.5 Receiver Design

In the previous sections, a survey of the main challenges related to the design of the passive UWB-RFID system was presented. Now, starting from the issues and constraints underlined, the main guidelines for the receiver design will be derived, based also on so-far unexplored readers' configurations for RFID applications. Note that such a design must be carefully carried out due to the specificity of the considered system where different signal components are present at the reader input. In fact, as will be investigated, the signals of interest coming from tags are dominated by the various static contributions (i.e., the clutter),

and the receiver must properly handle such weak signals preventing in parallel ADC saturations due to the strongest components.

5.5.1 Receiver Dynamic Range

In the practical implementation of the UWB receiver it is important to account for the relative levels of the received signals, both useful and interfering, in order to reduce the possibility of ADC saturation and poor quantization. For this reason, the signal characteristics expected at the receiving antenna port are now analyzed. Specifically, the received signal is composed of the following components:

1. The signals backscattered by the tags, related to the interrogation of a specific transmitter, which the reader wants to demodulate;
2. The signals backscattered by the tags related to the interrogation signal coming from other transmitters (i.e., an interference component);
3. The interference of other transmitters, that is, the ensemble of signals emitted by other transmitters independent of tags' and environment backscattering;
4. The signal emitted by a co-located transmitter and reflected by the environment, independent of tags' backscattering.

The first two components are the tags' contribution $r_{i,j}^T(t)$; the last two components are the static contribution (i.e., clutter) $r_{i,j}^S(t)$ (see Sec. 5.3.1). For the sake of a complete characterization of the dynamic range, it is important to analyze the expected amplitude of these signals, as well as the ratio between the strongest input signal and the signal backscattered by the intended tag (useful tag), which is supposed to be strongly attenuated by the two-way channel.

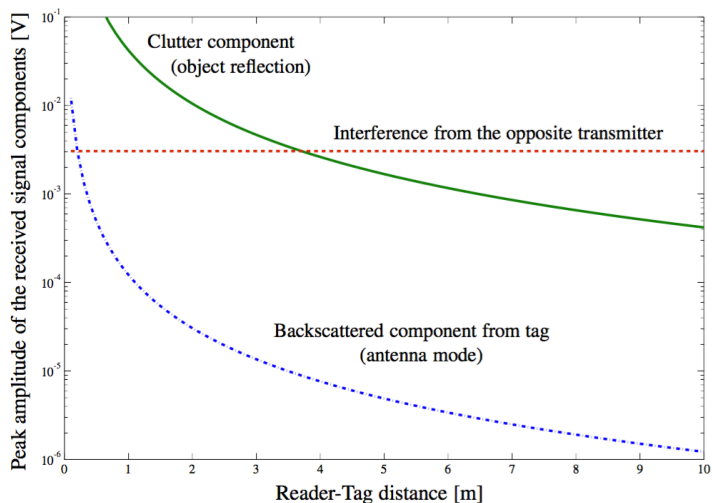


Figure 104: Typical dynamic range of a UWB-RFID system.

Assuming for simplicity a monostatic configuration, the pathloss related to the different components of the received signals, obtained adopting the free-space propagation model at a single central frequency, can be written as

$$\text{PL}_{i,k}^{(1,2)} = \left[G_r^2 G_t^2 \left(\frac{\lambda}{4\pi |\mathbf{p}_{Ri} - \mathbf{p}_k|} \right)^4 \right]^{-1} \quad (29)$$

$$\text{PL}_{i,j}^{(3)} = \left[G_r^2 \left(\frac{\lambda}{4\pi |\mathbf{p}_{Tj} - \mathbf{p}_{Ri}|} \right)^2 \right]^{-1} \quad (30)$$

$$\text{PL}_{i,k}^{(4)} = \left[\sigma G_r^2 \frac{\lambda^2}{(4\pi)^3} \left(\frac{1}{|\mathbf{p}_{Ri} - \mathbf{p}_k|} \right)^4 \right]^{-1} \quad (31)$$

where G_r and G_t are the reader and tag antenna gain, respectively, λ is the wavelength.¹⁶ The first term $\text{PL}_{i,k}^{(1,2)}$ accounts for the useful reader-tag-reader backscattering information signal, or equivalently for the interfering component of a different tag. The term $\text{PL}_{i,j}^{(3)}$ accounts for the direct path coming from an interfering transmitter, while $\text{PL}_{i,k}^{(4)}$ for a clutter component, here approximated with the reflection from a scatter with a radar cross section (RCS) σ placed in the tag's position. In fact, each tag is usually attached to a bigger object whose reflection properties, characterized by its RCS, could determine the presence of a strong clutter component having a TOA comparable to that of the useful signal.

In Fig. 104, the peaks of the received signals are reported considering the reference scenario of Fig. 100, where 4 readers are placed at the corner of a $(7 \times 7) \text{ m}^2$ area. As scatter, it is considered an object, attached to the tag, with the RCS of a square metallic plate of dimensions $(50 \times 50) \text{ cm}^2$. The figure illustrates that the maximum received signal component is usually the one coming from the opposite transmitter. For this reason, a strong interference mitigation capability is requested for the de-spreading operation. In non-synchronous scenarios such a mitigation capability is hard to guarantee [2] and time division multiple access (TDMA) techniques between different transmitters have to be adopted to avoid interference, as discussed in Sec. 5.7.1.

5.5.2 Analog-to-Digital Conversion

As previously stated, the receiver has to perform the signal de-spreading to detect and demodulate the tag signal. This process is generally performed in digital and, consequently, the ADC dynamic must be set to prevent saturation from the strongest signals, that are interference and clutter. In general, the receiver low-noise amplifier (LNA) must be designed to prevent saturation from the direct signals coming from other transmitters. It is important to underline that, as it will be described in Sec. 5.7.2, in some cases the direct transmitter-to-receiver signals can be exploited for synchronization and integration of radar capabilities; in such cases, even if TDMA is adopted to handle the access of different transmitters to prevent interference, a proper gain control has to be implemented to adapt the ADC dynamic to the input signals of different amplitude.

The number of quantization levels is then designed, as usual, for ensuring a satisfactory signal-to-quantization-noise ratio (SQNR) for the maximum allowed reader-tag distance (worst case). Note that the number of quantization bits is in general higher than in the case of traditional one-way active communication links due to the two-hop channel and its poor link budget. In general, a multistatic configuration requires less bits for the ADC conversion, since the received tag signal experiences a lower dynamic for different receiver-tag distances.

Fig. 105 presents the SQNR obtained at the output of the ADC whose maximum dynamic is adjusted considering the signal from the opposite transmitter in the reference square cell, as function of the reader-tag distance and for different number of quantization bits m , with $m = \log_2(L)$ and L the number of quantization levels. It is immediate to observe how a high number of bits is necessary in order to provide a satisfactory SQNR so that the quantization noise is negligible with respect to the thermal noise (e.g., 15 bits for a SQNR of 20 dB at 9 m reader-tag distance). Fortunately, this requirement can be relaxed by considering the presence of the digital de-spreading process. In fact, in presence of low SNR conditions, as the case of the received UWB tag signal, the process gain is beneficial for increasing the effective SQNR, as $\text{SQNR}_{\text{out}} = N_s \text{SQNR}_{\text{in}}$, where SQNR_{in} and SQNR_{out} refer to the SQNR at the input and at the output of the de-spreader, respectively. In this manner, the target SQNR at the output of the ADC, can be reduced, as well as the number of quantization bits. As an example, for a tag distance of 9 m with

¹⁶For UWB signals all the terms should be characterized as function of the frequency. This is a central-frequency approximation useful for understanding the order of magnitude of the signal level at receiver side.

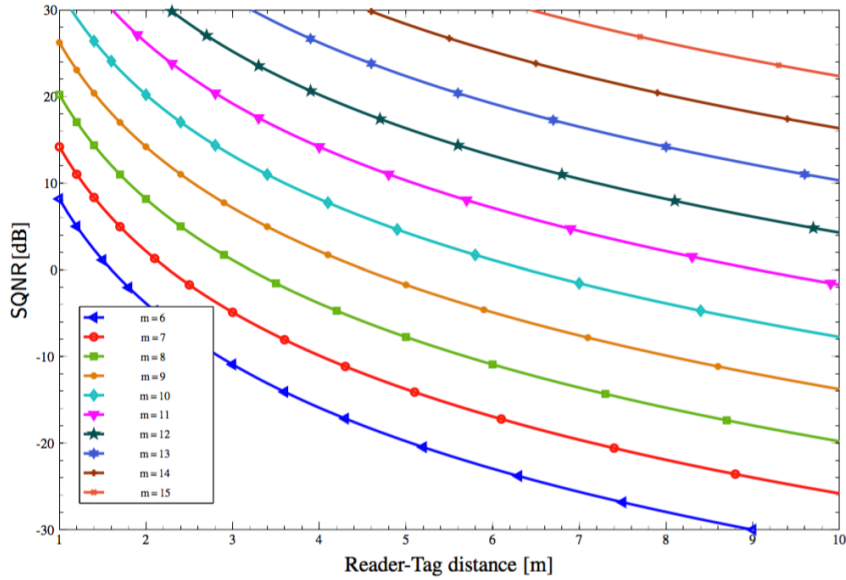


Figure 105: SQNR at the ADC output.

$N_s = 32768$, a $SQNR_{out}$ of 20 dB can be obtained with $SQNR_{in} = -25$ dB, reflecting in the adoption of 7 bits instead of 15.

An example of a receiver based on the scheme reported in [46], which prevents sampling at Nyquist rate, adopting 12 bits ADCs for the UWB-RFID reader is described in [47].

5.6 Signal Processing for Localization and Tracking

Accurate localization via RFID is challenging in wireless environments with multipath, clutter, and signal obstructions (for example caused by furniture and walls in indoor scenarios). These conditions can cause observations (e.g., range measurements) that are non-representative of the target object with heavy impact on the localization accuracy. These conditions can be mitigated by selecting representative observations and exploiting prior knowledge [48–54]. Here we focus on the main achievement obtained within the project in terms of selecting representative observations and use prior knowledge to derive a range information model [55] (see also Deliverable D3).

5.6.1 Blind Selection of Representative Observations

We proposed an approach that consists in exploiting diversity and selection of measurements to enhance the performance of sensor radars in harsh propagation environments with non-line-of-sight (NLOS) conditions [56]. Innovative techniques are presented, which are blind to both channel knowledge and propagation environment for selecting representative observations. Such blind techniques rely on indicators obtained from non-coherent reception and sub-Nyquist sampling of waveforms. The key contributions can be summarized as follows:

- introduction of blind techniques for the selection of representative observations;
- quantification of the localization accuracy improvement provided by observation selection techniques.

From the set of received signals for each tag-reader pair $\mathbf{r}_{P_{all}}(t) = \{r_{ij}(t) : (i, j) \in P_{all}\}$ after pre-filtering and clutter removal, a feature $h(r_{ij})$ is extracted for each received signal r_{ij} . Then, a subset of cardinality $L \leq N_{obs}$ of vectors $\mathbf{r}_{P_{sel}}(t)$ is selected based on such a feature. The TOA estimator at each receiver determines $\hat{\tau}_{ij}$ for the signal $r_{ij}(t)$ if selected, i.e., $(i, j) \in P_{sel}$.

The choice of the feature is crucial for the sensor radar's ability to select observations that are representative for target location inference. Therefore, such a choice has to be based on the relation be-

tween the feature $h(r_{ij})$ and the range error $e_{ij} = c |\hat{\tau}_{ij}(\mathbf{x}) - \tau_{ij}(\mathbf{x})|$. Consider a decision vector $\bar{\varepsilon}_{ij} = [\bar{\varepsilon}_{ij}^{(0)}, \bar{\varepsilon}_{ij}^{(1)}, \dots, \bar{\varepsilon}_{ij}^{(N_b-1)}]$ of N_b signal indicator samples for the pair $(i, j) \in P_{\text{all}}$ (e.g., with an energy detector the $\bar{\varepsilon}_{ij}^{(q)}$ is related to the energy of samples within the q th time interval) then $h(r_{ij}) = h(\bar{\varepsilon}_{ij})$. Since the range error depends on the true TOA, the ideal selection would be based on the centrality of $\bar{\varepsilon}_{ij}^{(q)}$ distribution with respect to $\tau_{ij}(\mathbf{x})$. Unfortunately, the true TOA is not known in a blind context. Different features are now considered and are related to the amplitude and temporal distribution of the decision vector $\bar{\varepsilon}_{ij}$ for selecting the observations that are most likely representative of the target (i.e., less affected by multipath, noise, and obstruction-loss).

To evaluate the temporal dispersion of $\bar{\varepsilon}_{ij}$ over the observation time, first normalize its elements, within each decision vector, as

$$f_{ij}(q) = \frac{\bar{\varepsilon}_{ij}^{(q)}}{\sum_{q=1}^{N_b} \bar{\varepsilon}_{ij}^{(q)}} \quad (32)$$

where $f_{ij}(q)$ represents the sampling probability that the true TOA belongs to the q th time interval given the vector $\bar{\varepsilon}_{ij}$. Note that, in the absence of prior knowledge, we consider the true TOA included in the maximum element of $\bar{\varepsilon}_{ij}$ with highest probability. Define the cumulative distribution function, the first moment, and the n th central moment of $f_{ij}(q)$, respectively, as

$$F_{ij}(x) = \sum_{q \leq x} f_{ij}(q) \quad (33)$$

$$\bar{\mu}_{ij} = \sum_{q=1}^{N_b} q f_{ij}(q) \quad (34)$$

$$\mu_{ij}^{(n)} = \sum_{q=1}^{N_b} (q - \bar{\mu}_{ij})^n f_{ij}(q). \quad (35)$$

From (33), (34), and (35), the temporal dispersion of the signal indicator samples can be evaluated by considering variance σ_{ij}^2 , interquartile range IQR_{ij} , kurtosis κ_{ij} , and skewness χ_{ij} , which are respectively given by

$$\sigma_{ij}^2 = \mu_{ij}^{(2)} \quad (36)$$

$$\text{IQR}_{ij} = F_{ij}^{-1}(0.75) - F_{ij}^{-1}(0.25) \quad (37)$$

$$\kappa_{ij} = \frac{\mu_{ij}^{(4)}}{(\mu_{ij}^{(2)})^2} \quad (38)$$

$$\chi_{ij} = \frac{\mu_{ij}^{(3)}}{\left(\sqrt{\mu_{ij}^{(2)}}\right)^3}. \quad (39)$$

To evaluate the amplitude dispersion of $\bar{\varepsilon}_{ij}$, consider the maximum value M_{ij} , sample variance s_{ij}^2 , sample

range r_{ij} , and sample skewness c_{ij} , which are respectively given by

$$M_{ij} = \max_q \bar{\epsilon}_{ij}^{(q)} \quad (40)$$

$$s_{ij}^2 = \frac{1}{N_b} \sum_{q=1}^{N_b} \left[\bar{\epsilon}_{ij}^{(q)} - \left(\frac{1}{N_b} \sum_{q=1}^{N_b} \bar{\epsilon}_{ij}^{(q)} \right) \right]^2 \quad (41)$$

$$r_{ij} = \left| \max_q \bar{\epsilon}_{ij}^{(q)} - \min_q \bar{\epsilon}_{ij}^{(q)} \right| \quad (42)$$

$$c_{ij} = \frac{\sum_{q=1}^{N_b} \left[\bar{\epsilon}_{ij}^{(q)} - \frac{1}{N_b} \left(\sum_{q=1}^{N_b} \bar{\epsilon}_{ij}^{(q)} \right) \right]^3}{N_b \left(s_{ij}^2 \right)^{3/2}}. \quad (43)$$

The relation between a feature $h(\bar{\epsilon}_{ij}) \in \left\{ \sigma_{ij}^2, \text{IQR}_{ij}, \kappa_{ij}, \chi_{ij}, s_{ij}^2, M_{ij}, r_{ij}, c_{ij} \right\}$ and the range error e_{ij} has been evaluated through the correlation $\rho(h(\bar{\epsilon}_{ij}), e_{ij})$. Such correlation is determined via both the Spearman and the Pearson correlation coefficients, which indicates whether a monotone relation between the two variables exists [57]. Specifically, the Pearson correlation coefficient for N observations of two variables x and y is given by

$$\rho(x, y) = \frac{\sum_{i=1}^N (x_i - \bar{x})(y_i - \bar{y})}{\sqrt{\sum_{i=1}^N (x_i - \bar{x})^2 (y_i - \bar{y})^2}} \quad (44)$$

where x_i and y_i , with $i = 1, \dots, N$, are observations of x and y , respectively; and \bar{x} and \bar{y} are the average values of the observation sample $\{x_i\}_{i=1}^N$ and $\{y_i\}_{i=1}^N$, respectively.

Consider for example the cases $h(\bar{\epsilon}_{ij}) = \sigma_{ij}^2$, $h(\bar{\epsilon}_{ij}) = \chi_{ij}$, and $h(\bar{\epsilon}_{ij}) = c_{ij}$. Specifically, low or high values of the variance σ_{ij}^2 are obtained with narrow or wide sampling distribution of the time interval containing the true TOA, respectively. Therefore, lower values of σ_{ij}^2 are expected for large values of SNR corresponding to smaller range errors. Differently, positive or negative values of skewness χ_{ij} are obtained when the sampling distribution is right-side or left-side tailed, respectively. In particular, positive values are due to the shape of the channel impulse response, whose right-side tail is given by the delay spread of the channel. The channel impulse response guides the shape of $f_{ij}(q)$ for large SNR values, while it has a lower impact for small SNR values. Therefore, higher values of χ_{ij} are expected for smaller range errors. Finally, low or high values of sample skewness are obtained when there are many or few elements with large values within the decision vector $\bar{\epsilon}_{ij}$, respectively. Large-value indicator samples are more likely to be associated with the target for large SNR values, when the energy due to the target is easily discernible from the noise floor. Therefore, higher values of c_{ij} are expected for smaller range errors.

The observations $\hat{\tau}_{P_{\text{all}}}(\mathbf{x})$ are sorted based on the features $h(\bar{\epsilon}_{P_{\text{all}}})$ in increasing or decreasing order, depending on whether the relation between $h(\bar{\epsilon}_{ij})$ and e_{ij} is monotonically non-increasing or non-decreasing, respectively. The features $h(\bar{\epsilon}_{P_{\text{all}}})$ are calculated based on the vector $\bar{\epsilon}_{P_{\text{all}}}$, that contains all the decision vectors $\bar{\epsilon}_{ij}$ with $(i, j) \in P_{\text{all}}$. Then, the subset $\hat{\tau}_{P_{\text{selsel}}}(\mathbf{x})$ of $L = |P_{\text{sel}}| \leq N_{\text{obs}}$ selected observations is composed by the first L sorted observations and further processed by the localization algorithm.

The comparison between the computational complexity of localization with and without observation selection depends on the complexity of the localization algorithm $\mathcal{C}_l(N)$. Note that the term $\mathcal{C}_f(N_{\text{meas}})$ is a linear function with the number of observations $\mathcal{O}(N_{\text{meas}})$ for all the aforementioned features, except for the IQR_{ij} that requires function inversion. Therefore, the selection of representative observations enables significant savings in complexity when $m \geq 2$.

In case of energy detection as in GRETA, after perfect clutter removal, the multipath propagation accounts for the paths scattered by the target, and these paths arrive at the receiver after reflections. In

the absence of prior information, we consider the true $\tau_{ij}(\mathbf{x})$ uniformly distributed in the interval $[0, T_a]$, where the maximum possible delay T_a depends on the propagation environment. The pulse repetition frequency (PRF) is chosen to satisfy $T_g > T_a$.

A decision vector based on energy bins is obtained as $\bar{\mathbf{e}}_{ij} = [\bar{e}_{ij}^{(0)}, \bar{e}_{ij}^{(1)}, \dots, \bar{e}_{ij}^{(N_b-1)}]$, where the q th element $\bar{e}_{ij}^{(q)}$ is determined, for example, by averaging over the N_p received signals [58]. In particular, an hard-decision threshold crossing search (TCS) algorithm is considered. For the radar $(i, j) \in P_{\text{all}}$ and target at \mathbf{x} , the estimated TOA $\hat{\tau}_{ij}(\mathbf{x})$ is chosen as the central value of the corresponding dwell interval for the first element of the energy vector above the threshold ξ_{ij} . The amplitude and temporal distributions of the elements $\bar{e}_{ij}^{(q)}$ depend on the true TOA $\tau_{ij}(\mathbf{x})$ and the received SNR $\gamma_{ij}(\mathbf{x})$, which are affected by propagation conditions (i.e., noise, path-loss, obstruction-loss).

Figure 106 shows the localization error outage (LEO) at $e_{\text{th}} = 1$ m as a function of the number of selected observations L for $h(\bar{\mathbf{e}}_{ij}) = \sigma_{ij}^2, \kappa_{ij}$, and M_{ij} . To better understand the importance of the observation selection features on localization accuracy, the results are also obtained by considering a random selection of the L observations. The non-blind case $h(\bar{\mathbf{e}}_{ij}) = e_{ij}$ serves as a benchmark. In the absence of walls (LOS conditions), all selection features provide a LEO that decreases with the number of selected observations. This is expected from the absence of obstruction-loss and excess delay. However, note that $L = 5$ observations, even randomly chosen, are sufficient to have a localization error $e_p(\mathbf{x}) < 1$ m in 80% of cases despite only $L = 5$ TOA estimates out of 66 are processed. This significantly reduces localization complexity, which is a quadratic function of the number of estimates that are processed. The worse performance levels for $L < 5$ are mainly due to ambiguities (e.g., ghost targets [59]) given by the intersection of L isorange contours (ellipses in two dimensions) leading to more than a single point in the absence of prior information (e.g., information on the environment). In the presence of walls (NLOS conditions) the LEO presents a minimum for all the selection features with $L = 5$ or 6. Here, the effect of selection is clear since in the case with $L = 5$ the localization error is $e_p(\mathbf{x}) < 1$ m in 20% of cases for random observation choice and in 77%, 80%, and 76% of cases for $h(\bar{\mathbf{e}}_{ij}) = \sigma_{ij}^2, \chi_{ij}$, and c_{ij} , respectively. Note also that the localization error is $e_p(\mathbf{x}) < 1$ m in only 7% of cases when no selection is performed (i.e., all the $L = N_{\text{meas}} = 66$ observations are processed). Therefore, the performance improvement offered by the proposed method for this selection of representative observations is remarkable.

5.6.2 Range Information Model

New soft-decision ranging techniques based on energy detection have been proposed to improve the tradeoff between accuracy and complexity [60]. The proposed techniques rely on range likelihood functions extracted from a reduced dataset of observations. Such likelihood functions can be grouped into two types: theoretical range likelihood functions and empirical range likelihood functions. The former requires the knowledge of the channel statistics and is based on the tractable range information model derived in [61], whereas the latter requires a measurement phase in which empirical distributions are calculated. Such empirical distributions characterize the random variables (RVs) associated with a reduced dataset of observations. Compared to the traditional soft-decision ranging, the use of a reduced dataset decreases the amount of resource utilization for communicating likelihood functions among nodes. Such likelihood functions related to different nodes are jointly processed by a localization algorithm to estimate the unknown node positions. The key contributions can be summarized as follows:

- proposal of the idea of reduced dataset for soft-decision ranging techniques and localization algorithms;
- development of low-complexity soft-decision ranging techniques based on theoretical and empirical range likelihood functions.

We first revised a hard-decision ranging technique based on TCS and then propose two soft-decision ranging techniques with reduced dataset, namely the energy-based soft-decision (ESD) and the threshold-based soft-decision (TSD). Localization algorithms based on these ranging techniques are then presented. The classical hard-decision ranging algorithm TCS will serve as a benchmark for comparision. Let $\hat{i} =$

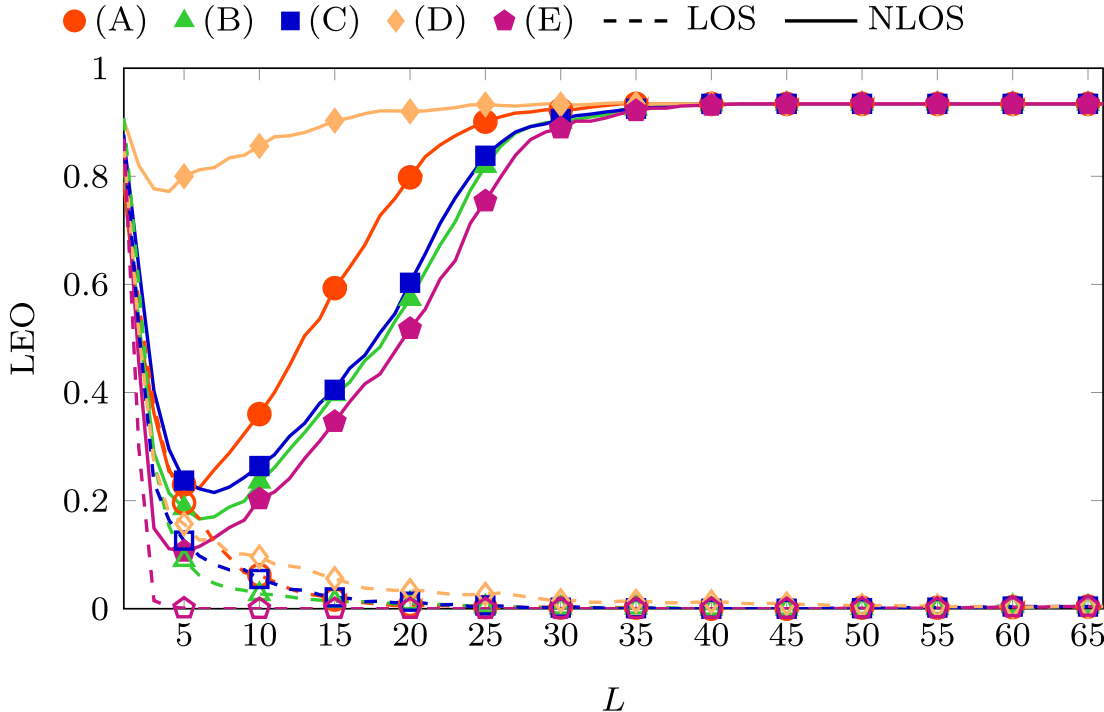


Figure 106: LEO as a function of e_{th} , with $L = 5$ and $N_{\text{meas}} = 66$, for the cases (A) $h(\bar{\varepsilon}_{ij}) = \sigma_{ij}^2$, (B) $h(\bar{\varepsilon}_{ij}) = \kappa_{ij}$, (C) $h(\bar{\varepsilon}_{ij}) = M_{ij}$. The case (D) represents the random choice of L observations. The case (E) refers to the non-blind cases, where $h(\bar{\varepsilon}_{ij}) = e_{ij}^2$.

$\min\{i : b_i > \xi_i\}$ denote the first bin crossing a threshold ξ_i . The TCS chooses the bin index \hat{i} and estimates the TOA $\hat{\tau}$ as a conventional value inside the interval $(T_d \hat{i}, T_d (\hat{i} + 1)]$ according to a function $\hat{\tau} = g(\hat{i})$ (e.g., the central value of the interval $\hat{\tau} = g(\hat{i}) = \hat{i}T_d + T_d/2$). The choice of the thresholds ξ_i 's affects the accuracy of the TOA estimation, as well as the detection rate and the false-alarm rate.¹⁷

Let $\boldsymbol{\theta} = [\tau \boldsymbol{\theta}_h \boldsymbol{\theta}_d]$ where $\boldsymbol{\theta}_h$ and $\boldsymbol{\theta}_d$ are the vectors of parameters representing the wireless channel and the energy detector (ED), respectively. We denote with $f_{B_i}(b_i|\boldsymbol{\theta})$ and $F_{B_i}(b_i|\boldsymbol{\theta})$ the probability density function (PDF) and cumulative distribution function (CDF) of the i th energy bin B_i conditional on $\boldsymbol{\theta}$. Analogously, $f_I(i|\boldsymbol{\theta})$ is the probability mass function (PMF) of the selected bin index conditional on $\boldsymbol{\theta}$. Soft-decision ranging for TOA estimation considers an observation set, usually the samples of the received waveforms, and compute the likelihood function of the TOA based on statistical models. We propose two range likelihood functions that are determined from a reduced dataset \mathcal{D} of variables obtained after processing $r(t)$. The ESD algorithm is a soft-decision algorithm that considers $\mathcal{D} = \{b_0, b_1, \dots, b_{N_b-1}\}$ as observation set, where b_i is an instantiation of the RV B_i . The RVs B_i 's are independent and non-identically distributed with noncentrality parameter depending on $\boldsymbol{\theta}$. The ESD range likelihood function is obtained as

$$\Lambda_{\text{ESD}}(\tau|\mathbf{b}) = \prod_{i \in \mathcal{B}} f_{B_i}(b_i|\tau, \boldsymbol{\theta}_h, \boldsymbol{\theta}_d) \quad (45)$$

where $f_{B_i}(b_i|\tau, \boldsymbol{\theta}_h, \boldsymbol{\theta}_d)$. The TSD is a soft-decision algorithm that considers $\mathcal{D} = \{\hat{i}\}$ as the observation set, where $\hat{i} \in \mathcal{B}$ is the selected bin index based on TCS. Specifically, let $\hat{i} = \min\{i : b_i > \xi_i\}$ denote the first bin crossing a threshold ξ_i , with \hat{i} being an outcome of the RV I [61]. The range likelihood function

¹⁷For TOA estimation, an approach based on model order selection which does not require a threshold is presented in [62]. For the cases where thresholding is used, typically the same threshold ξ_i is used for all the bins (i.e., $\xi_i = \xi \forall i \in \mathcal{B}$) and is chosen by accounting only for the randomness of the noise and discarding that of multipath propagation [63–66]. In contrast, the proposed range information model [61] enables us to choose a threshold that accounts for the randomness of the wireless environments.

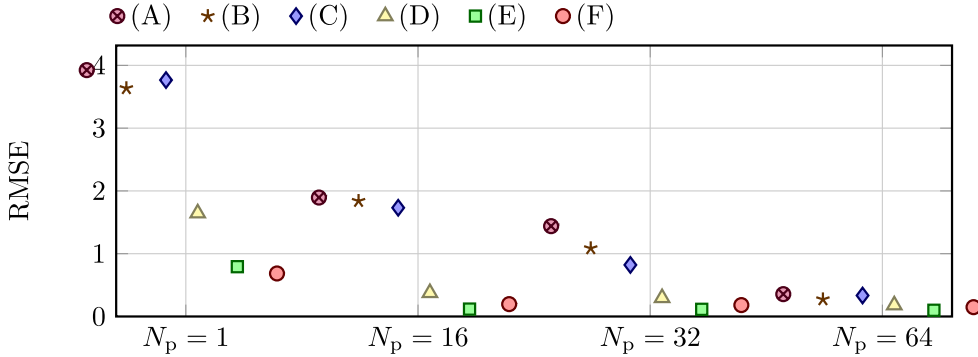


Figure 107: RMSE for different number of pulses for : (A) empirical TSD with $M = 5$; (B) empirical TSD with $M = 100$; (C) TSD; (D) empirical ESD with $M = 5$; (E) empirical ESD with $M = 100$; (F) ESD.

is obtained as

$$\Lambda_{\text{TSD}}(\boldsymbol{\zeta}|\hat{i}) = f_{\text{I}}(\hat{i}|\boldsymbol{\zeta}, \boldsymbol{\theta}_h, \boldsymbol{\theta}_d). \quad (46)$$

where $f_{\text{I}}(\hat{i}|\boldsymbol{\zeta}, \boldsymbol{\theta}_h, \boldsymbol{\theta}_d)$ is the PMF of the selected bin index I conditioned on the event $\mathcal{C}_{\text{th}} = \{\exists \in \mathcal{B} : > \xi\}$ and $\boldsymbol{\theta}$. Such a PMF is given by¹⁸

$$f_{\text{I}}(i|\boldsymbol{\theta}) = \left[1 - F_{B_i}(\xi_i|\boldsymbol{\theta}) \right] \prod_{j \in \mathcal{J}()} F_{B_j}(\xi_j|\boldsymbol{\theta}) \left[1 - \prod_{n \in \mathcal{B}} F_{B_n}(\xi_n|\boldsymbol{\theta}) \right]^{-1}$$

where $f_{B_i}(\xi_i|\boldsymbol{\theta})$ and $F_{B_i}(\xi_i|\boldsymbol{\theta})$.

Consider a localization system where N_a anchors, the k th anchor at \mathbf{p}_k and $k \in \mathcal{A} = \{1, 2, \dots, N_a\}$, are employed to locate a target at unknown position \mathbf{p} . Ranging based on energy detection (either hard-decision or soft-decision) is performed at each anchor.

In the case of hard-decision ranging, the selected index \hat{i}_k is provided at each anchor k as the input for the localization algorithm. A commonly used localization algorithm is to adopt the method of least-squares.

In the case of soft-decision ranging, a reduced dataset is provided at each anchor k as the input for the localization algorithm. The localization algorithm first computes the range likelihood function based on (45) and (46) for ESD and TSD, respectively. Then, it estimates the location of the target as that maximizing the likelihood.

Note that the evaluation of the likelihood function requires the PDF of the energy bins $f_B(b|\tau, \boldsymbol{\theta}_h, \boldsymbol{\theta}_d)$ and of the selected bin $f_{\text{I}}(\hat{i}|\tau, \boldsymbol{\theta}_h, \boldsymbol{\theta}_d)$ for ESD and TSD, respectively. They can be approximated based on the tractable range information model given in [61], leading to the theoretical likelihood functions in (45) and (46). Alternatively, they can be estimated based on measurements, leading to the empirical likelihood functions. By collecting M outcomes $\check{b}_{i,m}(\tau)$ and $\check{i}_m(\tau)$ of the RVs B and I with $m = 1, \dots, M$, the PDF can be approximated with the empirical distributions $\hat{f}_{B_i}^{(M)}(b_i|\tau, \boldsymbol{\theta}_h, \boldsymbol{\theta}_d)$ or $\hat{f}_{\text{I}}^{(M)}(\hat{i}|\tau, \boldsymbol{\theta}_h, \boldsymbol{\theta}_d)$.

In particular, we consider to gather M diverse measurements for each value of $\tau \in \mathcal{T}$ for a finite set \mathcal{T} of values. The empirical distributions are obtained as The empirical likelihood converges to the exact likelihood as M goes to infinity almost surely. Such a likelihood represents the prior knowledge about the operating environment that has been obtained by collecting measurements before the beginning of the localization process.

Remark: Note that the energy detection is distributed at each anchor, whereas the localization process is centralized. Therefore, the dataset size $|\mathcal{D}|$ for the range likelihood is an important parameter influencing the resource utilization for communicating the likelihood functions. In this perspective, the TSD and

¹⁸The index set $\mathcal{J}_{N_w}(m)$ is defined as $\mathcal{J}_{N_w}(m) = \mathcal{B} \cap \{m - N_w, m - N_w + 1, \dots, m - 1\}$ and is empty for $N_w \leq 0$.

TCS use a dataset with minimum size. In particular, the dataset size for the TSD is $|\mathcal{D}| = |\{\hat{\tau}\}| = ;$ the dataset size for the TCS is $|\mathcal{D}| = |\{\hat{\tau}\}| = .$ The ESD has dataset size $|\mathcal{D}| = |\mathbf{b}| = \mathcal{N}_b.$ Recall that original observation dataset is $|\mathcal{D}| \geq \mathcal{N}_{sb}\mathcal{N}_b.$ Therefore, the complexity of the proposed algorithms is significantly reduced compared to the localization algorithms with traditional soft-decision ranging.

Consider a localization network consisting of anchors at the corners of a square with side length equal to 10m. Each anchor emits a sequence of UWB root-raised cosine pulses with pulse repetition period $T_{pr} = 150\text{ ns}.$ The transmitted power spectral density is compliant with the emission masks according to the USA regulations (Federal Communication Commission) [67]. The wireless medium follows the IEEE 802.15.4a channel model for UWB indoor residential LOS environments [68].

The received signal is processed based on energy detection with observation time $T_{obs} = 256\text{ ns}.$ In the case of hard-decision ranging, we consider $\xi_i = \xi \forall i \in \mathcal{B},$ where ξ is chosen according to [61, eq. (44)]. The received SNR per pulse is $\gamma = E_p/N_0,$ where E_p is the energy of the received signal pulse and $N_0 = -110\text{ dBm/MHz}$ is the one-sided power spectral density of the noise component.¹⁹ Unless otherwise stated, the results in the following are provided for $N_b = 128,$ $T_d = 2\text{ ns},$ and $N_p = 32.$

Localization results are obtained with hard-decision and soft-decision ranging. For the soft-decision case, we consider both the ESD and the TSD algorithms. For the empirical distribution are conditional on $\tau \in \mathcal{T},$ where \mathcal{T} has 150 values linearly spaced between 0 and $T_a.$

We refer to the different system settings as: (A) empirical TSD with $M = 5;$ (B) empirical TSD with $M = 100;$ (C) TSD; (D) empirical ESD with $M = 5;$ (E) empirical ESD with $M = 100;$ (F) ESD; and (G) TCS. Fig. 107 shows the root mean square error (RMSE) for different number of N_p and system settings (A) – (F). Results show that when the value of N_p is high, all the algorithms have similar performance despite the different complexities. Differently, for low values of $N_p,$ the ESD outperforms the TSD for any value of $M.$

5.7 System Integration

The overall UWB-RFID network architecture comprises a central unit, readers and tags. Each reader communicates with the central unit mostly for transferring the signal processing data (e.g., the TOA estimates allowing the tag localization). In addition, these connections can be exploited to ensure a general coarse synchronization between the readers, as well as for network maintenance. Readers' synchronization will be further detailed in Sec. 5.7.2.

Define \mathcal{T}, \mathcal{E} and \mathcal{R} as the set of tags, transmitters and receivers in the environment, respectively, with cardinality $|\mathcal{E}| = N_t,$ $|\mathcal{R}| = N_r$ and $|\mathcal{T}| = N_{tag},$ with tags placed in unknown positions $\mathbf{p}_k = (x_k, y_k),$ with $k = 1, 2, \dots, N_{tag}.$

In [30], two different readers configurations are distinguished. In the former, the monostatic network, transmitters are co-located with receivers in known positions $\mathbf{p}_{Ri} = (x_{Ri}, y_{Ri}),$ with $i = 1, 2, \dots, N_r,$ and each reader post-processes only the backscattered signal related to its transmitting section. In the latter, the multistatic network, transmitters and receivers, placed in $\mathbf{p}_{Tj} = (x_{Tj}, y_{Tj})$ and $\mathbf{p}_{Ri} = (x_{Ri}, y_{Ri}),$ respectively, with $j = 1, 2, \dots, N_t,$ and $i = 1, 2, \dots, N_r,$ are not necessarily co-located. In fact, each receiver can post-process the backscattered signal related to other transmitters. Note that while in traditional RFID systems readers are usually in monostatic configuration, here transmitters and receivers can be also separated, and thus readers' complexity is reduced. On the other hand, synchronization with a separated transmitter has to be carefully addressed (see Sec. 5.7.2). The two solutions may be also combined in hybrid architectures, where a receiver listens to a subset of the transmitted interrogation signals. In the remainder of the paper it is referred to as *reader* the reference node composed of at least a receiver. Recently, practical advantages of multistatic configurations for RFID networks, including enhanced localization accuracy and interference rejection, have been highlighted [4, 28, 30].

In this section the challenges and the solutions concerning the multi-reader network deployment are presented.

¹⁹The noise has mean zero and variance $\sigma^2 = N_0W,$ where W is the bandwidth of the transmitted signal that is defined by the emission masks.

5.7.1 Multi-Reader Coexistence

As already described, in the UWB-RFID network several readers monitor a certain area (four in the reference scenario of Fig. 100). It is then necessary to enable the possibility of accessing the same tag by multiple transmitters, with a potential problem of inter-reader interference.

For this analysis, the reference scenario reported in Fig. 100 is considered. As worst case, the presence of obstacles is neglected, assuming that the largest interference comes from the opposite transmitter in case of line-of-sight propagation.²⁰ Without loss of generality, we focus on the interference generated by Reader 3 (opposite transmitter) on the Reader 1, whose aim is to detect the tag presence by analyzing the backscattered response to its own transmitted signal. Thus, it is possible to foresee three different signal contributions:

1. The interfering signal of Reader 3 backscattered by the intended useful tag for Reader 1;
2. The direct path (and the multipath) between Reader 3 and Reader 1, responsible for the strongest interfering signal;
3. The interfering signal of Reader 3 backscattered by a tag different from the useful one.

5.7.1.1 CDMA Approach

If a CDMA-based technique is adopted for handling the multi-readers access, even a low residual interference component can completely vanish the possibility of detecting a tag signal.²¹ We assume that the interrogation signals transmitted by Reader 3 and Reader 1 are generated adopting the spreading codes $\{\tilde{d}_n^{(3)}\}$ and $\{\tilde{d}_n^{(1)}\}$, respectively, and that the useful and the interfering tags have codes $\{\tilde{c}_n^{(u)}\}$ and $\{\tilde{c}_n^{(\text{int})}\}$, respectively. To detect the presence of the useful tag, Reader 1 performs a de-spreading using the composed code $\{\tilde{d}_n^{(1)} \cdot \tilde{c}_n^{(u)}\}$. In particular, relating to the previously presented three cases, the multi-reader interference is cancelled provided that the following three conditions are satisfied:

- Cancellation of the Reader 3 interference component modulated by the useful tag:

$$\sum_{n=1}^{N_s} \tilde{d}_n^{(1)} \tilde{c}_n^{(u)} \tilde{d}_n^{(3)} \tilde{c}_n^{(u)} = \sum_{n=1}^{N_s} \tilde{d}_n^{(1)} \tilde{d}_n^{(3)} = 0. \quad (47)$$

- Cancellation of the direct Reader 3-Reader 1 interference:

$$\sum_{n=1}^{N_s} \tilde{d}_n^{(1)} \tilde{d}_n^{(3)} \tilde{c}_n^{(u)} = 0. \quad (48)$$

- Cancellation of the Reader 3 interference component modulated by another tag:

$$\sum_{n=1}^{N_s} \tilde{d}_n^{(1)} \tilde{c}_n^{(u)} \tilde{d}_n^{(3)} \tilde{c}_n^{(\text{int})} = 0. \quad (49)$$

Note that condition (47) is satisfied adopting orthogonal codewords and ensuring a tight synchronization between the readers (see Sec. 5.7.2). Differently, (48) and (49) are substantially different from the classical conditions where good cross-correlation properties are required between pair of sequences [69], since here the products of three or four sequences are involved. These stringent requirements must be fulfilled for all the possible readers' sequences $d_n^{(j)}$ and all the possible tag sequences $c_n^{(k)}$ (and their cyclic shifts due to the partial tags asynchronism) since it is necessary to remove the interference due to all the possible readers and tags. Due to the additional constraints on tag code design to avoid interference [2], this poses several challenges on readers' codes design, especially for the almost-ideal interference cancellation capability required.

²⁰In general it is possible to assume a lower level for the interference of the two neighbor readers in the case of partial directive antennas at transmitting and/or receiving stage, while a higher level for the interference coming from the two neighbor readers in case of adoption of omnidirectional antennas.

²¹It can be shown that the difference between the power received by the opposite transmitter interference and that of a tag at 7 m from the reader is about 50 dB.

5.7.1.2 TDMA Approach

For the aforementioned analysis, it is clear how the simultaneous interrogation of multiple transmitters is critical, and simpler solutions, such as TDMA, have to be accounted especially for low-complexity realizations. Specifically this consists on alternating in a cyclic way the transmitter, and setting the other readers in receiving mode. With the TDMA, the interference problem coming from other transmitters is completely avoided. TDMA can be performed at different rates considering the alternation of the transmitter, for example, each symbol or each packet. Decreasing the switching rate between transmitters (e.g., implementing TDMA at packet level) allows preventing problems deriving from synchronization mismatches, whereas the main drawback is the reduction of the refresh rate and constraints on the maximum tags' allowed speed, when tags' tracking is performed. It is worthwhile to highlight that even the multi-reader access is TDMA-based, the multi-tag access is still CDMA-based.

5.7.1.3 Multistatic Configuration

An interesting alternative is represented by the adoption of a multistatic configuration with one only transmitter and at least 3 receivers [30], as in UWB radar sensor networks [70–76]. In this manner the number of receivers is sufficient to provide unambiguous localization, and the multi-transmitter interference problem is completely avoided. On the contrary, with this configuration, the diversity provided by the signals from more than one transmitter is no more available, and it is fundamental to guarantee the perfect visibility of the tag antenna with the transmitter, avoiding NLOS conditions.

5.7.2 Readers Synchronization

Readers must be kept synchronized in order to ensure satisfactory multiple access performance and to allow multistatic functionalities. Readers' coarse synchronization can be provided with the readers-central unit links (e.g., realized with a standard Ethernet protocol). Readers' fine synchronization can exploit the same UWB interrogation signals emitted by transmitters, hence re-using the same hardware developed for tag detection. In fact, the lower pathloss of the direct transmitter-to-receiver link ensures a very high SNR for the demodulation of the transmitter signal (static contribution), allowing very accurate (sub-nanosecond) TOA estimation. In this case, the de-spreading is operated according to the incoming transmitter's code $\tilde{d}_n^{(j)}$ only, without accounting for the tag code. Since the transmitter-receiver distance is fixed, TOA estimation can be compared with the expected propagation time between the two antennas, adjusting consequently the reader's clock according to the difference between the estimated and expected range. The process can be further iterated until the difference in the clock adjustment falls below a threshold, indicating the reached synchronism.

Summarizing, the synchronization process is enabled through two facts: (i) transmitters are placed in known positions; (ii) de-spreading operation is conducted exploiting the transmitters' code $\{\tilde{d}_n^{(j)}\}$ only, resulting in the isolation of the static contribution $r_{i,j}^S(t)$ at receiver side. Specifically, by performing TOA estimation on the signal $r_{i,j}^S(t)$, the i th receiver estimates $\hat{\tau}_{i,j}' = \hat{\tau}_{i,j} + T_{i,j}$, where $T_{i,j}$ is the unknown clock offset between the j th transmitter and the i th receiver. Since transmitters' and receivers' positions are known, the true distance $d_{i,j} = |\mathbf{p}_{Tj} - \mathbf{p}_{Ri}|$ between the transmitter and the receiver composing the bistatic pair can be exploited to determine $T_{i,j}$ and synchronize the receiver with the transmitter.

5.7.3 Tags Localization

After the initial readers' synchronization step, a second de-spreading operation conducted with the composed code $\{\tilde{d}_n^{(j)} \cdot \tilde{c}_n^{(k)}\}$ allows isolating the k th tag component $r_{i,j}^T(t)$. Now, TOA estimation of such a signal gives $\hat{\tau}_{i,j,k}$, and consequently $\hat{d}_{i,j,k} = c \hat{\tau}_{i,j,k}$, which corresponds to the estimation of the sum $d_{Tj} + d_{Ri}$. The term $\hat{d}_{i,j,k}$ can be exploited to define the ellipse related to the bistatic pair of interest, with the foci located in the considered transmitter and receiver. With the intersection of several ellipses the tag's position is then determined [77], as usually realized in radar networks where transmitters and

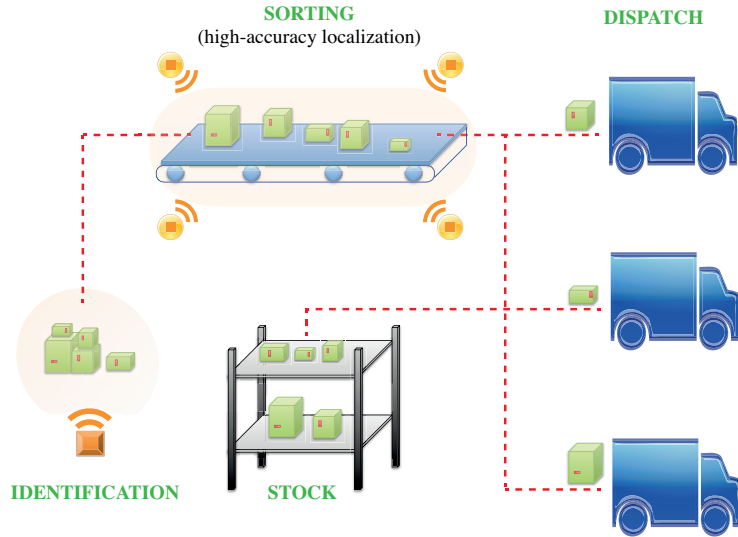


Figure 108: IoT application example.

receivers are often not co-located. Notice that, when a monostatic configuration is adopted, the receiver is intrinsically synchronous with the co-located transmitter, and the reader-tag distance is directly computed from the round-trip time (RTT). In this case localization is simply realized with the intersection of circumferences [78].

Recently, performance bounds for the localization accuracy in both monostatic and multistatic RFID configurations have been derived [30, 79], highlighting the role of system parameters, network configuration and topology.

5.7.4 Alternative Approaches considering Mode 2 and Mode 3 UHF-UWB Tags

In the previous sections, it has been shown that even if the passive UWB-RFID architecture is very promising, it might suffer from several issues. Thus, in this section, a new appealing solution for Internet of Things (IoT) applications is introduced. The idea is based on the integration of the previously described UWB tag with a standard UHF EPC Gen.2 tag.

A typical supply chain scenario is considered, where these proposed hybrid RFID tags are applied on goods which travel inside the factory. Tags identification can be normally realized with the UHF Gen.2 readers, exploiting the compatibility of the tags with the standard protocol. When goods enter in a critical area where high-accuracy location information is fundamental, for example in a section of a conveyor belt where they need to be correctly sorted (see Fig. 108) [80–82], the additional UWB interface can fulfill the high-accuracy localization requirement. Fig. 109 presents the general scheme of the hybrid UHF-UWB tag, which offers the important advantage of resulting compatible with the state-of-the-art Gen.2 tag. The UWB interface can be viewed as an *add-on* allowing accurate tag localization, which represents an extremely appealing feature for practical applications. In the following, two possible architectures exploiting these hybrid tags are discussed, according to the GRETA modes 2 and 3 presented in Sec. ??.

5.7.4.1 Option 1: UHF-UWB Portals

The first architectural solution for the exploitation of the hybrid UHF-UWB tags consists in the adoption of a UHF portal placed at the entrance of the area where localization becomes critical. Such a portal guarantees a log-in phase of the hybrid tags that are registered in the critical area. However, differently from the stand-alone UWB tags previously described, the portal assigns a dedicated codeword $c_n^{(k)}$ to each tag by exploiting the Gen.2 link communication capability. Such codeword is successively adopted by the UWB-RFID network for providing simultaneous multiple tags localization inside that critical area

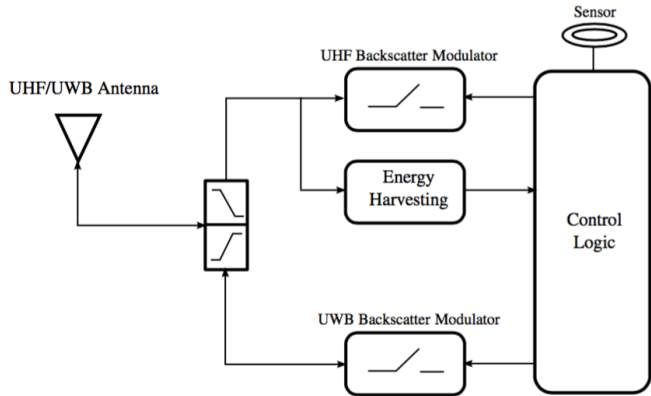


Figure 109: General Architecture of Hybrid UHF-UWB tag.

only. In this manner, the few available codewords can be reused in several separated areas, managed by different portals, improving the system efficiency and avoiding the need of a unique spreading sequence per tag. Moreover, the standard Gen.2 tag-reader link can be used also for data communication (i.e., to transfer sensor data from the tag). In this case, there is no need of exploiting the UWB tag-reader link for data communication, and a single bit in the UWB packet, that is, $N_p = 1$, is sufficient for tag ranging (i.e., only N_s pulses per tag are sent and backscattered). In this way, the specifications on the tag local oscillator can be relaxed, as the clock drift problem will not impact the short transmitted packet [42]. Since now only one bit has to be transmitted, the number of pulses N_s can be significantly enlarged to provide improved detection range and accurate TOA estimation thanks to the increased process gain.

Such an architectural solution ensures high refresh rate since the simultaneous UWB tags' access based on CDMA is exploited, but maintains the intrinsic problems discussed in the previous sections of the UWB-RFID, such as multi-reader and multi-tag interference. The last effect can be partially mitigated by the exploitation of several portals with only few tags simultaneously active. It is important to underline that the tag power consumption is increased due to the presence of the Gen.2 UHF circuitry with respect to the stand-alone UWB tag.

5.7.4.2 Option 2: Tight UHF-UWB Interaction

This second architectural solution is capable of overcoming the multi-tag interference problem, as it is completely managed by the standard Gen.2 RFID. The idea is to introduce a tight interaction between the UHF and the UWB protocols [7]. In this case, the UHF reader broadcasts an addressing command for a specific tag with the Gen.2 signaling. All the tags demodulate such UHF Gen.2 signal, but only the specific tag addressed activates its UWB backscatter modulator. In such a manner, only one UWB tag is active in each interrogation and, consequently, the multi-tag interference is completely avoided. In addition, the receiver structure is enormously simplified, as only one codeword can be shared among all tags without the need of replicating the receiver structure. Thus, differently from the adoption of the stand-alone passive UWB-RFID, the UHF-UWB system has no limitations in terms of number of manageable tags. As for the previous option, data communication can be performed with the UHF link in order to maintain a short UWB packet and increase the number of pulses per symbol.

Finally, this alternative solution is beneficial also for the multi-reader deployment. In fact, conditions (47), (48), (49) necessary for avoiding multi-reader interference are easily satisfied since, with the adoption of this architecture, only one tag backscatters the incoming readers' signals. Consequently, good cross-correlation properties are easier to find with a single tag codeword.

This configuration presents an additional drawback to that of the increased power consumption: in fact, the refresh rate of the UWB sub-architecture is significantly reduced since one only tag is active and multiple tags are scheduled in different time instants. However, if data communication is delegated to

the UHF signaling in order to preserve a short UWB packet, the intrinsic refresh rate reduction is in part compensated by the shorter duration of such a packet.

These solutions let to merge most of the benefits of both UHF and UWB RFID schemes, by maintaining a substantial low system complexity.

5.8 Identification and Network Management Protocols

The adoption of ultra-wide-band (UWB) technology has been envisaged as a promising solution to overcome the limits of ultra high frequency (UHF) techniques towards the definition of green RFID systems. Reducing energy consumption is also becoming a demanding requirement, and consideration of the environmental impact of RFID systems (e.g. through the use of recyclable materials) [1, 83] is also a major concern: UWB-based solutions would be useful on this purpose. Moreover, the capability of localizing and tracking passive (or semi-passive) devices through UWB signals is a key feature for several types of applications and is also useful to improve the performance of the existing systems [84].

UWB-based solutions have been already employed for active tags due to their low power consumption, however passive tags solutions are envisioned as preferable due to their low cost.

Anyway, UWB passive solutions are under investigation and show several drawbacks, such as i) poor link budget with consequent difficult signal detection at the reader receiver, ii) complex detection of multiple tags, which would require several processing units at the reader receiver, each one tuned on the specific tag code, iii) the problem of extracting energy from UWB signals due to regulatory issues. Thus, a hybrid UWB/UHF architecture could be useful to exploit UHF signal to transfer the required amount of energy to the tag.

However, the possible integration of a UWB module with the existing UHF RFID standard technology has not been investigated yet and is one of the targets of the GRETA project [85]. A few alternatives of hybrid UWB/UHF tag architectures have been investigated [85], with UHF only used for energy transfer or with the UHF section providing also the communication capability. We here consider a UHF module for energy transfer and communication for tags identification, while an UWB module is used to assist and improve such tags identification process.

We develop two hybrid UWB/UHF solutions: one of those exploits UWB signals to enhance the standard ISO/IEC 18000-6C UHF, which employs a Framed-Slotted ALOHA (FSA) collision arbitration with dynamic frame adaptation. The other one improves a compressive sensing (CS) based solution in the multi-reader, multi-tag scenario [86], by also considering synchronization errors.

In the first case, we propose an enhanced version of the adaptive Q -algorithm enforced by the EPC-Global Generation 2 protocol. The proposed solution is based on an UWB-aided identification procedure that support tag population estimation and ranging to improve the tags identification performance by reducing the occurrence of collisions. We describe the proposed solution for the single-reader scenario and then provide the guidelines to extend the enacted Q -algorithm to multi-reader systems. In particular, we describe the reader synchronisation policies and empathize how the readers' cooperation paradigm is essential for the development of an efficient and reliable RFID multi-reader system.

In the second case, the novel CS-based solution combines UWB information to reduce the total amount of time slots spent for tags identification [86]. Indeed, CS [87], [88] has been proposed as an alternative to the state-of-the-art FSA approach, which does not need to avoid collisions. However, when considering large tag population as in common RFID applications, the main problem in CS is to reduce the ID search space. We divide all the tags in groups, which are associated to UWB group codes. The UWB module, which operates at chip level, is used to quickly estimate the number of tags with data to transmit and to rapidly recognize the group codes they belong to; the UHF module, that operates at bit level, is used to identify the tags through a CS procedure. Moreover, we model and evaluate the effect of timing synchronization error on the proposed solution. Both standard-based ISO/IEC 18000-6 and CS approaches benefit from tags population estimation to minimize the total number of time slots spent by the reader for tags' identification.

Besides single-reader scenario, we extend our work in the multi-reader scenario. Indeed, some ap-

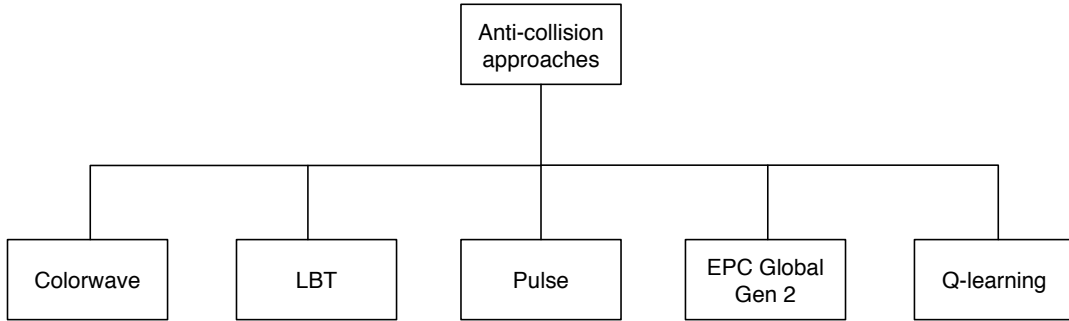


Figure 110: Multi-Reader Anti-Collision Approaches

plications are characterized by the deployment of large populations of tags, and single reader systems may not be sufficient to cover the area of interest. Thus, multi-reader solutions have been proposed to overcome limitations of a typical single reader system. We here consider and model several interference problems that are absent in the case of a single reader scenario and investigate possible solutions to face with these issues.

The rest of the Sec. 5.8 on network management protocols is structured as follows. Sec. 5.8.1 describes the state of the art in multi-reader systems, while Sec. 5.8.2 provides the features of the hybrid UWB/UHF architecture. The single reader scenario is described in Sec. 5.8.3, where both the proposed FSA and CS based solutions are described, and in Sec. 5.8.4 the extension of the proposed algorithms to the challenging multi-reader scenario is detailed. Finally, some comments on the presented results are detailed in Sec. 5.8.5 and future perspectives conclude the report.

5.8.1 Related Work

Unlike single reader systems, where tags are the only interfering entities, in multi-reader scenarios readers and tags are both interfering and interfered entities. Thus, different kinds of collision problems arise and have to be handled to properly analyse the systems and achieve adequate performance. Different approaches have been proposed to mitigate and solve the so called reader collision problem (i.e. a reader is the interferer and either a tag or another reader is the interfered entity). The most popular anti-collision approaches for multi-reader systems are summarised in Fig. 110.

One of the first proposed protocols to contrast reader collisions is a Time Division Multiple Access (TDMA) techniques known as *Colorwave* [89]. Colorwave is a distributed algorithm in which each reader chooses a random time slot used for query transmissions. If two readers choose the same time slot, a collision occurs. In this case a colliding reader chooses a different time slot and forwards a message to its neighbour readers to notify such a change. The main drawback of this approach is the required time synchronization between readers.

ETSI EN 302 208 [90] standard adopts a *Carrier Sense Multiple Access* (CSMA) based approach known as *Listen Before Talk* (LBT). Before transmitting a query, the reader senses the channel for a specified amount of time. If the channel is sensed idle, the reader begins the reading procedure, otherwise it waits a random back-off time waiting for the channel to become idle. Note that, as in traditional carrier sense based protocols, LBT suffers for the *hidden terminal problem* and thus may not be able to detect and solve collisions. Authors in [91] propose a *beaconing-based* technique called *Pulse*, that does not offer for the hidden terminal process. This protocol relies on the presence of two non-interfering channels. A control channel is reserved for reader-to-reader communication, while a data channel is used

for identification process. When a reader is in the reading phase, simultaneously broadcasts a beacon over the control channel to notify the ongoing communication in order to prevent neighbor readers to transmit over a busy data channel. This protocol may results in high delay when the number of readers is large.

Also Frequency Division Multiple Access (FDMA) based approaches can be adopted to mitigate reader collision problems. Unfortunately, FDMA-based protocols are only effective in solving reader-reader protocols unless the tags have frequency selectivity, which is not the case of passive systems. The standard EPCGlobal Generation2 suggests the use of FDMA for multi-reader operations, but does not specify how to coordinate the network of readers. However, the ETSI regulation dictates that readers can transmit over a specific channel only for a limited amount of times, thus reader coordination strategies should take into account this limitation imposed by the standard.

An approach based on learning theory is proposed in [92]. In particular the authors develop an online algorithm called *Hierarchical Q-Learning* (HiQ) that dynamically assigns frequency channels based on readers' access patterns observation. The algorithm attempts to find an optimum frequency assignment in order to prevent collisions to neighbor readers. The optimization problem is solved by means of a particular type of reinforcement learning called Q-learning.

Finally, great research effort has been recently devoted in finding MAC solutions for multi-reader systems, by allowing networked readers to operate either concurrently or cooperatively with the common goal of improving systems interrogation performance and reliability. Some examples of optimal reader activation scheduling can be found in [93].

We propose to use a hybrid UWB/UHF architecture to improve tags' identification both in single-reader and multi-reader scenarios. We develop two solutions: the first one exploits UWB signals to enhance the standard ISO/IEC 18000-6C UHF, the second one exploits UWB to improve the CS based solution.

5.8.2 UWB/UHF Hybrid Architecture Features

5.8.2.1 Opportunistic UWB signal

The tag population cardinality is in general unknown. Counting the number of tags within a certain region is one of the key problems strictly related to the tag identification process. While its usefulness is evident in those applications where it is desirable to only count the number of RFID tags, estimating the tag population cardinality provides a useful support in any case. In [94] the cardinality estimation problem is analyzed in two different versions: the *single-set RFID counting* problem and the *multiple-set RFID counting* problem. The single-set problem is directly connected to single-reader systems, while the multi-set counting problem arises in multi-reader systems or in a system for which a single mobile reader probes different interrogation areas.

Different counting approaches and protocols have been proposed in the literature. In [94] the authors point up that all the proposed techniques are based on a common approach of dividing the counting process in *rounds*. Within rounds the number of tags can be estimated from various statistical metrics extracted from the observed tags' response patterns. The development of accurate and efficient counting protocols requires, in general, two estimation phases. The idea is to start with a rough estimation during the first phase, and refine the result in a second phase to achieve the desired accuracy.

Very fast, reliable and efficient tag population estimation can be achieved by employing UWB backscattering communication [95], [96]. In particular, backscattering communication uses modifications of antenna reflection properties at the tag to transmit information. In general, due to the short pulse duration (typically less than 1 ns), the bandwidth of the transmitted signal can be on the order of one or more GHz.

The UWB signal transmitted to a tag is modulated using an antipodal pseudo-random binary code to uniquely identify the reader (reader's code). The UWB pilot signal is backscattered by the tag as well as by all the surrounding scatterers in the environment. In particular, at each chip time the backscattered signal associated with the k -th tag is modulated by the combination of reader's and tag's codes. Differently, the environmental reflected signal (i.e., clutter components, which includes the structural antenna mode) exhibits modulation only by the reader's code. The pulse repetition period is typically chosen so

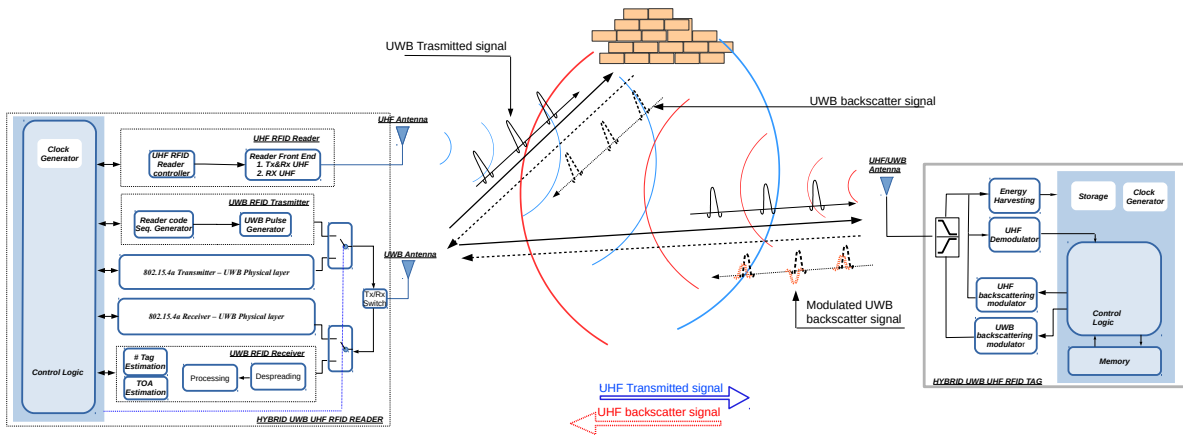


Figure 111: System Architecture

that all signals backscattered by the environment are received by the reader before the transmission of the successive pulse. In indoor scenarios a 100 ns repetition interval is usually sufficient to this purpose [97].

Consider a reader that interrogates a set of tags in its communication range by transmitting an UWB signal with a specific spreading code. For population estimation, it is reasonable to consider that tags share the same code. Considering that all tags backscatter in the same way, the estimation of the tag population is related to the analysis of the energy collected by the UWB receiver at the reader. Due to the different times of arrival (ToA) of backscattered signals from nodes at different distances, the reader may be able to distinguish the presence of tags at different distances. The tag population estimate results in estimating the number of backscattered pulses, although the channel delay spread should be accounted for in a realistic propagation scenario. Using different codes on the tag side may improve the detection performance, while increasing complexity. The accuracy is measured in terms of maximum estimation error on the interrogation ranges, which returns an error on the number of tags actually present within a given range. In a next phase, assuming that a tag has been identified, by measuring the ToA of the backscattered signal the reader is able to estimate the distance (ranging operation) and then provide an input to one or more algorithms for estimating the position of the tag.

The integration of classic UHF architectures and backscattering UWB communication enables the development of interesting solutions from a MAC layer perspective. Indeed, fast tag population estimation can be used as a support for the interrogation process, improving collision resolution techniques provided by the existing standard. In particular, referring to EPCGlobal Generation 2 protocol, UWB technology allows to overcome drawbacks of the adaptive *Q-Algorithm*, which provides dynamic frame length update only based on the observation of collided and idle slot patterns. On the contrary, having available an estimate of the number of tags involved in the interrogation process allows to develop more efficient frame length update algorithms for framed ALOHA-based MAC protocols.

Moreover, UWB backscattering can be successfully employed as the core technology in developing *multi-reader cooperative systems*. Classical MAC solutions presented in this field are based on concurrent readers' operations. However, more efficient and robust solutions may be developed by allowing readers to cooperatively operate for targeting some common performance requirements. In this perspective, ranging and tags' population estimation are required informations for designing cooperative readers networks for large-scale RFID systems characterized by real-time requirements, high identification reliability and accurate localization.

UWB backscattering communication allows for multi-reader cooperative solutions that can effectively improve system efficiency and robustness.

5.8.2.2 System Architecture

The hybrid UHF/UWB system architecture and the propagation scenario considered in this work are depicted in Fig. 111.

Hybrid UHF/UWB Reader. The reader is equipped with an UHF front-end for UHF domain operations. In particular, the reader relies on the UHF band for tag energization, synchronization and inventory commands as in classic EPC Global Generation 2 based systems. We assume that the reader has online power control and multi-frequency communication capabilities. These features are needed to mitigate interference problems in multi-reader systems as we discuss later in the report.

In the UWB domain the reader is equipped with a full IEEE 802.15.4a based communication system. As we discuss later, this communication structure is needed to exploit readers' cooperation (i.e., data exchange between readers) and readers discovery in multi-reader scenarios. Furthermore the reader is equipped with a UWB receiver for backscattered signals. This module is used for tag population estimation and ranging. A control logic unit is required to properly coordinate the operations in the two different domains and again we assume two logically separated antennas for UHF and UWB operations.

Hybrid UHF/UWB Tag. In the UHF domain a passive tag collects the power from the RF signal transmitted by the reader (i.e., tag energization). The energy harvesting unit and the storage module (i.e., usually a small capacitor) are used to provide energy supply for tag operations. Communication in the downlink (i.e., tag-reader link) takes place in backscattered fashion. In particular, the tag interprets the reader's command by means of the UHF demodulator and sends data back by switching the impedance of the antenna, typically between two states, thus modulating the backscattered UHF signal. In the UWB domain, the already energized tag may transmit back information by modulating the backscattered UWB pulses, similarly to the UHF domain, by switching impedance of the relative antenna.

The tag is equipped with a hybrid UHF/UWB antenna to properly operate in the two domains. We assume that the UHF and UWB antenna components are logically decoupled but can be implemented as a single physical antenna system. Details about hybrid antenna structures and fundamentals on backscattering communication can be found in [98] and [99]. Note that a control circuit is required to properly operate in the two coexisting bands.

Given the definition of the tag UWB module, the backscattered signal at the reader's receiving front-end, which accounts for the contributions of the tags in the covered area, can be expressed as an infinite sequence of pulses separated by T_f seconds (frame time) as [1]:

$$r(t) = \sum_{k=0}^{K-1} r^k(t) + \sum_{n=-\infty}^{+\infty} d_n \omega^{(c)}(t - nT_f) + n(t) \quad (50)$$

where K is the number of tags to be identified, $r^k(t)$ is the received backscattered signal from the k -th tag, $n(t)$ is the additive white Gaussian noise (AWGN), d_n is the reader's code, and $\omega^{(c)}(t)$ is the backscattered version of the transmitted pulse due to the clutter component, which accounts for pulse distortion, multi-path propagation, and tag's antenna structural mode.

By assuming that all tags are synchronous, (i.e., $\Delta^k = 0$), the k -th contribution to the received signal defined in (50) is:

$$r^k(t) = \sum_{m=-\infty}^{+\infty} \sum_{n=N_x}^{N_{pc}-N_x-1} d_n d_m^k \omega^k(t - nT_f - mT_c) \quad (51)$$

where N_{pc} is the reader's code length, N_x is the number of pulses associated to half synchronization error safeguard, d_m^k is the code of the k -th tag, $\omega^k(t)$ is the backscattered version of the transmitted pulse coming from the k -th tag, and T_c is the chip time. In general $\omega^k(t)$ accounts for pathloss, multi-path and delay induced by propagation channel.

Single-Reader		Multi-Reader		
	Enhanced Q-Algorithm	Compressive Sensing	Enhanced Q-Algorithm	Compressive Sensing
UHF	<ul style="list-style-type: none"> • Tag energization; • Tag synchronization; • Inventory and control commands; • Online power control; 	<ul style="list-style-type: none"> • Tag energization; • Tag synchronization; • Special command for UHF CS decoding (CS-Query); 	<ul style="list-style-type: none"> • Tag energization; • Tag synchronization; • Inventory and control commands; • Online power control; • Multi-frequency operations; 	<ul style="list-style-type: none"> • Tag energization; • Tag synchronization; • Special command for UHF CS decoding (CS-Query); • Single-frequency operations;
UWB	<ul style="list-style-type: none"> • Tag population estimation; • Ranging; • Multi-code aided estimation; 	<ul style="list-style-type: none"> • Tag population estimation; • Multi-code for tag groups identification; 	<ul style="list-style-type: none"> • Readers communication/cooperation; • Readers synchronization; • Tag population estimation; • Ranging; 	<ul style="list-style-type: none"> • Readers communication/cooperation; • Readers synchronization; • Multi-code for tag groups identification;

Figure 112: Summary Table

Note that, according to different purposes, we can assume a different set of tag codes. For example, the tags may be associated to different codes d_m^k for identifying the tags by only using the UWB module, or they can use the same code d_m for tag population through an energy estimation.

Fig. 112 shows a schematic overview on how the reader features are exploited by the enhanced *Q*-Algorithm and the compressive sensing approaches for both single-reader and multi-reader systems. Observe that tags are compatible with readers operation given the considered architecture.

5.8.3 Single Reader Scenario

In a single reader scenario, the operations on the UHF domain and UWB domain can be illustrated as follows. In the UHF domain, a passive tag collects power from the RF signal transmitted by the RFID reader and sends data back by modulating the backscattered UHF signal. In the UWB domain, the already energized tag transmits back information by modulating the backscattered UWB pulses. The UHF and UWB links can operate simultaneously both on the reader's and tag's side. Here the reader uses UHF for identification, while the UWB technology is adopted for tags' population estimation.

An interrogation round is defined as a sequence of consecutive commands and responses that are issued by a single reader and replied back by the tags in order to transmit the tag IDs to the reader. A sequence of consecutive interrogation rounds forms an interrogation session.

5.8.3.1 Enhanced ISO/IEC 18000-6C UHF

The time evolution of the algorithm is illustrated in Figs. 113 and 114 and described in the following.

1. Initially, the reader transmits a continuous-wave UHF signal (CW) to power up the tags in its maximum transmission range *RangeMax*. The maximum transmission range is application dependent and is limited by FCC/ETSI regulations.
2. As soon as the nodes are powered (i.e., $T_{pw} \approx 1500 \mu s$), the interrogation starts by following the standard ISO/IEC 18000-6C protocol. Together with the first *Query* command, the reader starts transmitting a sequence of UWB pulses and the tags respond by modulating the backscattered UWB signal using the *c* code.

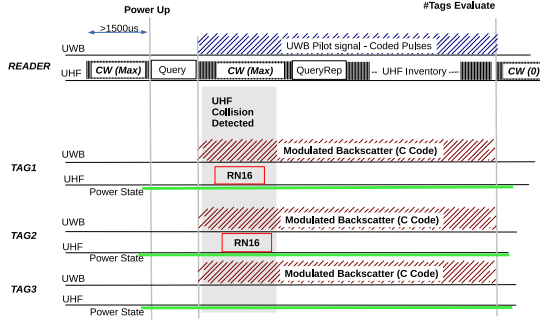


Figure 113: Standard UHF inventory in the first estimate of active tag number.

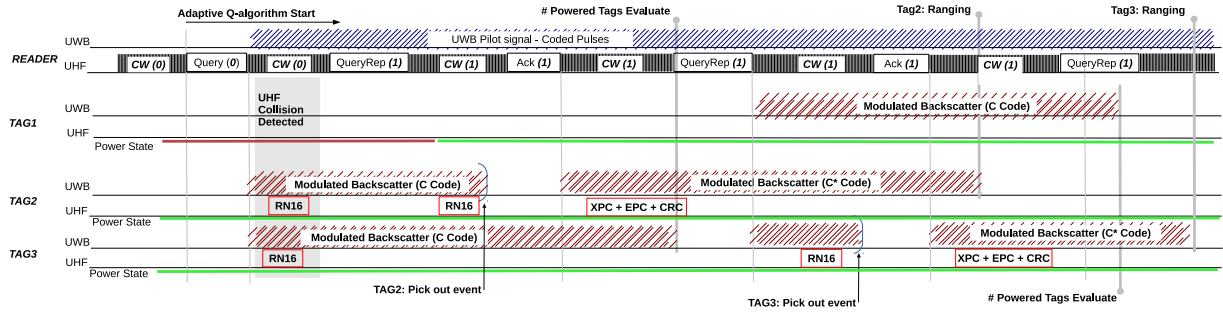


Figure 114: Example of UWB and UHF signal in the adaptive Q-algorithm, highlighting the UWB link tag use, the estimated number of tags (c code) and ranging (c^* code).

3. The reader interprets the received backscattered signal and estimates $Range0$ and $Range1$, namely the interrogation ranges that contain N_0 and $N_0 + N_1$ tags, respectively.
4. The reader then selects $Q = \lceil \log_2 N_0 \rceil$, where $\lceil \cdot \rceil$ denotes the nearest integer function, and sends the next *Query* command with sufficient power to interrogate tags in $Range0$.
5. Between consecutive *Query* commands, while interrogating tags in $Range0$, the reader continues the UWB ranging procedure by considering $Range1$ and $Range2$, which includes further N_2 tags. The UHF transmission power is set to reach also tags that are interrogated in the next *Query*. By doing so, those tags are already powered when receiving the *Query* command.
6. After N_1 tags have been identified, the reader increases the transmission power of the following *Query* command to reach tags in $Range1$ and, similarly, after $N_1 + N_2$ tags have been identified, the transmission power is increased to include $Range2$. In this way, the average number of activated tags in different stages of the interrogation is kept between $N_0 - N_i$ and N_0 . Notice that already identified tags stop responding to query commands and refrain from backscattering modulated UWB pulses in the same interrogation session.
7. The transmission range is increased every N_i successful interrogations until it reaches $RangeMax$ and the session ends when all tags have been identified.

We recall that the proposed mechanism is compliant with the ISO/IEC 18000-6C specifications for both the reader and the tag. The optimal choice of the parameters N_i is not straightforward. Every time the reader includes new tags, it has to issue a *Query* command instead of a shorter *QueryAdj* command. Therefore, if N_i is too small, the interrogation time and the energy consumption are negatively affected.

5.8.3.2 Enhanced Compressive Sensing Identification protocol

A novel tag identification protocol based on compressive sensing and UWB has been presented in [86], and it is briefly summarized in the following.

We consider a hybrid UWB/UHF tag architecture, where an UWB module helps the UHF-CS procedure for tags identification by reducing the time required for tags identification and by decreasing the complexity of the UHF-CS scheme. In particular, the tags are divided in groups, and both tags and groups are associated with codes for their identification. Specifically, group codes are communicated from tags to the reader in the UWB domain, while tag codes are sent in the UHF domain.

UHF signals are used for tags identification through a CS procedure, while UWB signals are exploited for fast groups identification and tags population estimation in order to reduce the UHF-CS search space size. Moreover, tag population and groups information are also useful to adapt the length of the tag ID codes. In this way, the UHF-CS procedure for tags identification becomes faster and simpler.

UHF-CS Model The tags' identification process is performed in the UHF domain and usually utilizes temporary IDs [87] [100]. Indeed, the globally unique ID, i.e., the one printed on the tag, is often long, while the temporary ID is shorter because the uniqueness needs to be kept only for the tags that want to transmit at the same time. As an example, the EPC Gen-2 standard [100] uses 16-bit temporary IDs during the identification phase [87] [100], so that the size of the temporary ID space is equal to $N = 2^{16}$.

Each tag chooses a temporary ID among N . A binary vector \mathbf{x} of size N is defined, where $x_j = 1$ if tag j is one of the K tags to be identified, and $x_j = 0$ otherwise. Therefore, $\|\mathbf{x}\|_0 = K$, since there are K non-zero elements in \mathbf{x} . We want to identify the elements j for which $x_j = 1$.

After receiving a start command, i.e., a Query from the reader, each tag for which $x_j = 1$ uses its ID as a seed in its hash function [88] to generate a $M \times 1$ pseudo random binary vector \mathbf{c}_j . $c_{ij} \in \{+1, -1\}$ are the elements of \mathbf{c}_j , where $i = 1, 2, \dots, M$, and M denotes the number of bits required for successful identification of the K tags. Specifically, the tags continue by generating a random bit and transmitting it until the reader verifies that a given length M has been reached. Then, the reader triggers the tags to stop transmitting, which can be done by simply stopping its RF signal that powers on the tags.

By gathering all vectors \mathbf{c}_j in the coding matrix $\mathbf{C} = [\mathbf{c}_1 \mathbf{c}_2 \dots \mathbf{c}_N]$ of size $M \times N$, where $M < N$, we have that the received measurement vector \mathbf{y} at the reader is given by

$$\mathbf{y}_{M \times 1} = \mathbf{C}_{M \times N} \mathbf{H}_{N \times N} \mathbf{x}_{N \times 1} = \mathbf{C}_{M \times N} \mathbf{z}_{N \times 1} \quad (52)$$

where $\mathbf{z} = \mathbf{Hx}$ and \mathbf{H} is the diagonal channel matrix, whose elements $\mathbf{H}_{jj} = h_j$ denote the complex channel coefficients for tag j . Indeed, since each tag transmits in a narrow band channel (640 kHz), its channel can be modeled as a single tap channel [100]. However, as described in Sec. 5.8.3.2, we analyse also the case of timing synchronization errors, for which \mathbf{H} considers the resulting inter-symbol interference (ISI).

The reader uses a CS decoding scheme to estimate the elements of vector \mathbf{z} . The estimation of \mathbf{z} is formulated as an optimization problem [101]:

$$\begin{aligned} \min_{\mathbf{z}} \quad & \|\mathbf{z}\|_1 \\ \text{subject to : } \quad & \mathbf{Cz} = \mathbf{y} \end{aligned} \quad (53)$$

where $\|\cdot\|_1$ is the l_1 norm. To guarantee stable recovery in the presence of noise, the number of measurements M , i. e. the length of the ID code associated to a tag, must obey:

$$M \geq \alpha K \log \left(\frac{N}{K} \right) \quad (54)$$

where α is a constant [101]. However, this condition imposes a prohibitive large value of M for $N = 2^{16}$, the whole ID search space. For this reason, it is needed to reduce the ID search space before employing CS techniques.

Even then, the 16-bit sequence of RN16 IDs are not used in CS-based protocols, since in general they will not fulfill the necessary condition (54) for successful recovery. This is the reason why M -length pseudo-random sequences are generated and transmitted in place of them.

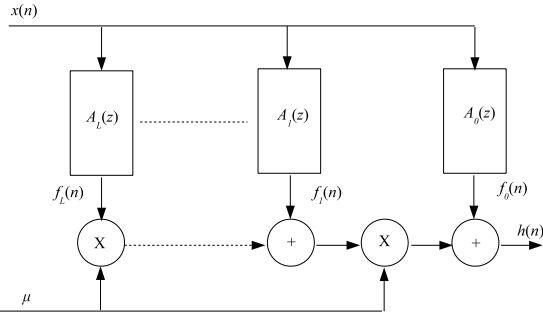


Figure 115: Farrow structure for the interpolation filter.

A drawback of CS-based protocols is that such pseudo-random sequences have to be received synchronously at the reader. Anyway, the tags can be synchronized by exploiting the reader's query that trigger the tags, but the jitter in detecting the reader's signal can lead to initial offsets.

In the following Sec. 5.8.3.2, in order to evaluate the effect of such offsets on the UHF-CS procedure, we model the timing offset as an ISI at time slot level among the backscattered signals from the different tags. The ISI effects results in a non-diagonal channel matrix \mathbf{H} (see Sec. 5.8.3.2).

Note that we analyse the synchronization issue only for UHF signals, since it is negligible for UWB signals in the way they are employed in the presented solution, as specified in Sec. 5.8.3.2.

Timing synchronization error model In this section we model the timing synchronization error in the UHF domain. The Farrow structure (see Fig. 115) of the interpolation filter consists of $L + 1$ parallel FIR branch components with fixed coefficients having transfer functions $C_l(z)$, for $l = 0, 1, \dots, L$, and only one variable parameter μ . The parameter L is the degree of the polynomial while μ represents the fractional delay timing error correction. The impulse response of the interpolator in each sampling time interval $T_s = \frac{T}{2}$, where T is the symbol time, is:

$$p(iT) = p[(k + \mu)T_s] = \sum_{l=0}^L a_l(k)\mu^l \quad (55)$$

The output of the Farrow scheme is:

$$h(n) = \sum_{k=-N/2}^{N/2-1} x(n-k)p[(k + \mu)T_s] = \sum_{l=0}^L f_l(n)\mu^l \quad (56)$$

where:

$$f_l(n) = \sum_{k=-N/2}^{N/2-1} x(n-k)a_l(k); \quad (57)$$

and N , the Farrow branch filter length, is equal to the filter order plus one. $h(i)$ is the element of the vector \mathbf{h} and \mathbf{H} is the convolution matrix of \mathbf{h} , which accounts for the ISI due to timing synchronization error, and it is used in (52) when accounting for timing synchronization errors, instead of the diagonal matrix.

The basic idea of this structure is that the outputs $h(i)$ form a polynomial approximation for the continuous-time signal $x(t)$ at time instants $iT = (n + \mu T_s)$. The obvious advantage, in terms of hardware implementation complexity, is that the filter coefficients are constant and the output time sampling is only controlled by the parameter μ [102].

The design of Farrow interpolators can be done in several ways and traditionally it is based on Lagrange polynomials. In this work we consider the Farrow structure for the Lagrange interpolator polynomials, as reported in [103], which satisfies the following condition:

$$\mathbf{V}\mathbf{a} = \mathbf{w} \quad (58)$$

where:

$$\begin{aligned}\mathbf{a} &= [A_0(z) \ A_1(z) \ \cdots \ A_L(z)]^T \\ \mathbf{w} &= [1 \ w^{-1} \ \cdots \ w^{-L}]^T\end{aligned}\tag{59}$$

and \mathbf{V} is the Vandermonde matrix:

$$\mathbf{V} = \begin{pmatrix} 0^0 & 0^1 & \cdots & 0^L \\ 1^0 & 1^1 & \cdots & 1^L \\ \vdots & \vdots & \ddots & \vdots \\ L^0 & L^1 & \cdots & L^L \end{pmatrix}\tag{60}$$

The solution of (58) provides a filter structure in which the fractional delay $\mu \in [0, 1]$ and a constant phase delay with respect to the filter order.

A more efficient construction is suggested in [104], with a new parameter range equal to $[-0.5, 0.5]$. This can be pursued by employing the matrix transformation \mathbf{T} :

$$T_{n,m} = \begin{cases} \text{round}(\frac{L}{2})^{n-m} \binom{n}{m} & \text{for } n \geq m \\ 0 & \text{for } n < m \end{cases}\tag{61}$$

where $n, m = 0, 1, \dots, L$ and the new filter is obtained by replacing the solution of (58) with:

$$\mathbf{a} = \mathbf{T} \mathbf{V}^{-1} \mathbf{w}\tag{62}$$

UWB Model While we use UHF signal to identify the tags through a CS procedure, we exploit a UWB signal to reduce the complexity of such UHF-CS algorithm [86].

Without loss of generality, we organize all the N tags in N_g groups with size s_g according to the globally unique ID number printed on each tag.

Considering the UWB domain, we use UWB codes to identify the groups the tags belong to. Thus, according to the model in Sec. 5.8.2.2, the reader receives the UWB backscattered signal $r(t)$ expressed in (50), whose k -th contribution defined in (51) is replaced with:

$$r^k(t) = \sum_{m=-\infty}^{+\infty} \sum_{n=N_x}^{N_{pc}-N_x-1} d_n d_m^g \omega^k(t - nT_f - mT_c)\tag{63}$$

where d_m^g is the group's code the k -th tag belongs to, which replaces the code d_m^k in (51).

UWB&UHF-CS algorithm first step: estimating the number K of tags and the groups they belong to The time evolution of the algorithm is described in the following. Initially, the reader transmits a continuous-wave UHF signal (CW) to power up the tags in its transmission range.

As soon as the nodes are powered (i.e., $T_{pw} - 1500 \mu s$), the interrogation starts. Note that differently from the standard ISO/IEC 18000-6C protocol, the CS procedure does not need re-transmission when a collision occurs. In particular, together with the Query command, the reader starts transmitting a sequence of UWB pulses. The K tags to be identified, i.e., the ones in the reader's range, respond by modulating the backscattered UWB signal using the d_m^g codes.

The reader interprets the received backscattered signal and estimates both the tags' population K and the identification of the groups they belong to according to the received UWB codes d_m^g . The reader despreads the received UWB backscattering signal $r(t)$, with reader code d_n and UWB group tag codes d_m^g according to (50) and (63), and identifies the empty/busy groups.

Moreover, estimating the received energy for each UWB group code gives an estimate of the number K of tags to be identified, even in the presence of multipath fading effects, since we just need a rough

estimation of K itself. Such estimate is used to adapt the tag code length in the UHF-CS algorithm described in the following.

We here do not consider the synchronization issue, since synchronization at chip level for UWB group codes identification is not stringent because the reader's receiver has to compute only the correlation with known groups codes to detect the groups the tags belong to; therefore, it is not necessary to recover data where the synchronization would be problematic.

UWB&UHF-CS algorithm second step: reducing the scale of Compressive Sensing In this section we describe the CS procedure, which is performed in the UHF domain.

Since CS moves the computational complexity from coding to decoding, a CS benefit is that the RFID tags can be quite low-cost. However, the reader must handle more computing work. The decoding complexity of CS is $O(N \times \log(N/K))$ [101], which is really high when the number N of all the RFID tags is huge. On this purpose, the reader must reduce the scale of suspected RFID tags.

UWB information is here exploited to reduce the search space size of the UHF-CS procedure. Specifically, the reader interprets the received backscattered signal and estimates the groups UWB codes d_m^g . Only the tags IDs associated with that group codes d_m^g will remain in the search space, the other ones will be discarded, thus reducing the number of columns of the matrix \mathbf{C} in (52). Note that tags' codes forming matrix \mathbf{C} are communicated in the UHF domain during the CS procedure for tags identification.

Let \mathbf{C}' be a reduced version of the matrix \mathbf{C} that keeps only the columns corresponding to the remaining $N_g^* s_g$ possible temporary IDs, where N_g^* is the number of the groups with tags to be identified, s_g is size of the group, with $N_g^* \leq K$. \mathbf{x}' and \mathbf{H}' are the similarly reduced forms of \mathbf{x} and \mathbf{H} expressed in (52). In this way, the reader only needs to regenerate \mathbf{C}' , as opposed to \mathbf{C} .

UWB&UHF-CS algorithm third step: tags identification through CS decoding scheme Now that we have reduced the scale of CS problem to recovering K temporary IDs out of only $K s_g$ possible IDs at most, and according to the notation in Sec. 5.8.3.2, the system to solve in the UHF domain becomes:

$$\mathbf{y} = \mathbf{C}' \mathbf{H}' \mathbf{x}' = \mathbf{C}' \mathbf{z}' \quad (64)$$

To decode, the reader uses CS to estimate the elements of vector \mathbf{z}' . Objective:

$$\min_{\mathbf{z}'} \|\mathbf{z}'\|_1 \quad (65)$$

Subject to:

$$\mathbf{C}' \mathbf{z}' = \mathbf{y} \quad (66)$$

The space of the problem is now N' as opposed to N , with $N' < N$ and $N' \leq N_g^* s_g$, where N_g^* is the number of groups containing the K tags to be identified, and the tag code length can be reduced to

$$M \geq \beta K \log(s_g) \quad (67)$$

where β is a constant [86].

5.8.4 Multi-Reader Scenario

Large tags deployment, mobility and real-time requirements are some peculiar aspects for a wide set of RFID application domains. Unfortunately, readers have limited energization and interrogation range, and consequently coverage and identification performance may not be met by a single interrogator. The use of multiple readers, networked in some way, has been proposed as a viable and effective approach to address leakages and drawbacks of single reader systems.

However, multi-reader MAC protocols design is challenging given that different kinds of collision problems arise. Indeed, unlike the single reader scenario, in which the *tag-tag collisions* can be handled by classical anti-collision schemes, in multi-readers systems interference between readers lead to different

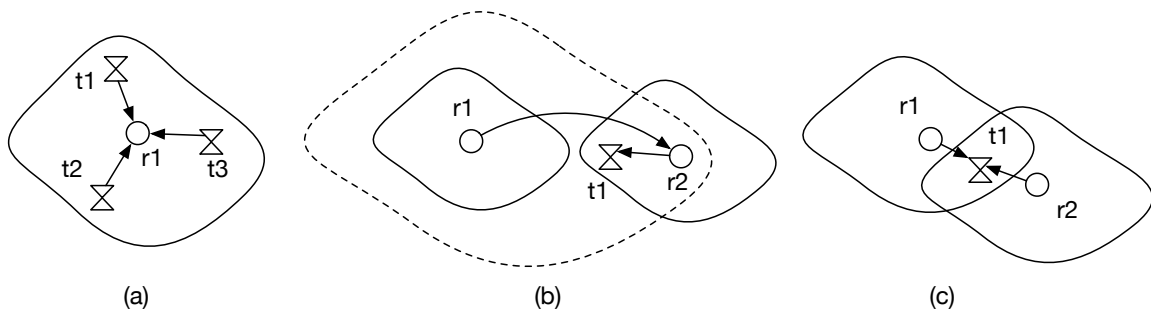


Figure 116: Collisions in multiple-reader RFID systems. (a) Tag-Tag collision. (b) Reader-Tag collision. (c) Reader-Reader collision.

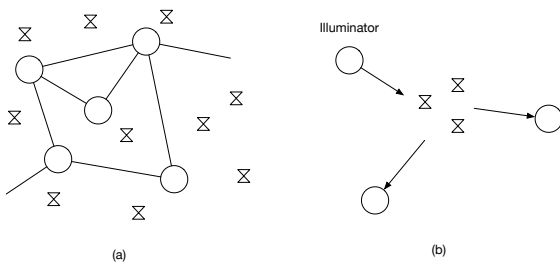


Figure 117: Readers Cooperation. (a) General readers network. (b) Readers cooperation for ranging and localization.

kinds of collisions known as *reader collisions*. In a reader collision event, interference is generated by a reader and the interfered entity can be either a reader or a tag. Thus, we can distinguish two kinds of reader collision (Fig. 116): *reader-tag collision* and *reader-reader collision*. A *reader-tag collision* occurs when a reader is in the interference region of another reader. For example, referring to Fig. 116-(b), the signal from r_1 may affect t_1 's response to reader r_2 , thus preventing correct tag identification. This kind of collision can be avoided by planning frequency channel assignment to neighboring readers, or by carefully scheduling reader activation in the time domain. Similarly, a *reader-reader collision* event takes place when a tag is in the overlapping interrogation region of two active readers. For example in Fig. 116-(c), queries from r_1 and r_2 may collide at tag t_1 , preventing t_1 to correctly respond to any reader. Although readers are still able to read tags in their interrogation regions, the reading process may result in wrong identification of those tags within the overlapping areas.

Readers cooperation can be exploited to mitigate the described problems.

The general multi-reader scenario is depicted in Fig. 117-(a), where a set of networked readers scan a certain region of interest. In this case, readers can exchange ranging and population information in order to perform efficient tag identification. For instance, readers can adjust interrogation ranges in order to mitigate interference and improve identification performance.

A particular case of the general scenario is depicted in Fig. 117-(b), where one reader acts as an "illuminator" (i.e., provides tag energization and synchronization) and the other ones are enabled for collecting UWB tags' responses for ranging and localization purposes.

In what follows we refer to the general scenario and consider the conditions under which it can be reduced to the particular case of Fig. 117-(b). We further provide the guidelines on how to extend the enhanced *Q*-Algorithm to the multi-reader scenario based on the system architecture described in Sec. 5.8.2 and exploiting reader cooperation. Finally, we extend the CS approach described in Sec. 5.8.3.2 to multi-reader systems.

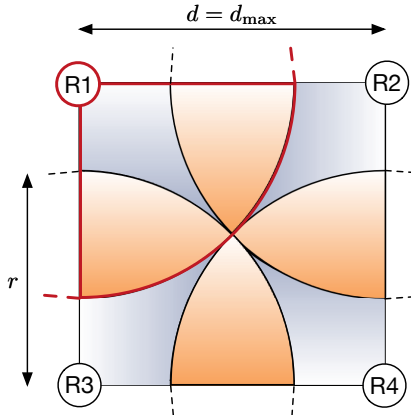


Figure 118: Localization regime: limit case

5.8.4.1 Enhanced Q-Algorithm

We consider the readers' network depicted in Fig. 117 that is structured as a Wireless Sensor Network (WSN) relaying on the IEEE 802.15.4a protocol. Without loss of generality, we focus on a small portion of the network, that consists of four readers operating under the following main assumptions: 1)

1. Nomadic environment: when not operational, one or more readers could change their position in the network;
2. Antenna model: each reader is equipped with a steerable antenna. We consider an ideal flat-top antenna model [105] with main lobe beam-width θ , and no secondary lobes. The antenna beam-width must be large enough to cover the interrogation region of interest (e.g., $\theta \geq 90^\circ$ to guarantee coverage for a square interrogation region);
3. the UHF coverage range r_{UHF} is equal to the UWB coverage range r_{UWB} (i.e., $r_{\text{UHF}}=r_{\text{UWB}}=r$). The coverage range r depends on the power emission limitation of both UHF and UWB specifications. In the UWB case, the range also depends on the processing gain of the selected codes [106].

The first assumption implies that, in general, readers in the network are not aware about the presence and the position of other readers. Consequently we define a *Reader Discovery Phase*. During this phase, neighbor readers identify themselves by exchanging information to determine their relative position in the network. At this stage readers also exchange information for negotiating their UWB codes for backscattering communication operation that will be used to perform multiple access under Code Division Multiple Access (CDMA) technique. The information exchange during the discovery phase completely relies on UWB communication. For instance, to achieve very fast reader communication, the discovery phase can be implemented by exploiting the IEEE 802.15.4a protocol features.

Note that readers should be able to direct their antenna beams towards the desired direction in order to determine the scanning area to be covered. Techniques to achieve this feature are beyond the scope of our work. In what follows we assume a static scenario where the discovery phase has been successfully completed and all the readers have their antenna beams pointed toward the correct direction. To avoid the presence of uncovered interrogation areas, we further assume a square total interrogation region with maximum dimension $d_{\text{max}}=2r/\sqrt{2}$ and we suppose that the tag population is confined within this area.

Once the reader network has been established, two possible operating regimes can be distinguished, namely the *Tag Identification Regime* and the *Tag Localization Regime*. The particular operating regime of the multi-reader system depends on the ratio between the readers coverage radius r and the interrogation area dimension d . The two operative scenario are described in details in the following.

Tag Identification Regime When the distance between adjacent readers is exactly equal to $d=d_{\text{max}}$ the system is unable to localize tags in the space. This is due to the fact that no point within the inter-

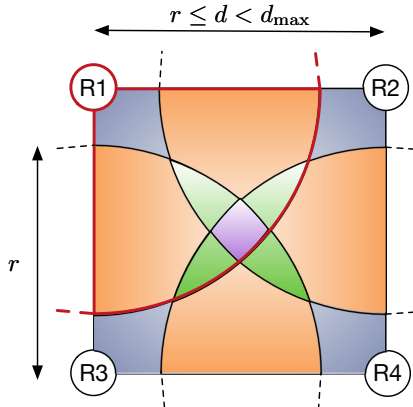


Figure 119: Localization regime: general case

rogation area can be covered by at least three readers simultaneously (Fig. 118). Thus, only ranging and identification are possible in this particular scenario.

The identification procedure for this case is performed by exploiting the enhanced Q -algorithm features described in Section 5.8.3.1. In particular, each reader separately runs the enhanced identification protocol scanning its own interrogation region. Observe that, to adapt the enhanced Q -algorithm to the multi-reader scenario in the Spatial Division Multiple Access (SDMA) hypothesis, readers need to cooperate in order to choose the proper power sweep step during each phase of the algorithm. In particular, each reader identifies tags within Range_i and simultaneously scan Range_{i+1} for ranging estimation. If uncoordinated, this procedure may lead to undesired overlapping scanning areas. Consequently, after each algorithm iteration, readers flood the gathered information over the readers' network, exploiting 802.15.4a underlying structure. Based on this knowledge, readers can adapt the protocol parameters when performing the next power sweep iteration trying to avoid overlapping among scanning areas.

The time required for each reader to complete the current algorithm step depends on the chosen Q , which in turn depends on the number of tags involved. Based on ranging information, readers can set their interrogation ranges such that the considered number of tags is about the same for each reader. Thus, all the readers terminate the power sweep step at the same time plus a small time offset and it is possible to exchange information through the readers' network without the need of additional UWB transceivers in the proposed readers' architecture. If at least one reader terminates its algorithm iteration later with respect to the other, the described procedure may become inefficient. The delayed reader will provide acquired information later, thus the current adaptation step has to be done with missing information. A statistical analysis of the step duration, conditioned to the number of tags involved in the step, is beyond the scope of our work.

Note that, if the readers are well coordinated, the described procedure effectively mitigate the *reader-reader* collision problem by decoupling the scanning area explored by each reader. Indeed, if readers properly coordinate power control during the interrogation phase, the number of overlapping areas can be drastically reduced, thus cutting down the reader-to-reader interference. The problem of finding an optimal power sweep policy can be solved by exploiting readers' cooperation. The derivation of the optimal power control policy is beyond the scope of our work and will be presented in future analysis.

We stress the fact that, assuming that an optimal power control policy exists, the performance of the multi-reader system strictly depends on the performance of a single-reader system in terms of tag speed identification and query success rate. Indeed, if the interrogation areas decoupling is guaranteed, the multi-reader scenario can be analyzed as a superimposition of four independent single reader systems. Furthermore, the reader-to-tag synchronization scheme proposed in [107] can be applied in the multi-reader scenario.

We remark that performance can be further improved when $r \leq d < d_{\max}$. Indeed, in this scenario

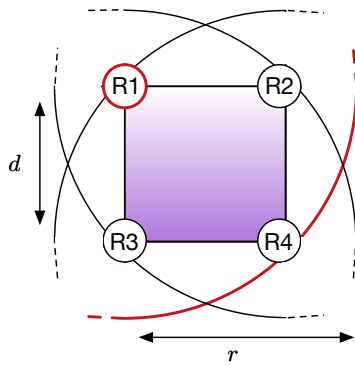


Figure 120: Localization regime

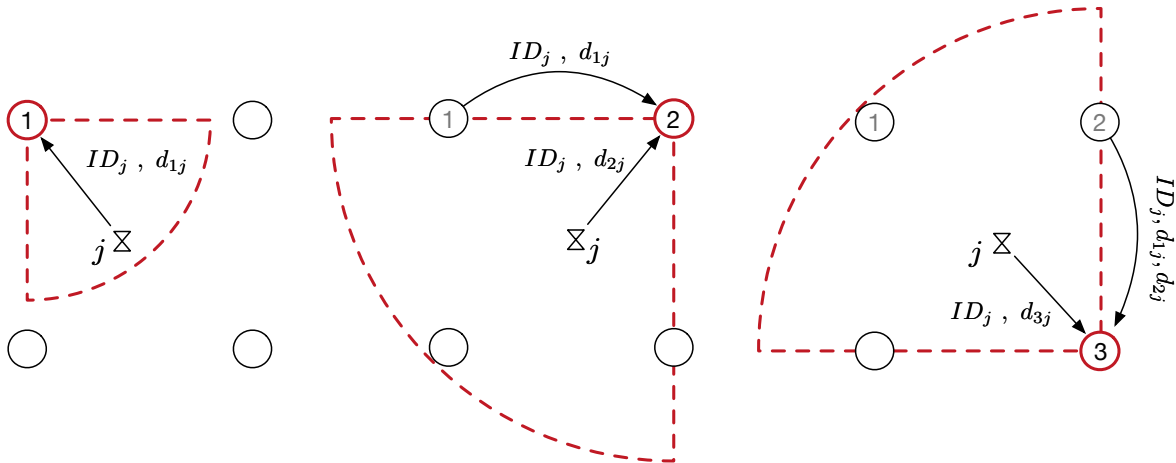


Figure 121: Token ring synchronization policy

the system is able to estimate tags' position within certain regions (Fig. 119). Consequently, localization information can be opportunistically used to refine the decoupling and the power sweep operations during the inventory phase.

Finally we observe that the *reader-tag* interference problem is not completely solved by the described procedure even if coordinated power sweep may mitigate it. However, if we again assume the existence of an optimal decoupling and power sweep scheme, reader-tag collisions can be easily solved by allowing readers to operate on different frequency channels.

Tag Localization Regime When the distance between readers is $d < r$, only one reader is sufficient for identification purposes. Indeed, the coverage range r is large enough to energize and interrogate the whole area of interest and relaying on only one reader referred to as “illuminator” (Fig. 120). The presence of other readers can be exploited to accurately localize the tags in the space. Readers that only give support for localization are denoted by “anchors”.

The identification performance are the same of the enhanced *Q*-Algorithm described in Sec. 5.8.3, and the focus for this scenario moves on tag spatial distribution estimation. Herein we consider a *mono-static* approach for tags localization. In particular, after the tags are energized, each reader acquires ranging information by investing tags with an UWB signal and waiting for the backscattered reply. The obtained information are exchanged through the readers’ network, so that the readers have at least three distance measurements for each tag. Consequently tags position can be estimated by means of some localization algorithm (i.e., trilateration-based positioning algorithms [108]).

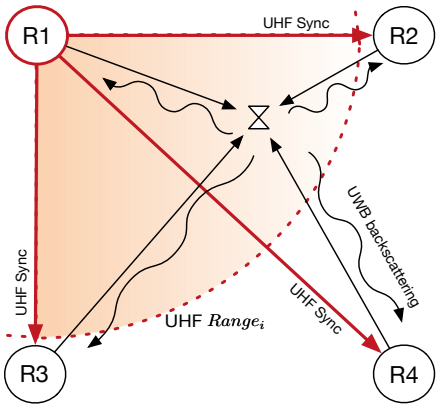


Figure 122: UHF/UWB signaling synchronization policy and UWB Backscattering in mono-static scenario

We remark that the described approach requires synchronization between readers. Different synchronization strategies are possible. In the following some alternatives for synchronization policies are described.

Token Ring: The reader network is organized in a token ring fashion and all the readers act as illuminators in deferred time. In particular, one reader (e.g., R1) runs the enhanced Q -Algorithm, thus identifying all the tags and collecting their ranging information. Once the procedure terminates, the reader transmits gathered information (i.e., tags' IDs and relative ranging information) and a token message to the next reader in the ring. The reader that receives the token illuminates the whole interrogation region, selecting the already identified tags. For each tag, the reader acquires ranging information and passes the token to the subsequent reader, also providing its ranging measurements. The procedure is repeated until the token returns to the first illuminator. At this point each reader is provided with at least three ranging measurements for each tag, thus enabling their localization. An example of the described procedure is illustrated in Fig. 121, where only one tag is considered. In each step, the active reader i sends the ID of the identified tag ID_j and its relative distance from the identified tag d_{ij} .

UHF signaling: In this case only one reader acts as illuminator. Again the illuminator initiates a Q -Algorithm session. The UHF signal sent by the illuminator for reader-tag synchronization has also the role of synchronization event for the network. In particular, the anchors listen to this signal and when they receive it, they simultaneously start a UWB session for gathering ranging information. Once ranging informations are available, readers flood the measurements through the network and the illuminator starts another Q -Algorithm iteration. Note that, under this synchronization policy, all the readers in the network must be able to listen to the illuminator UHF command [109]. The illustration of a single Q -Algorithm step operating under *UHF signaling* is shown in Fig. 122.

UWB signaling: This approach is similar to the previous one. Differently from the UHF signaling, synchronization is achieved by means of an UWB preamble-like signal, thus enabling a finer synchronization. The preamble violation (i.e., the end of the preamble-like signal) indicates the start of the backscattering UWB operations (Fig. 122).

Note that with either UHF or UWB signaling, readers synchronization is obtained during the system operational phase, then better performance can be obtained if compared with the *Token Ring* approach that defers readers activation over time in a TDMA fashion.

Finally, the tag localization can be also performed following a *multi-static* approach. Despite this requires more complex synchronization policies, it may result in energy consumption reduction, but localization accuracy may be lower than in the mono-static approach. Herein we do not consider the multi-static case. The interested reader is referred to [106] for a discussion on passive UWB RFID systems for tags localization.

5.8.4.2 CS for Multi-Reader Systems

As described before, the tag collision problem in single reader scenario can be solved by using compressed sensing techniques, which tolerate collisions differently from FSA protocols. However, CS procedures shift the complexity from the protocol to the decoding scheme at the reader and, in case of reader-reader collision, the tag would not understand the colliding queries. The CS procedure can not be applied to the tag receiver, since it is able to perform only simple tasks.

We propose to implement a synchronized protocol where all readers operate simultaneously on the same frequency channel using the same query, thus saving time and spectrum usage. The solution of using synchronized multiple readers in a large area could be equivalent to use a single reader with a larger power, but the restriction in the maximum power allowed to the readers limits their interrogation zones, requiring for multiple readers to cover the area [110].

A similar approach has been applied to FSA tag anti-collision problem in [110]. However, the issues in the proposed CS based protocol are different from the ones in FSA approach when using synchronized multiple readers. In particular, the open issues in a CS based solution is the choice of the length M of random tag codes used for their identification, which has to satisfy specific CS requirement as expressed in (67).

Moving into details, the protocol consists in all readers sending the same sequence of bits in the UHF domain, i.e. the same query, to the tags. Assuming coordination among the readers, the queries are sent at the same time so that they will not cause collisions at the tags. Indeed, since the queries are made up of the same bits, the interference from close readers do not produce collisions at tag receivers, and the received signal level at the tags remains high or low depending on whether the bit transmitted by the readers is a "1" or a "0".

If a tag is in the range of multiple readers, when receiving the common query, it will send only one response with its identification code (UHF domain). Such code will be received by the readers in the overlapping regions in the same slots since the readers' queries are synchronized in time.

As said before, the tags identification codes are characterized by the length M . We assume that all tags will have the same ID length M . In this way, by properly choosing the seed for generating the tag ID code and the same length M of the codes, there will be a unique tag ID code also for tags that are in overlapping reader regions.

$$M \geq \beta K_{max} \log(s_g) \geq \beta K_r \log(s_g) \quad (68)$$

In (68) the maximum number of tags K_{max} in a reader region needs to be calculated for the multi-readers scenario. Also in this case UWB information will be used to enhance the proposed CS based protocol. Indeed, the estimation of the maximum number of tags in reader region, available through UWB information, will allow a common definition of the length M of tag ID codes according to (68). M corresponds to the number of measurements needed to identify the tags in all readers regions, that is the time spent for the identification process in this scenario. Equation (68) assures to have the same performance as in the single reader scenario.

The seed of the random function for tag ID generation is its identification number. In this way, we assure a unique value for the seed of the specific tag, independently from the corresponding index of a certain coding matrix at the reader. Indeed, a tag in overlapping readers' regions will have a different index for each coding matrix of the readers, and a lookup table will be used to assure the correspondence of the seed.

5.8.5 Numerical Results and Discussions

5.8.5.1 Performance of the enhanced Q-algorithm

In this section, we report simulation results of the enhanced ISO/IEC 18000-6C against the standard protocol in terms of probability of successful identification in a single query, here denoted as query success rate, and energy consumption at the end of an interrogation session. The energy consumption is calculated at the reader, by considering the transmission power levels in the different stages for UHF and

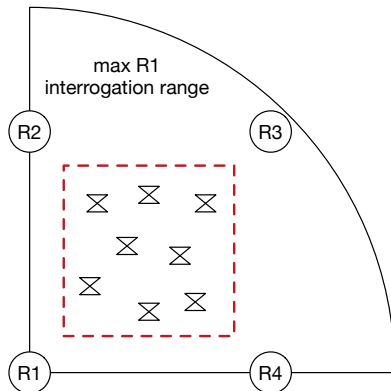


Figure 123: Reference scenario considered in simulation

UWB channels. Both the query success rate and the energy consumption depend on protocol specifications as well as the number of tags, the distance between the tag and the reader, environment, etc. In this validation we assume static channel conditions and zero bit-error rate. Moreover, the effects of antenna polarization on the communication range of the reader are not included. The tag population is in the range $N = [10 - 90]$ tags and it is uniformly deployed in a 2D area as in Fig. 123. We assume that the *tag localization regime* condition described in section 5.8.4.1 are met, thus we can evaluate interrogation performance as in the single-reader scenario. Localization performance analysis is beyond the scope of our work and is not reported here. The UHF air interface parameters are set to default specifications for tag modulation rate of 125 KHz. The evaluation is based on various levels of accuracy for the UWB ranging operation. The accuracy is measured in terms of maximum estimation error on the interrogation ranges (i.e., on the number of tags actually present in each range). The range accuracy of 1 cm can be achieved with very performing UWB modules, while 30 cm can be considered a fairly conservative value. As shown in Fig. 124, the enhanced mechanism achieves a query success rate of 0.42 with 25% gain with respect to the standard ISO/IEC 18000-6C for the case with high range accuracy. The gain is slightly reduced (20%) in the case of low ranging accuracy. The energy consumption (see Fig. 125) is 20% lower when using the enhanced mechanism with respect to the standard ISO/IEC 18000-6C thanks both to the faster identification speed and to the use of lower transmission power level. As an interesting note, there is no relevant dependency of the energy consumption on the range accuracy.

5.8.5.2 Performance of the UWB&UHF-CS algorithm:

UWB&UHF-CS algorithm in Single-reader scenario We use the same simulation set up as in [87] [88] to compare the proposed UWB&UHF-CS solution with the FSA system used in ISO/IEC 18000-6C standard and with BUZZ protocol [87], a CS-based scheme that uses a TDMA procedure for groups identification and search space reduction. A variable number K of tags is considered, i.e., 4, 8, 12 and 16, out of a total number N of 8000 tags. We consider $N_g = 160$ groups with a group size $s_g = 50$ as in [87] [88].

FSA uses 16-bit temporary IDs for the RFID tags and a re-transmission scheme in case a collision occurs. For the FSA algorithm we use the same setup parameters as in [88].

Given $N_g = 160$ groups, each containing 50 tags, the TDMA scheme of the BUZZ system takes 160 time slots only to reduce the scale of suspected tags. On the contrary, the proposed system performs the reducing phase just in one time slot by exploiting UWB information.

A comparison among the proposed scheme and the existing FSA and BUZZ approaches is presented in Fig. 126, showing the results in terms of time consumption (Fig. 126(a)) and probability of identifying

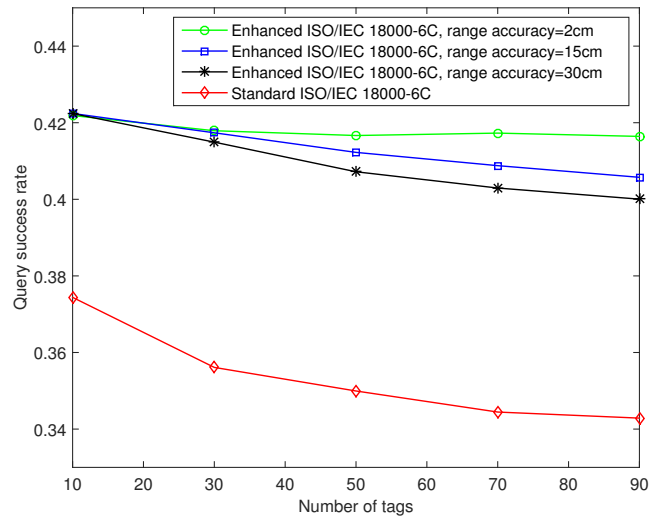


Figure 124: Query success rate (QSR) as a function of number of tags

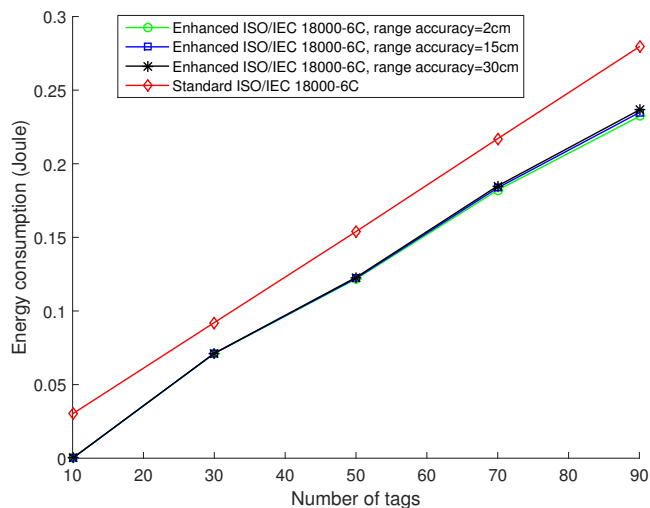
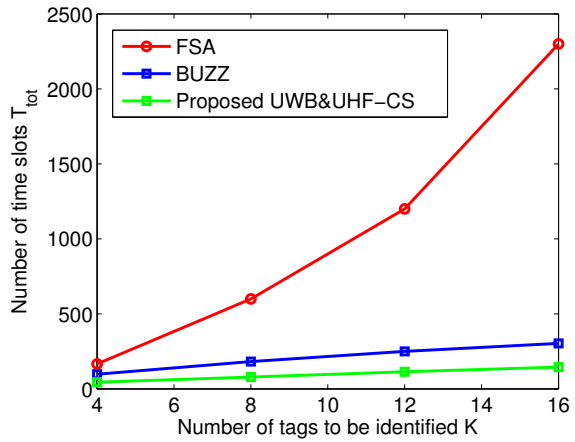
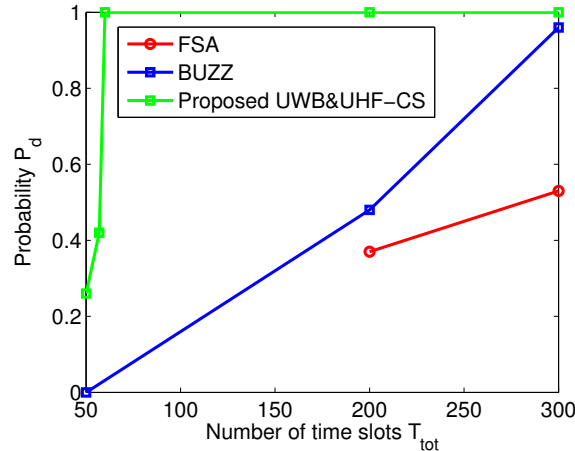


Figure 125: Energy consumption as a function of number of tags



(a) Time consumption



(b) Probability of identifying the K tags

Figure 126: Single reader scenario: Comparison among the proposed UWB&UHF-CS, FSA, and BUZZ

the K tags (Fig. 126(b)).

Fig. 126(a) shows that, when the number K of the tags to be identified increases, all the three schemes spend more and more time to identify the K tags. By using compressive sensing, both the BUZZ and the proposed UWB&UHF-CS scheme reach the goal of efficiently speeding up the identification, compared to the standard FSA. In addition, the proposed scheme has a higher efficiency than BUZZ because of the reduction improvement based on UWB information.

Fig. 126(b) shows the probability P_d of identifying the K tags. P_d is defined as $1 - P_{err}$, where P_{err} accounts for the miss detection of tags among the K ones to be identified. Fig. 126(b) refers to the case of $K = 12$ tags and shows that the proposed UWB&UHF-CS scheme needs less time slots than the other solutions to achieve a good probability of success (higher than 0.9). Finally, it is easy to note from the figure that the slope of the two CS-based approaches (UWB&UHF-CS and BUZZ) is higher than FSA solution, thus proving their effectiveness.

The following Fig. 127 refers to the proposed scheme, where the probability P_d of identifying the K tags is evaluated by varying K . Fig. 127 confirms that, as soon as the critical number of time slots is reached, the proposed solution is able to identify all the K tags with high probability.

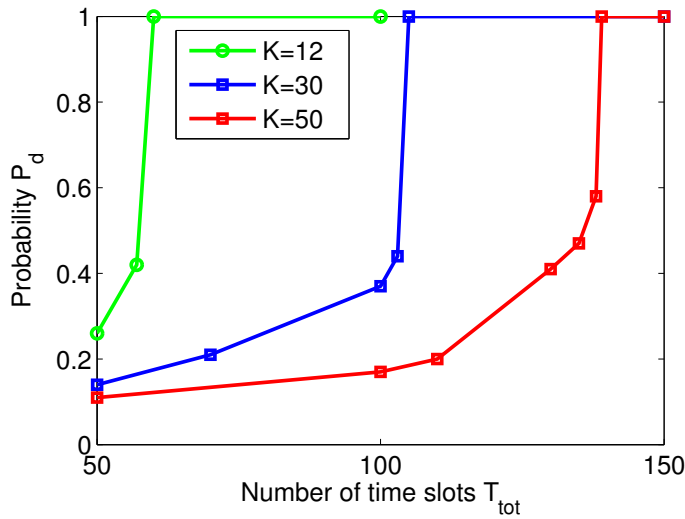


Figure 127: Proposed UWB&UHF-CS in single reader scenario: Probability of identifying the K tags

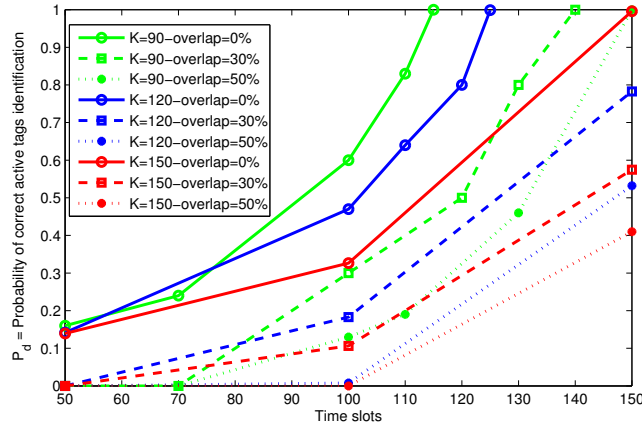


Figure 128: Proposed UWB&UHF-CS in multireader scenario: Probability of correct tags identification varying the number K of tags and the percentage of the overlapping region between readers.

UWB&UHF-CS algorithm in Multi-reader scenario: We first consider a total number of 8000 tags and then apply the scale reduction procedure for each reader, as described in Sec. 5.8.3.2. We assume that the number of tags are equally distributed among the readers. In the simulation we did not keep fixed the length of the code M as expressed in (68), but we let M to vary while maintaining the same value for all the tags. M is equal to the time slot required for tags identification and varies between 50 and 150 in Fig. 128 and between 50 and 200 in Fig. 129.

Fig. 128 shows the probability of tags identification in a multi-reader scenario. By increasing the number K of tags to be identified and the percentage of the overlapping region, the performance degrades since the sparsity degree changes. Indeed, for a given value of M , that is equal to the number of time slots required for the procedure, when increasing the overlapping region, the number of tags to be identified per reader increases, so the number of elements different from zero increases. On the contrary, if we fixed the value of M according to the reader that covers the maximum number of tags, as expressed in (68), we assure to have the same performance of the single reader scenario at the cost of increasing the number of time slots required for tags identification.

Fig. 129 shows the probability of tags' identification P_d when varying the the percentage of timing offset between the tags and the reader in a multi-reader scenario. We assume that the readers are syn-

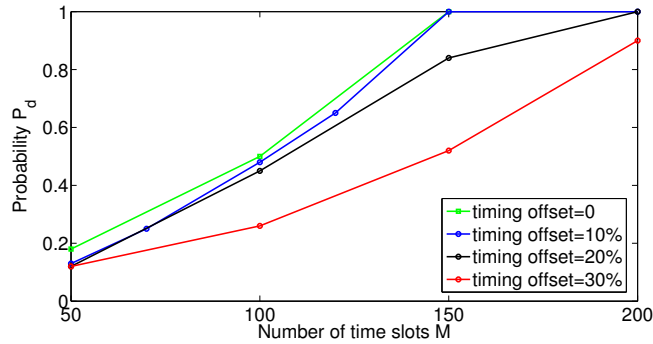


Figure 129: Proposed UWB&UHF-CS in multireader scenario: Probability of tags identification P_d varying the the percentage of timing offset between the tags and the reader.

chronized since they may use a dedicated channel for synchronization, while the tags may have an initial offset due to the jitter in detecting the reader's signal, which is used as a trigger to synchronize the tags. In Fig. 129 the offset varies between 0 and 30% of the bit length. The figure shows that the impact of the offset on the performance is negligible for offset values in the range 0 - 20%. Although there is a degradation when increasing the offset, the probability of detection is good at the cost of increasing the tag code length, i.e. the time required for tag identification.

We proposed two novel algorithms that efficiently exploit the integration of UHF and UWB radio modules to improve the performance of UHF RFID identification protocols in multi-reader, multi-tag systems. We first considered an enhanced *Q*-Algorithm for the ISO/IEC 18000-6C UHF standard that relies on UWB-aided tags inventory. In particular, UWB ranging capabilities are exploited for tuning MAC layer parameters and interrogation power in a readers' cooperation perspective. We showed how the considered solution outperforms the classic *Q*-Algorithm both in terms of query success rate and energy consumption, achieving a success rate gain of 25% and a reduction of 20% in energy expenditure. A compressive sensing based algorithm is also developed and analyzed in terms of correct tags identification probability. Simulation showed that the CS approach results in very fast tag identification and high robustness to readers' interference problems and time synchronization errors among tags and readers.

6 DISSEMINATION ACTIVITY

In this section the dissemination activity carried out and planned by the research units is reported.

6.1 University of Bologna

The following papers have been published or accepted for publication:

- M. Dini, A. Romani, M. Filippi, and M. Tartagni, " A Nanopower Synchronous Charge Extractor IC for Low-Voltage Piezoelectric Energy Harvesting With Residual Charge Inversion," IEEE Trans. Power Electron., vol. 31, no. 2, pp. 1263–1274, Feb. 2016.
- D. Masotti, A. Costanzo, P. Rocca, A. Massa, " The importance of nonlinear/electromagnetic co-simulation on time-modulated array synthesis", submitted to 2016 IEEE International Symposium on Antennas and Propagation & USNC/URSI National Radio Science Meeting (invited paper)
- S. Kenny, G. Goussetis, S.K. Podilchak, A. Costanzo, M. Del Prete, D. Masotti, P. Nicole, " Frequency Scanning Antenna for Wireless Power Transmission", submitted to 2016 IEEE International Symposium on Antennas and Propagation & USNC/URSI National Radio Science Meetin
- A. Costanzo, D. Masotti, " How to Get the Most from Far-field Wireless Power Transfer", accepted for publication on IEEE Microwave Magazine
- A. Pacini, R. Trevisan, F. Mastri, A. Costanzo, D. Masotti, "Geometry Optimization of Sliding Inductive Links for Position-independent Wireless Power Transfer" accepted for publication at 2016 IEEE MTT-S International Microwave Symposium (IMS)
- M. Del Prete, A. Costanzo, D. Masotti, M. Magno, L. Benini, " Experimental Analysis of Power Optimized Waveforms for Enhancing Wake-up Radio Sensitivity", accepted for publications at 2016 IEEE MTT-S International Microwave Symposium (IMS)
- A. Pacini, F. Mastri, R. Trevisan, A. Costanzo, D. Masotti, " Theoretical and Experimental Characterization of Moving Wireless Power Transfer Systems", accepted for publications at 2016 10th European Conference on Antennas and Propagation (EuCAP).
- D. Masotti, A. Costanzo, M. Del Prete, V. Rizzoli, "Time-Modulation of Linear Arrays for Real-Time Reconfigurable Wireless Power Transmission," IEEE Transactions on Microwave Theory and Techniques, vol.64, no.2, pp.331-342, Feb. 2016
- M. Del Prete, D. Masotti, A. Costanzo, M. Magno, L. Benini, " A Dual-Band Wake-Up Radio for Ultra-low Power Wireless Sensor Networks", IEEE Radio and Wireless Week 2016 (RWW), pp. 1-4, 24-27 Jan. 2016
- M. Chiani, " Distribution of the largest root of a matrix for Roy's test in multivariate analysis of variance," Journal of Multivariate Analysis, vol. 143, pp. 467–471, 2016.
- B. Sobhani, T. Zwick, and M. Chiani, " Target TOA association with the Hough Transform in UWB Radars," IEEE Trans. Aerospace and Electronic Systems, Apr 2016.
- F. Guidi, N. Decarli, D. Dardari, F. Natali, E. Savioli, M. Bottazzi, " A low complexity scheme for passive UWB-RFID: Proof of concept," IEEE Communications Letters, 2016, accepted.
- M. Chiani, A. Elzanaty, and A. Giorgetti, "Analysis of the restricted isometry property for Gaussian random matrices," in Proc. IEEE Global Commun. Conf. (GLOBECOM), San Diego, CA, Dec. 2015.
- A. Mariani, A. Giorgetti, and M. Chiani, "Wideband Spectrum Sensing by Model Order Selection," IEEE Trans. on Wireless Comm., vol. 14, no. 12, pp. 6710-6721, Dec. 2015
- E. Paolini, G. Liva, and M. Chiani, " Coded slotted ALOHA: A graph-based method for uncoordinated multiple access," IEEE Trans. Inform. Theory, vol. 61, no. 12, pp. 6815–6832, Dec 2015.
- M. Del Prete, A. Costanzo, A. Georgiadis, A. Collado, D. Masotti, Z. Popovic, "A 2.45-GHz Energy-Autonomous Wireless Power Relay Node," IEEE Transactions on Microwave Theory and Techniques, vol.63, no.12, pp.4511-4520, Dec. 2015
- A. Costanzo, M. Dionigi, F. Mastri, M. Mongiardo, G. Monti, R. Perfetti, " Design of Matched

- Wireless Power Transfer Links Realized with Coupled Inductors”, 2015 IEEE 15th Mediterranean Microwave Symposium (MMS), pp.1-4, Nov. 30 2015-Dec. 2 2015.
- C. Constantinides, W. Tang, S.K. Podilchak, G. Goussetis, A. Costanzo, P. Nicole, " Design Considerations for Frequency Scanning Transmit Antennas in Wireless Power Transmission”, 2015 IEEE 15th Mediterranean Microwave Symposium (MMS), pp.1-4, Nov. 30 2015-Dec. 2 2015.
 - A. Guerra, F. Guidi, A. Clemente, R. D’Errico, L. Dussopt, and D. Dardari, " Millimeter-wave backscattering measurements with transmit arrays for personal radar applications,” in 2015 IEEE Global Communications Conference (GLOBECOM), San Diego, CA, Dec. 2015, pp. 1–6.
 - A. Guerra, F. Guidi, A. Clemente, R. D’Errico, L. Dussopt, and D. Dardari, " Application of Transmitarray Antennas for Indoor Mapping at Millimeter-Waves,” in IEEE European Conference on Networks and Communications, EUCNC 2015, Paris, France.
 - N. Decarli, F. Guidi, D. Dardari, " Passive UWB RFID for tag localization: Architectures and design,” IEEE Sensors Journal, 2015, early-access online.
 - G. Pasolini, E. Paolini, D. Dardari, and M. Chiani, " Experimental results on secret-key extraction from unsynchronized UWB channel observations,” in Physical and Data-Link Security Techniques for Future Communication Systems, ser. Lecture Notes in Electrical Engineering, M. Baldi and S. Tomasin, Eds. Springer International Publishing, 2016, vol. 358, pp. 111–124.
 - N. Decarli, et. Al, " The GRETA Architecture for Energy Efficient Radio Identification and Localization,” in Proc. EURASIP Workshop on RFID Technology (EURFID), Oberaudorf, Germany, October 2015, pp. 1–8.
 - S. Bartoletti, N. Decarli, A. Guerra, F. Guidi, D. Dardari, and A. Conti, " Energy-based Order of Arrival Estimation via UWB-UHF RFID,” in Proc. EURASIP Workshop on RFID Technology (EURFID), Oberaudorf, Germany, October 2015, pp. 1–6.
 - M. Fantuzzi, D. Masotti, A. Costanzo " Electromagnetic prediction of antenna layout impact on UWB localization and sensing”, Special session on GRETA project in 2015 International EURASIP Workshop on RFID Technology (EURFID), pp.16-21, 22-23 Oct. 2015
 - M. Del Prete, D. Masotti, A. Costanzo, M. Magno, L. Benini, "A 2.4 GHz-868 MHz dual-band wake-up radio for wireless sensor network and IoT,” 2015 IEEE 11th International Conference on Wireless and Mobile Computing, Networking and Communications (WiMob), pp.322-328, 19-21 Oct. 2015
 - A. Mariani, K. Sithamparanathan, and A. Giorgetti, "Periodic Spectrum Sensing with Non-Continuous Primary User Transmissions,” IEEE Trans. on Wireless Comm., vol. 14, no. 3, pp. 1636 - 1649, March 2015.
 - D. Dardari, " Detection and accurate localization of harmonic chipless tags,” EURASIP Journal on Advances in Signal Processing, vol. 2015, no. 77, pp. 1–13, 2015.
 - F. Guidi, A. Guerra, and D. Dardari, " Personal mobile radars with millimeter-wave massive arrays for indoor mapping,” IEEE Trans. on Mobile Computing, 2015.
 - M. del Prete, A. Costanzo, A. Georgiadis, A. Collado, D. Masotti, and Z. Popovic, " A 2.45 GHz Energy-autonomous Wireless Power Relay Node”, IEEE Transactions on Microwave Theory and Techniques, vol.63, no.12, pp.4511-4520, Dec. 2015
 - M. Fantuzzi, D. Masotti, A. Costanzo " Electromagnetic prediction of antenna layout impact on UWB localization and sensing”, EURASIP RFID Workshop 2015, Oct. 2015
 - M. Fantuzzi, D. Masotti, A. Costanzo, " A multilayer compact-size UWB-UHF antenna system for novel RFID applications”, 2015 European Microwave Conference (EuMC), pp.255-258, 7-10 Sept. 2015
 - A. Costanzo, M. Fantuzzi, D. Masotti, F. Mastri, V. Rizzoli, "A rigorous circuit-level description of IR-UWB links,” 2015 International Conference on Electromagnetics in Advanced Applications (ICEAA), pp.553-556, 7-11 Sept. 2015
 - M. Fantuzzi, D. Masotti, A. Costanzo, " A novel integrated UWB-UHF one-port antenna for localization and energy harvesting”, IEEE Transactions on Antennas and Propagation, vol. 63, no. 9, pp. 3839-3848, Sept. 2015

- A. Costanzo, D. Masotti, " Start-up Solutions for Ultra-low Power RF Harvesting Scenarios", accepted for publication at IEEE MTT-S International Conference on Numerical Electromagnetic and Multiphysics Modelling and Optimization (NEMO 2015), Ottawa, Aug. 2015
- D. Masotti, A. Costanzo, V. Rizzoli, " Smart wireless power transfer operated by time-modulated arrays via a two-step procedure", International Journal on Antennas and Propagation (invited paper), vol. 2015, pp. 1-11, July 2015
- R. Marchukov, D. Masotti, A. Costanzo, " Dynamic Wireless Power Transfer by Time-Modulated Arrays", 2015 IEEE International Symposium on Antennas and Propagation & USNC/URSI National Radio Science Meeting, , pp.808-809, 19-24 July 2015
- S. Bartoletti, A. Giorgetti, M. Z. Win, and A. Conti, " Blind Selection of Representative Observations for Sensor Radar Networks," IEEE Trans. Veh. Technol., vol. 64, no. 4, pp. 1388–1400, Apr. 2015.
- A. Camarda, A. Romani, E. Macrelli, and M. Tartagni, " A 32 mV/69 mV input voltage booster based on a piezoelectric transformer for energy harvesting applications," Sensors Actuators A Phys., May 2015.
- M. Dini, A. Romani, M. Filippi, and M. Tartagni, " A Nano-Current Power Management IC for Low Voltage Energy Harvesting," IEEE Trans. Power Electron., vol. 31, no. 6, pp. 1–1, 2015.
- M. del Prete, A. Costanzo, A. Georgiadis, A. Collado, D. Masotti, and Z. Popovic, " Energy-autonomous Bi-directional Wireless Power Transmission (WPT) and Energy Harvesting Circuit", 2015 IEEE MTT-S International Microwave Symposium (IMS), pp.1-4, 17-22 May 2015
- M. Fantuzzi, D. Masotti, A. Costanzo, " Simultaneous UHF Energy Harvesting and UWB-RFID Communication", 2015 IEEE MTT-S International Microwave Symposium (IMS), pp. 1-4, May 2015, (invited paper)
- A. Costanzo, D. Masotti, " Wirelessly powering: an enabling technology for zero-power sensors, IoT and D2D communication", Microwave Symposium (IMS), 2015 IEEE MTT-S International, pp.1-4, 17-22 May 2015, (invited paper)
- M. Del Prete, D. Masotti, F. Berra and A. Costanzo, " Exploitation of a dual-band cell phone antenna for Near-field WPT", Wireless Power Transfer Conference (WPTC), 2015 IEEE , pp.1-4, 13-15 May 2015
- D. Masotti, R. Marchukov, V. Rizzoli and A. Costanzo , " Far-field Power Transmission by Exploiting Time-modulation in Linear Arrays", Wireless Power Transfer Conference (WPTC), 2015 IEEE , pp.1-4, 13-15 May 2015
- F. Berra, A. Costanzo, M. Dionigi, D. Masotti, F. Mastri, M. Mongiardo, R. Sorrentino, " Antenna design for unified far-field communication and near-field recharging", 9th European Conference on Antennas and Propagation (EuCAP), 2015, pp.1-4, 13-17 April 2015
- A. Mariani, A. Giorgetti, and M. Chiani, " Model order selection based on information theoretic criteria: Design of the penalty," IEEE Trans. Signal Processing, vol. 63, no. 11, pp. 2779–2789, June 2015.
- B. Sobhani, E. Paolini, M. Mazzotti, A. Giorgetti, and M. Chiani, "Multiple target tracking with particle filtering in UWB radar sensor networks," in Proc. International Conference on Localization and GNSS (ICL-GNSS), pp. 1-6, Gothenburg, Sweden, June 2015.
- A. Sharma, A. Mariani, A. Giorgetti, D. Mitra, and M. Chiani, "Subspace-based spectrum guarding," in Proc. IEEE International Conference on Communication (ICC), Workshop on Advances in Software Defined and Context Aware Cognitive Networks (IEEE SCAN-2015) pp. 411-416, London, UK, June 2015.
- A. Mariani, A. Giorgetti, and M. Chiani, "Designing ITC selection algorithms for wireless sources enumeration," in Proc. IEEE International Conference on Communications (ICC), pp. 4883-4888, London, UK, June 2015.
- D. Dardari, P. Closas, and P. M. Djuric, " Indoor tracking: Theory, methods, and technologies," IEEE Trans. Veh. Technol., vol. 64, no. 4, pp. 1263–1278, April 2015. Special Section.
- A. Guerra, F. Guidi, and D. Dardari, " Position and orientation error bound for wideband mas-

- sive antenna arrays," in IEEE ICC 2015 - Workshop on Advances in Network Localization and Navigation (ICC'15 - Workshop ANLN) , London, United Kingdom, Jun. 2015.
- D. Dardari, A. Arpino, F. Guidi, and R. Naldi, " A combined GP-State space method for efficient crowd mapping," in IEEE ICC 2015 - Workshop on Advances in Network Localization and Navigation (ICC'15 - Workshop ANLN) , London, United Kingdom, Jun. 2015.
 - M. Govoni, F. Guidi, V. D. Esposti, E. M. Vitucci, G. Tartarini, and D. Dardari, " UWB multistatic radars for obstacle detection and imaging in railroad crossing areas," in 12th Annual Workshop on Positioning, Navigation and Communication (WPNC'15), Dresden, Germany, Mar. 2015, pp. 1–6.
 - M. Govoni, E. M. Vitucci, V. D. Esposti, F. Guidi, G. Tartarini, and D. Dardari, " Study of a UWB multi-static radar for railroad crossing surveillance," in 2015 IEEE International Symposium on Antennas and Propagation and North American Radio Science Meeting , Vancouver, British Columbia, Canada, Jul. 2015, pp. 1–2.
 - A. Al-Rimawi and D. Dardari, " Analytical modeling of D2D communications over cellular networks," in IEEE ICC 2015 - Wireless Communications Symposium (ICC'15 (02) WC), London, United Kingdom, Jun. 2015.
 - A. Costanzo, D. Masotti, " Energy-Harvesting Fabric Antenna", chapter in book " Handbook of Smart Textiles", Ed. Springer, pp. 1-22, March 2015
 - A. Guerra, F. Guidi and D. Dardari, " Millimeter-Wave Personal Radars for 3D environment Mapping", ASILOMAR 2014, Nov. 2014.
 - A. Costanzo, M. Dionigi, D. Masotti, M. Mongiardo, G. Monti, L. Tarricone, R. Sorrentino, "Electromagnetic Energy Harvesting and Wireless Power Transmission: A Unified Approach," Proceedings of the IEEE , vol.102, no.11, pp.1692,1711, Nov. 2014.
 - F. Guidi, N. Decarli, S. Bartoletti, A. Conti, and D. Dardari, " Detection of multiple tags based on impulsive backscattered signals," IEEE Trans. Commun., 2014, accepted.
 - N. Decarli, A. Giorgetti, D. Dardari, M. Chiani, and M. Z. Win, " Stop-and-go receivers for non-coherent impulse communications," IEEE Trans. Wireless Commun., vol.13 n.9, pp. 4821–4835, Sep. 2014.
 - M. Chiani, " Distribution of the largest eigenvalue for real Wishart and Gaussian random matrices and a simple approximation for the Tracy-Widom distribution," Journal of Multivariate Analysis, vol. 129, pp. 69 – 81, 2014.
 - S. Gubinelli, E. Paolini, A. Giorgetti, M. Mazzotti, A. Rizzo, E. Troiani, and M. Chiani, " An ultra-wideband radar approach to nondestructive testing," in Proc. IEEE Int. Conf. on Ultra-Wideband (ICUWB), Paris, France, Sept. 2014.
 - A. Mariani, A. Giorgetti, and M. Chiani, " Wideband spectrum sensing for cognitive radio: a model order selection approach," in Proc. IEEE Int. Conf. on Commun. (ICC), Sydney, Australia, June 2014, pp. 1391–1396.
 - S. Bartoletti, A. Conti, A. Giorgetti, and M. Z. Win, " Sensor radar networks for indoor tracking," IEEE Wireless Commun. Lett., vol. 3, no. 2, pp. 157–160, Apr. 2014.
 - F. Guidi, C. Roblin, A. Sibille, and D. Dardari, " Analysis of UWB tag backscattering and its impact on the detection coverage," IEEE Trans. Antennas Propag., vol. 62, n. 8, , pp. 4292–4303, Aug. 2014.
 - A. Guerra, F. Guidi, and D. Dardari, " Energy sprinklers for passive UWB RFID," in IEEE International Conference on Ultra-Wideband, ICUWB 2014, Paris, France, Sep 2014, pp. 1–5.
 - F. Guidi, A. Guerra, and D. Dardari, " Millimeter-wave massive arrays for indoor SLAM," in Proc. IEEE Int. Conf. Commun. Workshops, Sydney, NSW, Jun. 2014, pp. 114-120.
 - S. Bartoletti, N. Decarli, A. Guerra, F. Guidi, D. Dardari, and A. Conti, " Order of Arrival Estimation via UHF-UWB RFID", Proc. IEEE Int. Conf. Commun. Workshops, Sydney, NSW, Jun. 2014, pp. 133-137.
 - M. Dini, A. Romani, M. Filippi, V. Bottarel, G. Ricotti, and M. Tartagni, " A Nano-current Power Management IC for Multiple Heterogeneous Energy Harvesting Sources," IEEE Trans. Power Electron., vol. PP, no. 99, pp. 1–1, 2014.

- A. Camarda, A. Romani, and M. Tartagni, " Piezoelectric Transformers for Ultra-low Voltage Energy Harvesting Applications," *Procedia Eng.*, vol. 87, pp. 1521–1524, 2014.
- M. Dini, M. Filippi, A. Romani, M. Tartagni, V. Bottarel, and G. Ricotti, " A 40 nA/source energy harvesting power converter for multiple and heterogeneous sources," in *ESSCIRC 2014 - 40th European Solid State Circuits Conference (ESSCIRC)*, 2014, pp. 259–262.
- N. Decarli and D. Dardari, " Ziv-Zakai bound for time delay estimation of unknown deterministic signals," in *2014 IEEE Int. Conf. on Acoustics, Speech, and Signal Processing (ICASSP)*, Florence, Italy, May 2014, pp. 1–5.
- N. Decarli, F. Guidi, and D. Dardari, " A novel joint RFID and radar sensor network for passive localization: Design and performance bounds," *IEEE J. Sel. Topics Signal Process.*, vol. 8, no. 1, pp. 80–95, Feb. 2014, special Issue on Non-cooperative Localization Networks.
- B. Sobhani, E. Paolini, A. Giorgetti, M. Mazzotti, and M. Chiani, " Target tracking for UWB multistatic radar sensor networks," *IEEE J. Sel. Topics Signal Process.*, vol. 8, no. 1, pp. 125–136, Feb. 2014, special Issue on Non-cooperative Localization Networks.
- N. Decarli, A. Guerra, A. Conti, R. D'Errico, A. Sibille, and D. Dardari, " Non-regenerative relaying for network localization," *IEEE Trans. Wireless Commun.*, vol. 13, no. 1, pp. 174–185, Jan. 2014.
- V. Zambianchi, E. Paolini, and D. Dardari, " Information transmission via source of opportunity signals: Piggyback communications," in *IEEE International Conference on Communications (ICC)*, Budapest, Hungary, Jun. 2013.
- N. Decarli and D. Dardari, " RFID and radar localization: A position error bound analysis," in *IEEE International Conference on Communication (ICC)*, Budapest, Hungary, Jun. 2013.
- M. Del Prete, D. Masotti, M. Dini, M. Filippi, A. Costanzo, A. Romani and M. Tartagni, " A Fully-Autonomous Integrated RF Energy Harvesting System for Wearable Applications", *2013 EuMC European Microwave Week*, Oct 2013.
- A. Costanzo and D. Masotti, " Design of RF energy harvesting platforms for power management unit with start-up circuits", *PowerMEMS (13th International Conference on Micro and Nanotechnology for Power Generation and Energy Conversion Applications)*, London Dec. 2013.
- B. Sobhani, M. Mazzotti, E. Paolini, A. Giorgetti, and M. Chiani, "Effect of State Space Partitioning on Bayesian Tracking for UWB Radar Sensor Networks," *IEEE International Conference on Ultra-Wideband (ICUWB)*, Sydney, Australia, Sep. 2013.
- S. Bartoletti, A. Giorgetti, and Andrea Conti, "Sensor Radars with Subset Diversity," *Int. Conf. on Comm., Work. on Advances in Network Localization and Navigation (ANLN)*, Budapest, Hungary, Jun 2013.

In addition, the following dissemination activities are reported:

- GTTI/SIEM Ancona 24-26 June 2013 – Chiani
- RAI TG3 – June 2013
- ClassTV – Dardari
- Packology, Rimini 11-14 June 2013 – Costanzo
- IEEE Workshop on Advances in Network Localization and Navigation (ANLN) at ICC 2013, Budapest, June 9-13 (Dardari, Conti et al.)
- Seminar at Université Catholique Louvain, 3/7/2013 - Dardari
- A. Costanzo, D. Masotti " CAD Tools and Techniques for Co-Design of Multi-Source Energy Autonomous Systems", *Digest of IEEE EuMC 2013 Workshop W03: Energy harvesting, circuit and system advances for battery-less Radio Frequency Identification (RFID) systems*, Norimberga, October, 2013
- IEEE 2nd Workshop on Advances in Network Localization and Navigation (ANLN) at ICC 2014, Sidney, 2014 (Dardari, Conti et al.)
- Organization of the Workshop on Localization of energy autonomous devices (Costanzo/Dardari) at EUMW 2014, Rome, Oct. 2014

- Best student paper award A. Guerra, N. Decarli, F. Guidi, and D. Dardari, " Energy sprinklers for passive UWB RFID," in IEEE International Conference on Ultra-Wideband, ICUWB 2014, Paris, France, Sep 2014
- IEEE 3rd Workshop on Advances in Network Localization and Navigation (ANLN) at ICC 2015, London, 2015 (Dardari, Conti et al.)
- Davide Dardari, Andrea Conti, " Localization of passive tags using UWB backscatter modulation" at Workshop on Localization of energy autonomous devices (EuMW 2014)
- A. Costanzo, D. Masotti, " Object selection and detection by monopulse RADAR", Digest of IEEE EuMC 2014 Workshop WS6: Localization of energy autonomous devices, Roma, October, 2014
- Dissemination Event at Telecom Italia, Torino, 26/2/2015 " UWB Backscatter Identification and Localization for IoT Energy-Efficient Applications" – (Davide Dardari)
- D. Masotti, " Time-modulated arrays for smart WPT", oral presentation at 4th meeting of COST – WIPE (action IC1301), Graz, 30-31 March, 2015
- A. Costanzo, D. Masotti, M. Del Prete, R. Trevisan, " Potential space applications of two far-field and near-field WPT systems", invited at International Microwave Symposium (IMS) 2015 Workshop WFK: New technology application for Space, Phoenix, May, 2015
- A. Costanzo, D. Masotti, M. Fantuzzi, " RF-baseband nonlinear co-design of zero-power harvesting systems", invited at International Microwave Symposium (IMS) 2015 Workshop WFC: Nonlinear RFID systems, characterization and exploitation, Phoenix, May, 2015
- A. Costanzo , Imperial college, London (UK) 14 ottobre 2015 Invited lecture for PhD students
- A. Costanzo, "COMBINING UWB- AND UHF- RFID FOR LOCALIZATION AND SENSING", 2nd European School on RFID Harvesting and sensing, Technosite, Valence (France) 27 ottobre 2015.
- A. Costanzo, "UWB-UHF circuit and system solutions for simultaneous wireless powering, tracking and sensing at ultra-low power", at the European school of Antennas (ESOA): Wireless networks: from Energy harvesting to information processing, CTTC, Barcellona 10 novembre 2015.
- A. Costanzo, D. Masotti, M. Fantuzzi " Combining UWB- and UHF-RFID for localization and sensing", invited in Workshop " European Initiatives to Develop Wireless Power Supply for Sensor Node Evolution" in IEEE Radio and Wireless Week 2016 (RW), 24-27 Jan. 2016.
- R. Trevisan, A. Costanzo, " Circuit Level Design of Systems for Simultaneous Data and Power Transfer", invited at International Microwave Symposium (IMS) 2016 Workshop WFJ: Theory and Application of Wireless Power Transfer, San Francisco, June, 2016
- C. Florian, F. Mastri, R.P. Paganelli, D. Masotti, A. Costanzo " Power amplifier load variation in high efficiency near-field inductive resonant wireless power transfer links with variable distance between transmitter and receiver", invited at International Microwave Symposium (IMS) 2016 Workshop WFK: Power Amplifiers with Variable Load, San Francisco, May, 2016

6.2 University of Ferrara

The following papers have been published:

- F. Zabini and A. Conti, "Inhomogeneous Poisson Sampling of Finite-Energy Signals with Uncertainties in \mathbb{R}^d ," IEEE Trans. Signal Process., to appear, 2016
- K. Witrisal et al., "High-accuracy localization for assisted living," IEEE Signal Process. Mag., vol. 33, no. 2, pp. 59 – 70, Mar. 2016.
- S. Bartoletti, N. Decarli, A. Guerra, F. Guidi, D. Dardari, and A. Conti, "Energy-based Order of Arrival Estimation via UWB-UHF RFID," in Proc. EURASIP Workshop on RFID Technology (EURFID), Oberaudorf, Germany, October 2015, pp. 1–6.
- N. Decarli, et. Al, "The GRETA Architecture for Energy Efficient Radio Identification and Localization," in Proc. EURASIP Workshop on RFID Technology (EURFID), Oberaudorf, Germany, October 2015, pp. 1–8.
- S. Bartoletti, W. Dai, A. Conti, and M. Z. Win, "Wideband localization via range likelihood

based on reduced dataset," in Proc. IEEE Canadian Workshop on Information Theory (CWIT), St. John's, Canada, Jul. 2015, pp. 93–96, *Student Paper Award, 1st place*.

- S. Bartoletti, A. Giorgetti, M. Z. Win, and A. Conti, "Blind Selection of Representative Observations for Sensor Radar Networks," *IEEE Trans. Veh. Technol.*, vol. 64, no. 4, pp. 1388–1400, Apr. 2015.
- S. Bartoletti, W. Dai, A. Conti, and M. Z. Win, "A Mathematical Model for Wideband Ranging," *IEEE J. Sel. Topics Signal Process.*, vol. 9, no. 2, pp. 216–228, Mar. 2015, Special Issue on Situational Awareness from Networked Sensors and Social Media.
- F. Guidi, N. Decarli, S. Bartoletti, A. Conti, and D. Dardari, "Detection of multiple tags based on impulsive backscattered signals," *IEEE Trans. Commun.*, 2014, vol. 62, no 11, pp. 3918–3930, Nov. 2014.
- S. Bartoletti, A. Conti, and M. Z. Win, "Passive radar via LTE signals of opportunity," in Proc. IEEE Workshop on Advances in Network Localization and Navigation (ICC), Sydney, Australia, Jun. 2014, pp. 181–185.
- S. Bartoletti, N. Decarli, A. Guerra, F. Guidi, D. Dardari, and A. Conti, "Order of arrival estimation via UHF-UWB RFID," in Proc. IEEE Workshop on Advances in Network Localization and Navigation (ICC), Sydney, Australia, Jun. 2014, pp. 133–137.
- S. Bartoletti, A. Conti, A. Giorgetti, and M. Z. Win, "Sensor radar networks for indoor tracking," *IEEE Wireless Commun. Lett.*, vol. 3, no. 2, pp. 157–160, Apr. 2014.
- A. Conti, D. Dardari, M. Guerra, L. Mucchi, and M. Z. Win, "Experimental characterization of diversity navigation," *IEEE Syst. J.*, vol. 8, no. 1, pp. 115–124, Mar. 2014.
- N. Decarli, A. Guerra, A. Conti, R. D'Errico, A. S. Dardari, and D. Dardari, "Non-regenerative relaying for network localization," *IEEE Trans. Wireless Commun.*, vol. 13, no. 1, pp. 174–185, Jan. 2014.
- S. Bartoletti, A. Giorgetti, and A. Conti, "Sensor Radars with Subset Diversity," in Proc. IEEE International Conference on Communication (ICC), Budapest, Hungary, Jun. 2013.

In addition, the following dissemination activities are reported:

- Dardari, Conti et al., IEEE 3rd Workshop on Advances in Network Localization and Navigation (ANLN) at ICC 2015, London, May 2015
- A. Conti, M. Z. Win, IEEE Tutorial, "Network Localization and Navigation: from Theory to Practice," IEEE WCNC'15, New Orleans, March 2015.
- Dardari, Conti et al., IEEE 2nd Workshop on Advances in Network Localization and Navigation (ANLN) at IEEE ICC 2014, Sidney, June 2014.
- A. Conti, IEEE Distinguished Lecture, "Network Localization of Tagged and Untagged Objects," at Nanyang Technology University and Institute for Infocomm Research, A*STAR, Singapore, February 2014.
- A. Conti, Keynote Speech, "Network Localization," at IEEE GIIS'13, Trento, Italy, October 2013.
- A. Conti, Keynote Speech, " Network Localization," at IEEE ISPCC'13, JUIT, India, September 2013.
- A. Conti, Invited talk at the 2013 IEEE Communications Theory Workshop, "Network Localization in the Presence of Backscattering Interference," Phuket, Thailand, June 2013.
- A. Conti, Invited talk at Chulalongkorn University, " Network Localization of Tagged and Untagged Objects," Bangkok, Thailand, June 2013.

6.3 University of L'Aquila

The following papers have been published or accepted for publication:

- R. Alesii, P. Di Marco, F. Santucci, P. Savazzi, R. Valentini, A. Vizziello : "Backscattering UWB/UHF hybrid solutions for Multi-Reader Multi-Tag passive RFID Systems", submitted, 2016.

- R. Valentini, M. Levorato, F. Santucci: " Aging Aware Random Channel Access for Battery-Powered Wireless Networks" in IEEE Wireless Communication Letters, 2016.
- Roberto Alesii, Piergiuseppe Di Marco, Fortunato Santucci, Pietro Savazzi, Roberto Valentini, and Anna Vizziello: Multi-reader multi-tag architecture for UWB-UHF radio frequency identification systems. International EURASIP Workshop on RFID Technology (EURFID). Rosenheim, Germany, October 2015.
- Nicolo Decarli, Anna Guerra, Francesco Guidi, Marco Chiani, Davide Dardari, Alessandra Costanzo, Marco Fantuzzi, Diego Masotti, Stefania Bartoletti, Jinous Shafiei Dehkordi, Andrea Conti, Aldo Romani, Marco Tartagni, Roberto Alesii, Piergiuseppe Di Marco, Fortunato Santucci, Luca Roselli, Marco Virili, Pietro Savazzi, and Maurizio Bozzi: The GRETA Architecture for Energy Efficient Radio Identification and Localization. International EURASIP Workshop on RFID Technology (EURFID). Rosenheim, Germany, October 2015.
- N. Rendevski and D. Cassioli, "Potentials of Low-Complexity Rake Receivers for 60 GHz UWB Wireless Communication Systems,? RTSI Forum, Turin, 16-18 Sep. 2015.
- D. Cassioli and N. Rendevski, ?Modulation and Detection Strategies for 60 GHz UWB High-Data Rate Wireless Indoor Communications,? TELSIKS 2015, Serbia, Nis, 14-17 Oct. 2015 (Invited Paper)
- D.Cassioli, "Statistical Analysis of Cars Induced Scattering in 60 GHz UWB Outdoor Channels,? IEEE VTC-Fall 2015, Boston, MA, USA, 6-9 Sep. 2015
- A. Falcone, L. Pomante, C. Rinaldi, and M. Santic, Performance analysis of a lightweight localization algorithm for WSNs in a real scenario, Signals, Circuits and Systems (ISSCS), 2015 International Symposium on, July 2015.
- N. Rendevski and D. Cassioli, 60 GHz UWB Rake Receivers in a Realistic Scenario for Wireless Home Entertainment, ICC 2015 - Wireless Communications Symposium (ICC?15 (02) WC), London, United Kingdom, Jun. 2015
- P. Di Marco, C. Fischione, F. Santucci, and K.H. Johansson, Modeling IEEE 802.15.4 networks over fading channels. IEEE Transactions on Wireless Communications, October 2014.
- C. Rinaldi, N. Rendevski, D.Cassioli, "Performance Evaluation of UWB Signaling at mmWaves," IEEE ICUWB International Conference on Ultra-Wideband, 1-3 Sept. 2014, Paris, France
- N. Rendevski and D. Cassioli, BER of IEEE 802.11ad OFDM Radios vs. Carrier Frequency in Real 60 GHz Indoor Channels, ICC 2014, Sydney, Australia, June 2014.
- D. Cassioli and N. Rendevski, A Statistical Model for the Shadowing Induced by Human Bodies in the Proximity of a mmWaves Radio Link, ICC 2014 WS on 5G, Sydney, Australia, June 2014.
- M. Vari and D. Cassioli, mmWaves RSSI Indoor Network Localization, ICC 2014 WS on ANLN, Sydney, Australia, June 2014.
- P. Di Marco, F. Santucci, and C. Fischione, Modeling anti-collision protocols for RFID systems with multiple access interference, IEEE ICC 2014, Sydney, Australia. June 2014.
- R. Alesii, R. Congiu, F. Santucci, P. Di Marco, and C. Fischione, Architectures and protocols for fast identification in large-scale RFID systems, IEEE ISCCSP 2014, Athens, Greece. May 2014.
- P. Di Marco, C. Fischione, F. Santucci, and K.H. Johansson, Effects of Rayleigh-lognormal fading on IEEE 802.15.4 networks. IEEE ICC 2013, Budapest, Hungary. June 2013.
- M. Di Renzo, C. Merola, A. Guidotti, F. Santucci, and G.E. Corazza, Error Performance of Multi-Antenna Receivers in a Poisson Field of Interferers: A Stochastic Geometry Approach, IEEE Transactions on Communications, Vol.:61 Issue:5 Pag.:2025 -2047, May 2013.
- A. Guidotti, V. Buccigrossi, M. Di Renzo, G.E. Corazza, and F. Santucci, Outage and symbol error probabilities of dual-hop AF relaying in a Poisson field of interferers, IEEE WCNC 2013, April 2013.

In addition, the following dissemination activities are reported:

- D. Cassioli, Millimeter-waves wireless communications, XI International Conference ETAI 2013, Ohrid, Macedonia. 26-28 Sept. 2013. Plenary Talk.

- Promoter and co-organizer of the GRETA Special Session at the 5th International EURASIP Workshop on RFID Technology, 22-23 October 2015, Rosenheim, Germany;
- The GRETA project has been mentioned and briefly illustrated within the presentations that Fortunato Santucci has made at Mid-Sweden University in Sundsvall, Sweden (August 20th, 2015) and at ENSEA in Paris (October 14, 2015).
- Roberto Valentini, invited speech at the Donald Bren School of Information and Computer Science, University of California, Irvine. " Presentation of the Doctoral research activity". March 20, 2015.
- M.Faraone, R.Alesii, S.Tennina, F.Graziosi, " Device Free Patients Localization in Controlled Indoor Environments", IEEE CAMAD2014, December 1-3, 2014, Athens, Greece

6.4 University of Pavia

The following papers have been published/accepted for publication and submitted:

- P. Gamba, E. Goldoni, P. Savazzi, P.G. Arpesi, C. Sopranzi, J. Durfour, "Wireless Passive Sensors for Remote Sensing of Temperature on Aerospace Platforms", WiSEE 2013.
- S. Moscato, R. Moro, M. Bozzi, L. Perregini, S. Sakouhi, F. Dhawadi, A. Gharsallah, P. Savazzi, A. Vizziello, P. Gamba : "Chipless RFID for Space Applications", in Proceeding of IEEE International Conference on Wireless for Space and Extreme Environments, Noordwijk, The Netherlands, 30-31 October 2014.
- P.G. Arpesi, C. Sopranzi, P. Gamba, E. Goldoni, P. Savazzi, J-F. Dufour, M. Lavagna, "Communication aspects in wireless passive sensing on spacecrafs," IEEE International Conference on Wireless for Space and Extreme Environments, WiSEE 2014.
- P. Gamba, E. Goldoni, P. Savazzi, P.G. Arpesi, C. Sopranzi, J-F. Dufour, M. Lavagna. Wireless Passive Sensors for Remote Sensing of Temperature on Aerospace Platforms. IEEE SENSORS JOURNAL, VOL. 14, NO. 11, NOVEMBER 2014.
- S. Kianoush, A. Vizziello, and P. Gamba : "Energy-efficient and Mobile-aided Cooperative Localization in Cognitive Radio Networks", IEEE Transactions on Vehicular Technology, vol. PP, no. 99, June 2015.
- R. Alesii, P. Di Marco, F. Santucci, P. Savazzi, R. Valentini, A. Vizziello : "Multi-reader multi-tag architecture for UWB/UHF radio frequency identification systems", in Proceeding of EURASIP RFID 2015 Workshop, Rosenheim, Germany, 22-23 Oct. 2015.
- P. Savazzi, A. Vizziello : "Carrier Synchronization in Distributed MIMO Satellite Links", in Proceeding of IEEE International Conference on wireless for space and extreme environments, IEEE WiSEE 2015, Orlando, FL, USA, 14-16 Dec. 2015.
- N. Decarli, et. Al, "The GRETA Architecture for Energy Efficient Radio Identification and Localization," Proc. EURASIP Workshop on RFID Technology (EURFID), Oberaudorf, Germany, October 2015, pp. 1-8.
- A. Vizziello, P. Savazzi : "Efficient RFID Tag Identification exploiting hybrid UHF-UWB tags and Compressive Sensing", submitted, 2015.
- R. Alesii, P. Di Marco, F. Santucci, P. Savazzi, R. Valentini, A. Vizziello : "Backscattering UWB/UHF hybrid solutions for Multi-Reader Multi-Tag passive RFID Systems", submitted, 2016.

6.5 University of Perugia

The following papers have been published/accepted for publication:

- M. Virili, A. Georgiadis, F. Mira, A. Collado, F. Alimenti, P. Mezzanotte, L. Roselli, "EH Performance of an Hybrid Energy Harvester for Autonomous Nodes", Wireless Sensors and Sensor Networks (WiSNet), 2016 IEEE Topical Conference on., 24 - 27 January 2016.
- Alimenti, F.; Mariotti, C.; Palazzi, V.; Virili, M.; Orecchini, G.; Mezzanotte, P. & Roselli, L. "Communication and Sensing Circuits on Cellulose," Journal of Low Power Electronics and Applications, 2015, 5, 151.

- M. Virili, A. Georgiadis, A. Collado, K. Niotaki, P. Mezzanotte, L. Roselli, F. Alimenti and N. B. Carvalho (2015). "Performance improvement of rectifiers for WPT exploiting thermal energy harvesting." *Wireless Power Transfer*, 2015, pp 22-31.
- Palazzi, V.; Mariotti, C.; Alimenti, F.; Virili, M.; Orecchini, G.; Mezzanotte, P. & Roselli, L. "Demonstration of a chipless harmonic tag working as crack sensor for electronic sealing applications" *Wireless Power Transfer*, 2015, 2, 78-85.
- Palazzari, V.; Mezzanotte, P.; Alimenti, F.; Fratini, F.; Orecchini, G.; Virili, M.; Mariotti, C.; Roselli, L., "Leaf compatible "eco-friendly" temperature sensor clip for high density monitoring wireless networks," in *Microwave Symposium (MMS), 2015 IEEE 15th Mediterranean* , vol., no., pp.1-4, Nov. 30 2015-Dec. 2 2015
- Virili, M.; Roselli, L.; Alimenti, F.; Mezzanotte, P.; Moscato, S.; Silvestri, L.; Bozzi, M.; Perugini, L., "GRETA approach towards new green material technologies," in *RFID Technology (EURFID), 2015 International EURASIP Workshop on* , vol., no., pp.9-15, 22-23 Oct. 2015. N. Decarli, et. Al, "The GRETA Architecture for Energy Efficient Radio Identification and Localization," in Proc. EURASIP Workshop on RFID Technology (EURFID), Oberaudorf, Germany, October 2015, pp. 1-8.
- Decarli, N.; Guerra, A.; Guidi, F.; Chiani, M.; Dardari, D.; Costanzo, A.; Fantuzzi, M.; Masotti, D.; Bartoletti, S.; Dehkordi, J.S.; Conti, A.; Romani, A.; Tartagni, M.; Alesii, R.; Di Marco, P.; Santucci, F.; Roselli, L.; Virili, M.; Savazzik, P.; Bozzik, M., "The GRETA architecture for energy efficient radio identification and localization," in *RFID Technology (EURFID), 2015 International EURASIP Workshop on* , vol., no., pp.1-8, 22-23 Oct. 2015
- F. Alimenti, V. Palazzi, C. Mariotti, M. Virili, G. Orecchini, L. Roselli, P. Mezzanotte, "24-GHz CW radar front-ends on cellulose-based substrates: A new technology for low-cost applications," *Microwave Symposium (IMS), 2015 IEEE MTT-S International* , vol., no., pp.1,4, 17-22 May 2015.
- V. Palazzi, F. Alimenti, C. Mariotti, M. Virili, G. Orecchini, L. Roselli, P. Mezzanotte, "Demonstration of a high dynamic range chipless RFID sensor in paper substrate based on the harmonic radar concept," *Microwave Symposium (IMS), 2015 IEEE MTT-S International* , vol., no., pp.1,4, 17-22 May 2015.
- C. Mariotti, R. Goncalves, Ricardo; M. Virili; N.B. Carvalho, L. Roselli, P. Pinho, "Dual-frequency antennas embedded into the floor for efficient RF "energy evaporation"," *Electronic Components and Technology Conference (ECTC) , 2015 IEEE 65th* , vol., no., pp.2066,2070, 26-29 May 2015.
- Virili, M.; Georgiadis, A.; Collado, A.; Mezzanotte, P.; Roselli, L., "EM characterization of a patch antenna with thermo-electric generator and Solar Cell for hybrid Energy Harvesting," in *Radio and Wireless Symposium (RWS), 2015 IEEE* , vol., no., pp.44-46, 25-28 Jan. 2015.
- Roselli, L.; Mariotti, C.; Mezzanotte, P.; Alimenti, F.; Orecchini, G.; Virili, M.; Carvalho, N.B., "Review of the present technologies concurrently contributing to the implementation of the Internet of Things (IoT) paradigm: RFID, Green Electronics, WPT and Energy Harvesting," in *Wireless Sensors and Sensor Networks (WiSNet), 2015 IEEE Topical Conference on* , vol., no., pp.1-3, 25-28 Jan. 2015.
- Poggiani, Martina; Alimenti, Federico; Mezzanotte, Paolo; Virili, Marco; Mariotti, Chiara; Orecchini, Giulia; Roselli, Luca: "24-GHz Patch antenna array on cellulose-based materials for green wireless internet applications", *IET Science, Measurement & Technology*, 2014.
- V. Palazzi, F. Alimenti, P. Mezzanotte, M. Virili, C. Mariotti, G. Orecchini, L. Roselli, "Low-Power Frequency Doubler in Cellulose-Based Materials for Harmonic RFID Applications," *Microwave and Wireless Components Letters, IEEE* , vol.24, no.12, pp.896,898, Dec. 2014.
- L. Roselli, N. B. Carvalho, F. Alimenti, P. Mezzanotte, G. Orecchini, M. Virili, C. Mariotti, R. Goncalves, and P. Pinho, "Smart surfaces: Large Area Electronics (LAE) systems for IoT enabled by energy harvesting," *Proceedings of the IEEE* , vol.102, no.11, pp.1723,1746, Nov. 2014.
- Virili, M.; Georgiadis, A.; Niotaki, K.; Collado, A.; Alimenti, F.; Mezzanotte, P.; Roselli, L.; Borges Carvalho, N., "Design and optimization of an antenna with Thermo-Electric Generator

- (TEG) for autonomous wireless nodes," in RFID Technology and Applications Conference (RFID-TA), 2014 IEEE , pp.21-25, 8-9 Sept. 2014.
- Virili, Marco; Casula, Giulia; Mariotti, Chiara; Orecchini, Giulia; Alimenti, Federico; Cosseddu, Piero; Mezzanotte, Paolo; Bonfiglio, Annalisa; Roselli, Luca, "7.5â€¢15 MHz organic frequency doubler made with pentacene-based diode and paper substrate," Microwave Symposium (IMS), 2014 IEEE MTT-S International, pp.1,4, 1–6 June 2014.
 - F. Alimenti, L. Roselli, "Theory of Zero-Power RFID Sensors Based on Harmonic Generation and Orthogonally Polarized Antennas," Progress in Electromagnetic Research, vol. 134, 2013, pp. 337-357.
 - Alimenti, F.; Mezzanotte, P.; Giacomucci, S.; Dionigi, M.; Mariotti, C.; Virili, M.; Roselli, L., "24 GHz Single-Balanced Diode Mixer Exploiting Cellulose-Based Materials," in Microwave and Wireless Components Letters, IEEE , vol.23, no.11, pp.596-598, Nov. 2013
 - L. Valentini, J. M. Kenny, F. Alimenti, L. Roselli, "Planar MOSFET Devices on Paper Substrate Using Graphene Oxide Film as Gate Dielectric", in Proc. of European Microwave Conference 2013, 6-11 Oct. 2013, Nuremberg, GE
 - C. Mariotti, F. Alimenti, P. Mezzanotte, M. Virili, S. Giacomucci, L. Roselli, "Modeling and characterization of copper adhesive tape microstrips on paper substrates", in Proc. of European Microwave Conference 2013, 6-11 Oct. 2013, Nuremberg, GE
 - S. Kim, C. Mariotti, F. Alimenti, P. Mezzanotte, A. Georgiadis, A. Collado, L. Roselli, M.M. Tentzeris, "No Battery Required: Perpetual RFID-Enabled Wireless Sensors for Cognitive Intelligence Applications," IEEE Microwave Magazine, vol. 14, n. 5, July-August 2013, pp. 66-77.
 - M. Virili, F. Alimenti, L. Roselli, P. Mezzanotte, M. Dionigi (2013). "Organic frequency doubler RFID tag exploiting 7.5-MHz wireless power transfer 2013 IEEE Wireless Power Transfer (WPT)." Proceedings of 2013 IEEE Wireless Power Transfer (WPT) 33- 36, In:2013 IEEE Wireless Power Transfer (WPT). 15-16 May 2013, Perugia.
 - L. Valentini, M. Cardinali, M. Mladjenovic, P. Uskokovic, F. Alimenti, L. Roselli, J. Kenny, "Flexible Transistors Exploiting P3HT on Paper Substrates and Graphene Oxide Films as Gate Dielectrics: Proof of Concept," Science of Advanced Materials, vol. 5, n. 5, May 2013, pp. 1-4.
 - F. Alimenti, C. Mariotti, P. Mezzanotte, M. Dionigi, M. Virili, L. Roselli, "A 1.2 V, 0.9 mW UHF VCO Based on Hairpin Resonator in Paper Substrate and Cu Adhesive Tape," IEEE Microwave and Wireless Component Letters, vol. 23, n. 4, April 2013, pp. 214-216.
 - L. Aluigi, T.T. Thai, M.M. Tentzeris, L. Roselli, F. Alimenti (2013). "Chip-to-package wireless power transfer and its application to mm-Wave antennas and monolithic radiometric receivers 2013 IEEE Radio and Wireless Symposium." Proceedings of 2013 IEEE Radio and Wireless Symposium 202- 204, In:2013 IEEE Radio and Wireless Symposium. 20-23 January 2013, Austin, TX.

REFERENCES

- [1] Davide Dardari, Raffaele D'Errico, Christophe Roblin, Alain Sibille, and Moe Z. Win. Ultrawide bandwidth RFID: The next generation? *Proceedings of the IEEE, Special Issue on RFID - A Unique Radio Innovation for the 21st Century.*, 98(9):1570 –1582, Sep 2010.
- [2] Francesco Guidi, Nicolif; Decarli, Stefania Bartoletti, Andrea Conti, and Davide Dardari. Detection of multiple tags based on impulsive backscattered signals. *IEEE Trans. Commun.*, 2014. In publication.
- [3] *Green tags (GRETA) project - Deliverable D2 (Report on the First Year of Activity)*, 2014.
- [4] Anna Guerra, Nicolo Decarli, Francesco Guidi, and Davide Dardari. Energy sprinklers for passive UWB RFID. In *Proc. IEEE Int. Conf. on Ultra-Wideband (ICUWB)*, pages 1–6, Paris, France, Sep. 2014.
- [5] *Green tags (GRETA) project - Deliverable D3 (Report on the Second Year of Activity)*, 2015.
- [6] R. D'Errico, M. Bottazzi, F. Natali, E. Savioli, S. Bartoletti, A. Conti, D. Dardari, N. Decarli, F. Guidi, F. Dehmas, L. Ouvry, U. Alvarado, N. Hadaschik, C. Frankek, Z. Mhanna, M. Sacko, Y. Wei, and A. Sibille. An UWB-UHF semi-passive RFID system for localization and tracking applications. In *Proc. IEEE Int. Conf. on RFID-Technology and Applications (RFID-TA)*, pages 1–6, Nice, France, Nov. 2012.
- [7] Piergiuseppe Di Marco, Roberto Alesii, Fortunato Santucci, and Carlo Fischione. An UWB-enhanced identification procedure for large-scale passive RFID systems. In *Proc. IEEE Int. Conf. on Ultra-Wideband (ICUWB)*, pages 421–426, Paris, France, September 2014.
- [8] N. Amin, Ng Wen Jye, and M. Othman. A bpsk backscatter modulator design for rfid passive tags. In *Radio-Frequency Integration Technology, 2007. RFIT 007. IEEE International Workshop on*, pages 262–265, Dec 2007.
- [9] Davide Dardari, Francesco Guidi, Christophe Roblin, and Alain Sibille. Ultra-wide bandwidth backscatter modulation: processing schemes and performance. *EURASIP Journal on Wireless Communications and Networking*, 2011(1):1–15, 2011.
- [10] D. Dardari and R. D'Errico. Passive ultrawide bandwidth rfid. In *Global Telecommunications Conference, 2008. IEEE GLOBECOM 2008. IEEE*, pages 1–6, Nov 2008.
- [11] F. Fuschini, C. Piersanti, F. Paolazzi, and G. Falciaiasecca. Analytical approach to the backscattering from uhf rfid transponder. *Antennas and Wireless Propagation Letters, IEEE*, 7:33–35, 2008.
- [12] N. Decarli, F. Guidi, A. Conti, and D. Dardari. Interference and clock drift effects in uwb rfid systems using backscatter modulation. In *Ultra-Wideband (ICUWB), 2012 IEEE International Conference on*, pages 546–550, Sept 2012.
- [13] U. Karthaus and M. Fischer. Fully integrated passive uhf rfid transponder ic with 16.7- mu;w minimum rf input power. *Solid-State Circuits, IEEE Journal of*, 38(10):1602–1608, Oct 2003.
- [14] G. De Vita and G. Iannaccone. Ultra low power rf section of a passive microwave rfid transponder in 0.35 um bicmos. In *Circuits and Systems, 2005. ISCAS 2005. IEEE International Symposium on*, pages 5075–5078 Vol. 5, May 2005.
- [15] G. De Vita, F. Bellatalla, and G. Iannaccone. Ultra-low power {PSK} backscatter modulator for {UHF} and microwave {RFID} transponders. *Microelectronics Journal*, 37(7):627 – 629, 2006.

- [16] G. De Vita and G. Iannaccone. Design criteria for the rf section of uhf and microwave passive rfid transponders. *Microwave Theory and Techniques, IEEE Transactions on*, 53(9):2978–2990, Sept 2005.
- [17] A. Facen and A. Boni. A cmos analog frontend for a passive uhf rfid tag. In *Low Power Electronics and Design, 2006. ISLPED'06. Proceedings of the 2006 International Symposium on*, pages 280–285, Oct 2006.
- [18] Changming Ma, Xingjun Wu, Chun Zhang, and ZhiHua Wang. A low-power rf front-end of passive uhf rfid transponders. In *Circuits and Systems, 2008. APCCAS 2008. IEEE Asia Pacific Conference on*, pages 73–76, Nov 2008.
- [19] Meng-Lin Hsia, Yu-Sheng Tsai, and O.T.-C. Chen. An uhf passive rfid transponder using a low-power clock generator without passive components. In *Circuits and Systems, 2006. MWSCAS '06. 49th IEEE International Midwest Symposium on*, volume 2, pages 11–15, Aug 2006.
- [20] Hongqiang Zong, Jinpeng Shen, Shan Liu, Mei Jiang, Qingyuan Ban, Ling Tang, Fanyu Meng, and Xin'an Wang. An ultra low power ask demodulator for passive uhf rfid tag. In *ASIC (ASICON), 2011 IEEE 9th International Conference on*, pages 637–640, Oct 2011.
- [21] M. Dini, A. Romani, M. Filippi, V. Bottarel, G. Ricotti, and M. Tartagni. A nanocurrent power management ic for multiple heterogeneous energy harvesting sources. *Power Electronics, IEEE Transactions on*, 30(10):5665–5680, Oct 2015.
- [22] S.B. Baik. Cmos comparator with hysteresis, Apr. 3rd 2001. US Patent 6,211,712.
- [23] Y. Osaki, T. Hirose, N. Kuroki, and M. Numa. Nano-ampere cmos current reference with little temperature dependence using small offset voltage. In *Circuits and Systems (MWSCAS), 2010 53rd IEEE International Midwest Symposium on*, pages 668–671, Aug 2010.
- [24] Zejun Wu, Xiaoxing Feng, and Xin'an Wang. An uhf rfid transponder with novel clock generator and demodulator. In *Cross Strait Quad-Regional Radio Science and Wireless Technology Conference (CSQRWC), 2011*, volume 2, pages 1041–1045, July 2011.
- [25] Nhan Tran, Bomson Lee, and Jong-Wook Lee. Development of long-range uhf-band rfid tag chip using schottky diodes in standard cmos technology. In *Radio Frequency Integrated Circuits (RFIC) Symposium, 2007 IEEE*, pages 281–284, June 2007.
- [26] Xiaoxing Feng, Xin'an Wang, Xing Zhang, Binjie Ge, Jinpeng Shen, Shan Liu, Yongzhen Qi, and Jinsi Zhong. An uhf rfid transponder for iso 18000-6b. In *ASIC, 2009. ASICON '09. IEEE 8th International Conference on*, pages 983–986, Oct 2009.
- [27] Davide Dardari, Francesco Guidi, Christophe Roblin, and Alain Sibille. Ultra-wide bandwidth backscatter modulation: Processing schemes and performance. *EURASIP J. Wireless Commun. Networking*, pages 1–15, July 2011.
- [28] John Kimionis, Aggelos Bletsas, and John N Sahalos. Increased range bistatic scatter radio. *IEEE Trans. Commun.*, 62(3):1091–1104, March 2014.
- [29] IEEE standard for information technology - telecommunications and information exchange between systems - local and metropolitan area networks - specific requirement part 15.4: Wireless medium access control (MAC) and physical layer (PHY) specifications for low-rate wireless personal area networks (WPANs). *IEEE Std 802.15.4a-2007 (Amendment to IEEE Std 802.15.4-2006)*, pages 1–203, 2007.

- [30] Nicolo Decarli, Francesco Guidi, and Davide Dardari. A novel joint RFID and radar sensor network for passive localization: Design and performance bounds. *IEEE J. Sel. Topics Signal Process.*, 8(1):80–95, February 2014.
- [31] Sanming Hu, C.L. Law, and Wenbin Dou. Measurements of UWB antennas backscattering characteristics for RFID systems. In *Proc. IEEE Int. Conf. on Ultra-Wideband (ICUWB)*, pages 94–99, Singapore, September 2007.
- [32] Sanming Hu, C.L. Law, and Wenbin Dou. A balloon-shaped monopole antenna for passive UWB-RFID tag applications. *IEEE Antennas Wireless Propag. Lett.*, 7:366–368, 2008.
- [33] Francesco Guidi, Alain Sibille, Christophe Roblin, Valerio Casadei, and Davide Dardari. Analysis of UWB tag backscattering and its impact on the detection coverage. *IEEE Trans. Antennas Propag.*, 62(8):4292–4303, August 2014.
- [34] Davide Dardari, Raffaele D’Errico, Christophe Roblin, Alain Sibille, and Moe Z. Win. Ultrawide bandwidth RFID: The next generation? *Proc. IEEE*, 98(9):1570–1582, September 2010.
- [35] P. Meissner, E. Leitinger, and K. Witrisal. UWB for robust indoor tracking: Weighting of multipath components for efficient estimation. *IEEE Wireless Commun. Lett.*, 3(5):501–504, October 2014.
- [36] R. D’Errico, J. Keignart, and L. Rudant. Characterization of UWB backscattering propagation for passive tags identification and localization. In *European Conf. on Antennas and Propag. (EuCAP)*, pages 1909–1913, Gothenburg, Sweden, April 2013.
- [37] A Sibille, Z. Mhanna, M. Sacko, R. Contreras, V. Casadei, and R. D’Errico. Channel modeling for backscattering based UWB tags in a RTLS system with multiple readers. In *European Conf. on Antennas and Propag. (EuCAP)*, pages 3022–3026, Gothenburg, Sweden, April 2013.
- [38] J.D. Griffin and G.D. Durgin. Complete link budgets for backscatter-radio and RFID systems. *IEEE Antennas Propag. Mag.*, 51(2):11–25, April 2009.
- [39] F. Guidi, A. Sibille, and C. Roblin. Interaction of UWB tag backscattering with close metallic reflectors. *IEEE Antennas Wireless Propag. Lett.*, 13:245–248, 2014.
- [40] Francesco Guidi, Alain Sibille, Davide Dardari, and Christophe Roblin. UWB RFID backscattered energy in the presence of nearby metallic reflectors. In *Proc. of the European Conf. on Antennas and Propag. (EuCAP)*, pages 1425–1429, Rome, Italy, April 2011.
- [41] A. Lazaro, A. Ramos, R. Villarino, and D. Girbau. Active UWB reflector for RFID and wireless sensor networks. *IEEE Trans. Antennas Propag.*, 61(9):4767–4774, September 2013.
- [42] Nicolo Decarli, Francesco Guidi, Andrea Conti, and Davide Dardari. Interference and clock drift effects in UWB RFID systems using backscatter modulation. In *Proc. IEEE Int. Conf. on Ultra-Wideband (ICUWB)*, pages 1–5, Syracuse, NY, Sep. 2012.
- [43] Kin Keung Lee, K. Granhaug, and N. Andersen. A study of low-power crystal oscillator design. In *Proc. NORCHIP Conf.*, pages 1–4, Vilnius, Lithuania, November 2013.
- [44] P. Di Marco, F. Santucci, and C. Fischione. Modeling anti-collision protocols for RFID systems with multiple access interference. In *Proc. IEEE Int. Conf. on Commun.*, pages 5938–5944, Sydney, Australia, June 2014.
- [45] A. Ramos, A. Lazaro, and D. Girbau. Semi-passive time-domain UWB RFID system. *IEEE Trans. Microwave Theory Tech.*, 61(4):1700–1708, April 2013.

- [46] D. Lachartre, B. Denis, D. Morche, L. Ouvry, M. Pezzin, B. Piaget, J. Prouve, and P. Vincent. A 1.1nJ/b 802.15.4a-Compliant Fully Integrated UWB Transceiver in 0.13 μ m CMOS. In *Proc. of the ISSCC*, San Francisco, USA, Feb. 2009.
- [47] E. Savioli, M. Bottazzi, F. Natali, N. Decarli, F. Guidi, N. Hadaschik, R. D'Errico, and L. Ouvry. Semi-passive UHF-UWB RFID: Architecture and localization performance. In *Proc. IEEE Int. Conf. on Commun. Workshops*, pages 1–5, Budapest, Hungary, June 2013.
- [48] L. Mucchi, E. Del Re, and T. Landi. Multi-level environment identification method for impulsive radio systems. In *Proc. IEEE Int. Conf. on Ultra-Wideband (ICUWB)*, pages 385–389, Bologna, Italy, September 2011.
- [49] P. Closas, C. Fernández-Prades, and J. A. Fernandez-Rubio. A Bayesian approach to multipath mitigation in GNSS receivers. *IEEE J. Sel. Topics Signal Process.*, 3(4):695–706, August 2009.
- [50] P. Closas and C. Fernández-Prades. A statistical multipath detector for antenna array based GNSS receivers. *IEEE Trans. Wireless Commun.*, 10(3):916–929, March 2011.
- [51] P. Closas and M. F. Bugallo. Improving accuracy by iterated multiple particle filtering. *IEEE Signal Processing Lett.*, 19(8):531–534, August 2012.
- [52] Hsiao-Chun Wu, Yiyan Wu, J. C. Principe, and Xianbin Wang. Robust switching blind equalizer for wireless cognitive receivers. *IEEE Trans. Wireless Commun.*, 7(5):1461–1465, May 2008.
- [53] A. Athalye, V. Savic, M. Bolic, and P. M. Djuric. Novel semi-passive RFID system for indoor localization. *IEEE Sensors J.*, 13(2):528–537, February 2013.
- [54] E. Arias de Reyna and P. M. Djuric. Indoor localization with range-based measurements and little prior information. *IEEE Sensors J.*, 13(5):1979–1987, May 2013.
- [55] Stefania Bartoletti, Wenhan Dai, Andrea Conti, and Moe Z. Win. A mathematical model for wideband ranging. *IEEE J. Sel. Topics Signal Process.*, 9(2):216–228, March 2015.
- [56] Stefania Bartoletti, Andrea Giorgetti, Moe Z. Win, and Andrea Conti. Blind selection of representative observations for sensor radar networks. *IEEE Trans. Veh. Technol.*, 64(4):157–160, April 2015.
- [57] N. Balakrishnan and Chin Diew Lai. *Continuous Bivariate Distributions*. Springer, second edition, 2009.
- [58] Davide Dardari, Andrea Conti, Ulric J. Ferner, Andrea Giorgetti, and Moe Z. Win. Ranging with ultrawide bandwidth signals in multipath environments. *Proc. IEEE*, 97(2):404–426, February 2009. special issue on *Ultra-Wide Bandwidth (UWB) Technology & Emerging Applications*.
- [59] Merrill I. Skolnik. *Radar Handbook*. McGraw-Hill, New York, NY 10020, 3 edition, 1970.
- [60] Stefania Bartoletti, Wenhan Dai, Andrea Conti, and Moe Z. Win. Wideband localization via range likelihood based on reduced dataset. St. John's, NL, Canada, July 2015.
- [61] Stefania Bartoletti, Wenhan Dai, Andrea Conti, and Moe Z. Win. A mathematical model for wideband ranging. *IEEE J. Sel. Topics Signal Process.*, 9(2):216–228, March 2015.
- [62] Andrea Giorgetti and Marco Chiani. Time-of-arrival estimation based on information theoretic criteria. *IEEE Trans. Signal Processing*, 61(8):1869–1879, April 2013.
- [63] Ismail Guvenc and Zafer Sahinoglu. TOA estimation with different IR-UWB transceiver types. In *IEEE Int. Conf. on Ultra-Wideband*, pages 426–431, Zurich, Switzerland, Sep 2005.

- [64] Joon-Yong Lee and Robert A. Scholtz. Ranging in a dense multipath environment using an UWB radio link. *IEEE J. Select. Areas Commun.*, 20(9):1677–1683, December 2002.
- [65] Robert A. Scholtz and Joon-Yong Lee. Problems in modeling UWB channels. *Electronic letters*, 20(9):1–10, December 2002.
- [66] Davide Dardari, Chia-Chin Chong, and Moe Z. Win. Threshold-based time-of-arrival estimators in UWB dense multipath channels. *IEEE Trans. Commun.*, 56, 2008.
- [67] Federal Communications Commission. Revision of part 15 of the commission's rules regarding ultra-wideband transmission systems, first report and order (ET Docket 98-153), Adopted Feb. 14, 2002, Released Apr. 22, 2002.
- [68] Andreas F. Molisch, Dajana Cassioli, Chia-Chin Chong, Shahriar Emami, Andrew Fort, Balakrishnan Kannan, Johan Karedal, Juergen Kunisch, Hans Schantz, Kai Siwiak, and Moe Z. Win. A comprehensive standardized model for ultrawideband propagation channels. *IEEE Trans. Antennas Propagat.*, 54(11):3151–3166, November 2006. Special Issue on Wireless Communications.
- [69] D.V. Sarwate and M.B. Pursley. Crosscorrelation properties of pseudorandom and related sequences. *Proc. IEEE*, 68(5):593–619, May 1980.
- [70] Enrico Paolini, Andrea Giorgetti, Marco Chiani, Riccardo Minutolo, and Mauro Montanari. Localisation capability of cooperative anti-intruder Radar systems. 2008:1–14, June 2008.
- [71] M. Chiani, A. Giorgetti, M. Mazzotti, R. Minutolo, and E. Paolini. Target detection metrics and tracking for UWB radar sensor networks. In *Ultra-Wideband, 2009. ICUWB 2009. IEEE International Conference on*, pages 469–474, Sept. 2009.
- [72] B. Sobhani, M. Mazzotti, E. Paolini, A. Giorgetti, and M. Chiani. Effect of state space partitioning on Bayesian tracking for UWB radar sensor networks. In *2013 IEEE International Conference on Ultra-Wideband (ICUWB)*, pages 120–125, Sept 2013.
- [73] B. Sobhani, E. Paolini, A. Giorgetti, M. Mazzotti, and M. Chiani. Bayesian tracking in UWB radar sensor networks. In *2013 IEEE International Conference on Communications Workshops (ICC)*, pages 47–51, June 2013.
- [74] B. Sobhani, M. Mazzotti, E. Paolini, A. Giorgetti, and M. Chiani. Multiple target detection and localization in UWB multistatic radars. In *2014 IEEE International Conference on Ultra-WideBand (ICUWB)*, pages 135–140, Sept 2014.
- [75] B. Sobhani, E. Paolini, M. Mazzotti, A. Giorgetti, and M. Chiani. Multiple target tracking with particle filtering in UWB radar sensor networks. In *2015 International Conference on Location and GNSS (ICL-GNSS)*, pages 1–6, June 2015.
- [76] B. Sobhani, E. Paolini, A. Giorgetti, M. Mazzotti, and M. Chiani. Target tracking for UWB multistatic radar sensor networks. *Selected Topics in Signal Processing, IEEE Journal of*, 8(1):125–136, Feb 2014.
- [77] M. Malanowski and K. Kulpa. Two methods for target localization in multistatic passive radar. *IEEE Trans. Aerospace Electronic Syst.*, 48(1):572–580, January 2012.
- [78] D. Dardari, E. Falletti, and M. Luise. In *Satellite and Terrestrial Radio Positioning Techniques - A signal processing perspective*. Elsevier Ltd, London, 2011.
- [79] N. Decarli and D. Dardari. RFID and Radar localization: A position error bound analysis. In *Proc. IEEE Int. Conf. on Commun. Workshops*, pages 37–41, Budapest, Hungary, June 2013.

- [80] S. Bartoletti, N. Decarli, A. Guerra, F. Guidi, D. Dardari, and A. Conti. Order of arrival estimation via UHF-UWB RFID. In *Proc. IEEE Int. Conf. on Commun. Workshops*, pages 133–137, Sydney, Australia, June 2014.
- [81] A. Buffi, P. Nepa, and F. Lombardini. A phase-based technique for localization of UHF-RFID tags moving on a conveyor belt: Performance analysis and test-case measurements. *IEEE Sensors J.*, 15(1):387–396, January 2015.
- [82] L. Shangguan, Z. Li, Z. Yang, M. Li, Y. Liu, and J. Han. OTrack: Towards order tracking for tags in mobile RFID system. *IEEE Trans. Parallel Distrib. Syst.*, 25(8):2114–2125, August 2013.
- [83] D. Dardari and R. D’Errico. Passive ultrawide bandwidth RFID. In *IEEE Global Telecommunications Conference (GLOBECOM)*, 2008.
- [84] Yuan Zhou, C.L. Law, Yong Liang Guan, and F. Chin. Localization of passive target based on UWB backscattering range measurement. In *IEEE International Conference on Ultra-Wideband, ICUWB*, 2009.
- [85] *Green tags (GRETA) project - Deliverable D2 (Report on the First Year of Activity)*, 2014.
- [86] A. Vizziello and P. Savazzi. Efficient rfid tag identification exploiting hybrid uhf-uwb tags and compressive sensing. *submitted to IEEE Sensors Journal*, 2015.
- [87] Jue Wang, Haitham Hassanieh, Dina Katabi, and Piotr Indyk. Efficient and reliable low-power backscatter networks. In Lars Eggert, Jörg Ott, Venkata N. Padmanabhan, and George Varghese, editors, *SIGCOMM*, pages 61–72. ACM, 2012.
- [88] Guanhong Lai, Yu Liu, Xiaocheng Lin, and Lin Zhang. Collision-based radio frequency identification using compressive sensing. In *Communication Technology (ICCT), 2013 15th IEEE International Conference on*, pages 759–763, Nov 2013.
- [89] J. Waldrop, D.W. Engels, and Sanjay E. Sarma. Colorwave: an anticollision algorithm for the reader collision problem. In *Communications, 2003. ICC ’03. IEEE International Conference on*, volume 2, pages 1206–1210, May 2003.
- [90] ETSI. Etsi en 302 208-1, 2009.
- [91] S.M. Birari and S. Iyer. Mitigating the reader collision problem in rfid networks with mobile readers. In *Networks, 2005. Jointly held with the 2005 IEEE 7th Malaysia International Conference on Communication., 2005 13th IEEE International Conference on*, volume 1, pages 6 pp.–, Nov 2005.
- [92] J. Ho, D.W. Engels, and Sanjay E. Sarma. Hiq: a hierarchical q-learning algorithm to solve the reader collision problem. In *Applications and the Internet Workshops, 2006. SAINT Workshops 2006. International Symposium on*, pages 4 pp.–, Jan 2006.
- [93] Shaojie Tang, Cheng Wang, Xiang-Yang Li, and Changjun Jiang. Reader activation scheduling in multi-reader rfid systems: A study of general case. In *Parallel & Distributed Processing Symposium (IPDPS), 2011 IEEE International*, pages 1147–1155. IEEE, 2011.
- [94] Binbin Chen, Ziling Zhou, and Haifeng Yu. Understanding rfid counting protocols. In *Proceedings of the 19th Annual International Conference on Mobile Computing & Networking, MobiCom ’13*, pages 291–302, 2013.
- [95] P. Di Marco, R. Alesii, F. Santucci, and C. Fischione. An uwb-enhanced identification procedure for large-scale passive rfid systems. In *Ultra-WideBand (ICUWB), 2014 IEEE International Conference on*, pages 421–426, Sept 2014.

- [96] R. Alesii, R. Congiu, F. Santucci, P. Di Marco, and C. Fischione. Architectures and protocols for fast identification in large-scale rfid systems. In *Communications, Control and Signal Processing (ISCCSP), 2014 6th International Symposium on*, pages 243–247, May 2014.
- [97] Davide Dardari, Francesco Guidi, Christophe Roblin, and Alain Sibille. Ultra-wide bandwidth backscatter modulation: Processing schemes and performance. *EURASIP Journal on Wireless Communications and Networking*, 2011:47(1), 2011.
- [98] M. Fantuzzi, D. Masotti, and A. Costanzo. A multilayer compact-size uwb-uhf antenna system for novel rfid applications. In *Microwave Conference (EuMC), 2015 European*, pages 255–258, Sept 2015.
- [99] F. Guidi, N. Decarli, D. Dardari, C. Roblin, and A. Sibille. Performance of uwb backscatter modulation in multi-tag rfid scenario using experimental data. In *Ultra-Wideband (ICUWB), 2011 IEEE International Conference on*, pages 484–488, Sept 2011.
- [100] EPCGlobal. Class 1 generation 2 UHF air interface protocol standard v.1.0.9. 2005.
- [101] D.L. Donoho. Compressed sensing. *Information Theory, IEEE Transactions on*, 52(4):1289–1306, April 2006.
- [102] P. Savazzi and P. Gamba. Iterative symbol timing recovery for short burst transmission schemes. *Communications, IEEE Transactions on*, 56(10):1729–1736, 2008.
- [103] C.W. Farrow. A continuously variable digital delay element. In *Proc. IEEE International Symposium on Circuits and Systems (ISCAS '88*, pages 2641–2645, June 1988 1988.
- [104] V. Välimäki. A new filter implementation strategy for lagrange interpolation. In *Proc. IEEE International Symposium on Circuits and Systems (ISCAS '95*, pages 484–488, 30 Apr-3 May 1995 1995.
- [105] Ram Ramanathan. On the performance of ad hoc networks with beamforming antennas. In *Proceedings of the 2Nd ACM International Symposium on Mobile Ad Hoc Networking & Computing*, pages 95–105. ACM, 2001.
- [106] N. Decarli, F. Guidi, and D. Dardari. Passive uwb rfid for tag localization: Architectures and design. *Sensors Journal, IEEE*, (99):1–1, 2015.
- [107] R. Alesii, P. Di Marco, F. Santucci, P. Savazzi, R. Valentini, and A. Vizziello. Multi-reader multi-tag architecture for UWB/UHF radio frequency identification systems. In *2015 International EURASIP Workshop on RFID Technology (EURFID)*, pages 28–35, Oct 2015.
- [108] Stefano Tennina, Marco Di, Fabio Graziosi, and Fortunato Santucci. Distributed localization algorithms for wireless sensor networks: From design methodology to experimental validation. In *Wireless Sensor Networks*. InTech, jun 2011.
- [109] P.V. Nikitin and K.V.S. Rao. Performance limitations of passive uhf rfid systems. In *IEEE Antennas and Propagation Society International Symposium 2006*, pages 1011–1014, July 2006.
- [110] Vinod Namboodiri and Ravi Pendse. Bit level synchronized mac protocol for multireader rfid networks. *EURASIP Journal on Wireless Communications and Networking*, 2010(1):956578, 2010.